



2008

# ELECTRON FIELD-EMISSION FROM CARBON NANOTUBES FOR NANOMACHINING APPLICATIONS

Jaime A. Sanchez

*University of Kentucky*, [jasanc0@engr.uky.edu](mailto:jasanc0@engr.uky.edu)

**[Click here to let us know how access to this document benefits you.](#)**

---

## Recommended Citation

Sanchez, Jaime A., "ELECTRON FIELD-EMISSION FROM CARBON NANOTUBES FOR NANOMACHINING APPLICATIONS" (2008). *University of Kentucky Doctoral Dissertations*. 590.  
[https://uknowledge.uky.edu/gradschool\\_diss/590](https://uknowledge.uky.edu/gradschool_diss/590)

This Dissertation is brought to you for free and open access by the Graduate School at UKnowledge. It has been accepted for inclusion in University of Kentucky Doctoral Dissertations by an authorized administrator of UKnowledge. For more information, please contact [UKnowledge@lsv.uky.edu](mailto:UKnowledge@lsv.uky.edu).

ABSTRACT OF DISSERTATION

Jaime A. Sánchez

The Graduate School  
University of Kentucky

2008

ELECTRON FIELD-EMISSION FROM CARBON NANOTUBES  
FOR NANOMACHINING APPLICATIONS

---

ABSTRACT OF DISSERTATION

---

A dissertation submitted in partial fulfillment of the  
requirements for the degree of Doctor of Philosophy in the  
College of Engineering  
at the University of Kentucky

By  
Jaime A. Sánchez

Lexington, Kentucky

Director: Dr. M. Pınar Mengüç, Professor of the Department of Mechanical Engineering

Lexington, Kentucky

2008

Copyright © Jaime A. Sánchez 2008

## ABSTRACT OF DISSERTATION

### ELECTRON FIELD-EMISSION FROM CARBON NANOTUBES FOR NANOMACHINING APPLICATIONS

The ability to pattern in the nanoscale to drill holes, to draw lines, to make circles, or more complicated shapes that span a few atoms in width is the main driver behind current efforts in the rapidly growing area of nanomanufacturing. In applications ranging from the microprocessor industry to biomedical science, there is a constant need to develop new tools and processes that enable the shrinking of devices. For this and more applications, nanomanufacturing using electron beams offers a window of opportunity as a top-down approach since electrons, unlike light, have a wavelength that is in the order of the atomic distance. Though the technology based on electron beams has been available for more than twenty years, new concepts are constantly being explored and developed based on fundamental approaches. As such, a tool that utilizes electron field-emission from carbon nanotubes was proposed to accomplish such feats.

A full numerical analysis of electron field-emission from carbon nanotubes for nanomachining applications is presented. The different aspects that govern the process of electron field-emission from carbon nanotubes using the finite element method are analyzed. Extensive modeling is carried here to determine what the effect of different carbon nanotube geometries have on their emission profiles, what energy transport processes they are subject to, and establish what the potential experimental parameters are for nanomachining.

This dissertation builds on previous efforts based on Monte Carlo simulations to determine electron deposition profiles inside metals, but takes them to next level by considering realistic emission scenarios. A hybrid numerical approach is used that combines the two-temperature model with Molecular Dynamics to study phase change and material removal in depth. The use of this method, allows the determination of the relationship between the amount of energy required to remove a given number of atoms from a metallic workpiece and the number of carbon nanotubes and their required settings in order to achieve nanomachining.

Finally, the grounds for future work in this area are provided, including the need for novel electron focusing systems, as well as the extension of the hybrid numerical approach to study different materials.

**KEYWORDS:** electron field-emission, molecular dynamics,  
nanoscale phase change, material removal,  
nanomanufacturing

---

Jaime A. Sánchez

---

January 18, 2008

ELECTRON FIELD-EMISSION FROM CARBON NANOTUBES  
FOR NANOMACHINING APPLICATIONS

by

Jaime A. Sánchez

Dr. M. Pinar Mengüç

---

Director of Dissertation

Dr. L. S. Stephens

---

Director of Graduate Studies

January 18, 2008

---

## RULES FOR THE USE OF DISSERTATIONS

Unpublished dissertations submitted for the Doctor's degree and deposited in the University of Kentucky Library are as a rule open for inspection, but are to be used only with due regard to the rights of the authors. Bibliographical references may be noted, but quotations of summaries of parts may be published only with the permission of the author, and with the usual scholarly acknowledgments.

Extensive copying or publication of the dissertation in whole or in part also requires the consent of the Dean of the Graduate School of the University of Kentucky.

A library that borrows this thesis for use by its patrons is expected to secure the signature of each user.

Name

Date

---

---

---

---

---

---

---

---

---

---

DISSERTATION

Jaime A. Sánchez

The Graduate School  
University of Kentucky

2008



ELECTRON FIELD-EMISSION FROM CARBON NANOTUBES  
FOR NANOMACHINING APPLICATIONS

---

DISSERTATION

---

A dissertation submitted in partial fulfillment of the  
requirements for the degree of Doctor of Philosophy in the  
College of Engineering  
at the University of Kentucky

By  
Jaime A. Sánchez

Lexington, Kentucky

Director: Dr. M. Pınar Mengüç, Professor of the Department of Mechanical Engineering

Lexington, Kentucky

2008

Copyright © Jaime A. Sánchez 2008

I would like to dedicate this Dissertation to my father,  
Dr. Jaime Sánchez S. His strength is my inspiration

## ACKNOWLEDGEMENTS

Throughout all these years, from my undergraduate education until now, my family has been the source of constant support and comfort, especially my parents. My father, Jaime, always encouraged me from the very beginning, with valuable advice on patience and perseverance, even more so, when I chose not to become a medical doctor as himself, but rather pursue the engineering discipline. My role model, I try to live my life and follow my dreams always excelling in everything I do just as he does. My mother, Teresa, always listened and comforted me as I embarked in a long road that has taken a little over ten years until my studies were complete. Back then, this day seemed so far away, but they helped me stay focused on my goals. My brothers, Luis, Francisco and Diego, and my sister, Maria Isabel, were the key to my success as they put up with me all this time, not always to their liking. My grandparents have also been there for me all this time, and the realization of my goals would not have been possible without them. I would also like to acknowledge my beautiful fiancée, Jennifer, as in the past year our relationship has grown and now we are about to be married. She is my very special friend and my support.

This Dissertation would not have been possible without the help of my academic advisor, Dr. M. Pınar Mengüç who gave me the opportunity to pursue my degree in the exciting new area of Nanotechnology. I would also like to thank my co-worker Dr. Basil T. Wong, as this work is the successful continuation of his modeling efforts based on the Monte Carlo methods. Also, I thank Dr. R. Ryan Vallance and Mr. King-Fu Hii for the helpful discussions related to the modeling of field-emission from carbon nanotubes. Finally, I would like to thank my Ph.D. committee members Dr. Stephen E. Rankin, Dr. L. S. Stephens and Dr. Dusan P. Sekulić, and the outside examiner Dr. Zhi Chen, for their critical review of my work.

## TABLE OF CONTENTS

ACKNOWLEDGEMENTS .....	iii
TABLE OF CONTENTS.....	iv
LIST OF TABLES.....	vi
LIST OF FIGURES .....	vii
NOMENCLATURES .....	xiii
PREFACE.....	1
CHAPTER 1 INTRODUCTION.....	3
1.1 Nanomanufacturing using electron beams.....	3
1.2 Phase change and material removal in the nanoscale.....	5
CHAPTER 2 ELECTRON FIELD-EMISSION FROM CARBON NANOTUBES.....	8
2.1 Theoretical Background.....	8
2.2 Heat Transfer Models .....	15
2.3 Thermophysical Properties .....	18
2.4 Electron Trajectories.....	19
2.5 Finite Element Methods.....	20
2.6 Field-Emission Simulations and Experimental Validation.....	22
2.6.1 Electro-static calculations .....	22
2.6.2 Heat transfer calculations.....	25
2.7 Geometrical effects.....	27
2.7.1 Effects on electro-statics.....	27
2.7.2 Electron Trajectories and Deposition Profiles .....	29
2.7.3 Heat Transfer .....	29
2.8 Comments .....	32
CHAPTER 3 ELECTRON ENERGY DEPOSITION IN METALS AND HEAT TRANSFER MODELS.....	53
3.1 Electron beam propagation .....	53
3.2 Electron deposition profiles as a function of CNT geometry .....	54
3.3 The Two-Temperature Model.....	55
3.3.1 Electronic Properties.....	57
3.3.2 Heating of an Au workpiece with a single CNT.....	59
3.4 Electron Field-Emission from multiple CNTs.....	61
3.5 Comments .....	64
CHAPTER 4 MOLECULAR DYNAMICS THEORY.....	73
4.1 An Adiabatic Theory of Lattice Vibrations .....	73
4.2 Interatomic Potential.....	75
4.3 Integration of Equations of Motion.....	76
4.4 Boundary Conditions .....	77
4.5 Statistical Ensembles .....	78
4.6 Analysis of Atomic Trajectories.....	78
4.6.1 Equipartition Theorem and the Virial .....	79
4.6.2 Determination of Phase Change.....	79

4.7 MD codes .....	81
4.7.1 Bulk Simulations.....	82
4.7.2. Surface Simulations .....	83
4.8 Comments .....	85
CHAPTER 5 THE TWO TEMPERATURE MODEL COUPLED WITH MOLECULAR DYNAMICS: A HYBRID CONTINUUM-DISCRETE NUMERICAL APPROACH...	91
5.1 Coupling of the TTM with MD .....	91
5.2 Numerical Considerations.....	95
5.2.1 One-Dimensional (1D) Problems .....	95
5.2.2 Three-Dimensional (3D) Problems.....	96
5.3 Simulations of Laser Heating.....	98
5.4 Comments .....	101
CHAPTER 6 1D SIMULATIONS OF ELECTRON HEATING USING THE HYBRID TTM-MD METHOD .....	107
6.1 Problem settings.....	107
6.2 One-dimensional temperature and pressure spatial-temporal profiles.....	109
6.3. Structural Changes.....	111
6.4. Comments .....	114
CHAPTER 7 NANOMACHINING OF METALLIC SURFACES USING A HIGHLY FOCALIZED ELECTRON BEAM.....	125
7.1 Problem settings.....	125
7.2 Numerical model settings .....	126
7.3 Continuum calculations with the TTM.....	126
7.4 Nanostructure formation .....	129
7.5 Pressure and temperature profiles.....	132
7.6 Comments .....	135
CHAPTER 8 ELECTRON FOCUSING TECHNIQUES AND FABRICATION OF ELECTRON GUNS.....	145
8.1 Electron beam lithography systems .....	145
8.2 Electro-static lenses and emission from multiple CNTs.....	146
8.2.1 Preliminary modelling of electro-static lenses.....	147
8.3 Comments .....	149
CHAPTER 9 SUMMARY.....	156
9.1 Conclusions.....	156
9.2 Future work.....	157
9.2.1 Accurate electron deposition profiles .....	157
9.2.2 Extension of hybrid TTM-MD method to other materials.....	158
9.2.3 Experimental verification of electron beam based nanomachining.....	158
9.2.4 Exploration of novel focusing systems for parallel electron beam nanomachining.....	159
9.2.5 Thermodynamic analysis of phase change at the nanoscale.....	159
REFERENCES .....	160
VITA .....	173

## LIST OF TABLES

Table 2.1	Thermophysical properties.....	34
Table 3.1	Material constants used for TTM calculations.....	66
Table 6.1	Domain size used in the simulations.....	118
Table 8.1	Geometrical combinations used for electro-static problem in Fig. 8.3.....	153

## LIST OF FIGURES

Figure 1.1 Nanomachining concept as proposed by Vallance et al. (2003) .....	7
Figure 2.1 a) Two flat plates separated by a finite distance in the vacuum; b) energy diagram for a); c) CNT placed on top of a flat plate and separated by a finite distance from second plate; d) energy diagram for c). .....	35
Figure 2.2 Potential energy diagram for defining the work function (Tsukada 1983) .....	36
Figure 2.3 Side-view schematic of the electron stream and radial coordinate at the surface of the workpiece (Sanchez et al. 2007).....	37
Figure 2.4 SEM image of CNT attached to an etched tungsten probe. The CNT has dimensions of ~ 60 nm in diameter and 2.1 $\mu\text{m}$ in length. The protruding length is ~ 600 nm. ....	38
Figure 2.5 a) Geometry of the CNT attached to the tungsten filament. b) attachment point. The model is axi symmetric with the revolving axis depicted as $r = 0$ . The dimensions are in meters.....	39
Figure 2.6 Meshing used in the simulations for a CNT with a) closed tip; b) open tip, 10 nm wall thickness.....	40
Figure 2.7 Solution methodology of the finite element problem discussed in Section 2.5.....	41
Figure 2.8 a) Electric field distribution on the CNT's tip (inset is in meters). b) Log of the current density on the CNT's tip. The gap distance is 13.43 $\mu\text{m}$ and the plots correspond to 70, 100 and 140 V. Figures a) and b) are enlarged from the inset in a). The axis of symmetry is at $r = 0$ . The dashed line can be used for reference as the values indicated for each intersection correspond to the magnitudes of the normal electric field or current density at that point. The dashed line can be rotated on the center of the wall of the CNT to give the values of the electric field or current density at the intersection points. The values shown correspond to the values of the electric field and current density at that particular intersection (Sanchez et al. 2008a).....	42
Figure 2.9 a) Emitting area as a function of the applied voltage for a separation distance of 13.43 $\mu\text{m}$ . b) Emission current vs. voltage. The points correspond to the experimental data by Hii et al. (2006). .....	43
Figure 2.10 a) Electrons that are emitted from a radial location on the tip (abscissa) impact at a radial location on the workpiece (ordinate). The inset has the same dimensions. b) Current density on the workpiece mapped following (Sanchez et al. 2007). The axis of symmetry is at $r = 0$ . The separation distance is 13.43 $\mu\text{m}$ . ....	44

Figure 2.11 a) Maximum temperature vs. applied voltage. b) Comparison between the Nottingham effect and the Joule heating. ....	45
Figure 2.12 Comparison between the temperature on the tip and the inversion temperature, Eq. (2.19). ....	46
Figure 2.13 a) Comparison between the total emission current from integrating Eqs. (2.11) and (2.12) with the experimental data of Hii et al. (2006). The inset has the same dimensions. b) Near field thermal radiation effects compared based on a constant factor. The applied voltage is 130 V. ....	47
Figure 2.14 Field enhancement factor contour plots for a CNT to a tungsten filament to show the effect of length of the CNT and gap distance from the anode. The radius of the CNT is 30 nm; the minimum gap distance and length considered were 500 nm. a) open tip with a wall thickness of 5 nm; b) closed tip. ....	48
Figure 2.15 Comparison between the emission characteristics [ $I(V)$ plot] between an open ended and closed CNT with length of 2 $\mu\text{m}$ , radius of 50 nm and gap distance of 18 $\mu\text{m}$ . ....	49
Figure 2.16 Radial profile of electrons on the workpiece as a function of electron emission from a particular polar angle on the tip (see Fig. 2.3). a) effect of radius of the CNT; b) effect of length of the CNT; c) effect of the gap distance; d) effect of the applied voltage. In every case, all other geometrical parameters remained constant. ....	50
Figure 2.17 a) Maximum temperature distribution vs. emission current for different geometries of the CNT. b) Comparison between the heating sources acting on the CNT. The Joule heating term was integrated over the entire volume of the CNT and the tungsten filament, whereas the Nottingham effect was integrated over the surface of the CNT. For all cases the CNT had a radius of 50 nm and wall thickness of 10 nm. In b) all the cases shown in a) are considered. Different shapes of the tip do not have any significant effect on these results. ....	51
Figure 2.18 Maximum temperature distribution vs. emission current for different geometries of the CNT: a) effect of CNT radius; b) effect of wall thickness. In a) the wall thickness remained constant at 10 nm and in b) the outer radius of the CNT was fixed at 50 nm. ....	52
Figure 3.1 Back scattering electron yield as a function of the electron-beam energy for a) Au and b) Ni. The indicated references can be found in the compilation by Joy (2001). The line is just a guide to the eye. ....	66
Figure 3.2 Electron distribution (in $1/\text{nm}^3$ normalized using the initial kinetic energy of electrons) inside the workpiece for various applied voltages, gap distances and tip geometries: a) 300 V, 50 nm gap, round tip; b) 300 V, 50 nm gap, flat tip; c) 50 V, 10 nm	



gap, round tip; d) 50 V, 10 nm gap, flat tip. The axis are in nm and in all cases the CNT had a radius of 50 nm and a length of 4 $\mu\text{m}$ .....	67
Figure 3.3 a) Electron spread on the surface of the workpiece. b) Electron energy density ( $1/\text{nm}^3$ ) obtained from the MC solution of the EBTE based on the input profile in a). The axes are in nm. ....	68
Figure 3.4 Field-emission from an array of CNT grown on a substrate. ....	69
Figure 3.5 Radial profile of electrons on the workpiece as a function of electron emission from a particular polar angle on the tip. In all cases the applied voltage was 200 V and the gap distance 300 nm. The results are shown for a single CNT and for the CNT in the center with the effect of the emission of the CNTs around it separated by different distances. The inset shows the initial launching positions of the electrons on the periphery of the CNT tip. ....	70
Figure 3.6 a) Normalized amplification factor as a function of the intra-tubular distance. b) Field-emission current on the CNT in the center as a function of the intra-tubular distance calculated following the methods in (Sanchez and Mengüç 2008b). ....	71
Figure 3.7 Electron energy density deposited inside a gold thin film for a single CNT emitter and multiple emitters separated by intra-tubular distances indicated in the plot. These results suggest that the electron deposition profiles are not a function of the array geometry. ....	72
Figure 4.1 Periodic boundary condition used in molecular dynamics simulations .....	86
Figure 4.2 Equilibrium positions of atoms in the FCC structure. The arrows indicate the directions of vectors along the equilibrium lines.....	87
Figure 4.3 Common trends of the RDF: a) Solid phase; b) Liquid phase .....	88
Figure 4.4 Linear thermal expansion for Cu, Ag, and Au. The vertical axis applies to Au and the other curves are offset by 0.02. The experimental data from (Touloukian 1975) are plotted as points, and the calculated values are plotted as curves.....	89
Figure 4.5 Phonon modes of the first atomic layer of Cu(100) at position X of the surface Brillouin zone: a) phonon frequency as a function of temperature; b) spectral intensity at 300 K.....	90
Figure 5.1 Schematic showing the system and our solution scheme. The electronic system is simulated using a finite difference scheme (FD). An energy beam (laser or electron) irradiates the electronic system with normal incidence. The atomic system is treated by a MD scheme. Electronic and atomic systems are coupled by the electron-phonon coupling.....	102

Figure 5.2 Schematic of the hybrid continuum-MD approach. Each discrete element of the continuum model contains initially 109 atoms. ....	103
Figure 5.3 Comparison between numerical methods to predict the electron and lattice temperatures for a laser pulse of 200 fs with a fluence of $130 \text{ J/m}^2$ on a 50 nm thin film of Au: a) electron temperature; b) lattice temperature. ....	104
Figure 5.4 Electron and lattice temperature on the top and bottom surfaces of a) gold and b) nickel after laser irradiation with $130 \text{ J/m}^2$ of absorbed fluence with pulse duration of 200 fs.....	105
Figure 5.5 Lattice temperature of a 50 nm thin film of gold when heated by a 200 fs laser pulse with an absorbed laser fluence of $130 \text{ J/m}^2$ . Different lattice heat capacities are compared when using Eq. (5.9) as the coupling between MD and the TTM. ....	106
Figure 6.1 Electron energy density for Ni and Cu as a function of the depth in the film	117
Figure 6.2 Transient lattice temperature profiles during heating of a 100 nm thin film by an array of 10000 CNTs with 300 V of applied voltage and 300 nm gap distance. a) Cu film; b) Ni film.....	118
Figure 6.3 Transient pressure profiles during heating of a 100 nm thin film by an array of 10000 CNTs with 300 V of applied voltage and 300 nm gap distance. a) Cu; b) Ni. Positive values denote compression, negative values denote tension.....	119
Figure 6.4 Spatial-temporal profile of the normalized number density of the films during heating by an array of 10000 CNTs with 300 V of applied voltage and 300 nm gap distance. a) Cu film; b) Ni film. The dotted line delineates the solid-liquid interface and the dashed line the liquid-vapor interface. ....	120
Figure 6.5 Structural analysis of the Cu film during the heating of field-emission by an array of 10000 CNTs with an applied voltage of 300 V and 300 nm gap distance. a) Order parameter and b) in-plane radial distribution function at 100 ps at various depths.....	121
Figure 6.6 Structural analysis of the Ni film during the heating of field-emission by an array of 10000 CNTs with an applied voltage of 300 V and 300 nm gap distance. a) Order parameter and b) radial distribution function at 100 ps at various depths. ....	122
Figure 6.7 Velocities of the solid-liquid and liquid-vapor interface in a) Cu and b) Ni, after heating with 10000 CNT with 300 V and 300 nm of separation distance.....	123
Figure 6.8 Time required to achieve melting at a given depth of a thin film as a function of the number of CNTs used for electron emission: a) Cu, b) Ni. ....	124
Figure 7.1 Electron energy density as a function of the applied voltage based on MCM simulations a) Au; b) Ni.....	137

Figure 7.2 Temperature profile along the radius and axis of the films: a) and c) (left column) correspond to Ni; b) and d) (right column) correspond to Au in the radial and axial directions, respectively. For each accelerating voltage heating powers of 0.5 W (blue), 1 W (green) and 10 W (red) were considered for the electron beam. In all the plots, the $x$ - axis is in nm and the $y$ - axis in K. ....	138
Figure 7.3 Snapshots of atomic positions of Ni workpiece in an $x$ (horizontal: -20 – 20 nm) – $y$ (vertical: -10 – 10 nm) plane 0.352 nm thick centered at $z = 0$ nm. Simulations are for highly focused electron beam with an accelerating voltage of 250 V and heating power of 0.5 W. ....	139
Figure 7.4 Melting sequence depicted within Ni film by the order parameter in an $x$ (horizontal: -37 – 37 nm) – $y$ (vertical: -27 – 10 nm) plane 0.352 nm thick centered at $z = 0$ nm. Below 0.04 the material is considered a liquid. Simulations correspond to highly focused electron beam with an accelerating voltage of 250 V and heating power of 0.5 W.....	140
Figure 7.5 In plane radial distribution function at four locations of Ni film in the $x$ - $y$ plane for various times during the nanomachining sequence. Conditions are the same as in Figs. 7.3 and 7.4.....	141
Figure 7.6 a) Position of solid-liquid interface in Ni film at various times. The marks correspond the the actual position and the lines are polynomials of 4 <sup>th</sup> order that were used to fit the data. b) Speed of the melting front at the center of the workpiece. The inset shows its position as a function of time. In both cases, the results show the $x$ - $y$ plane centered at $z = 0$ . Conditions are the same as in Figs. 7.3 and 7.4.....	142
Figure 7.7 Stress profile on the Ni workpiece during the nanomachining process. Positive stresses are compressive; negative are tensile. Conditions are the same as in Figs. 7.3 and 7.4.....	143
Figure 7.8 Temperature rise on the Ni workpiece during the nanomachining sequence. Conditions are the same as in Figs. 7.3 and 7.4.....	144
Figure 8.1 Electron beam processing equipment. Electrons are generated and accelerated by the electron gun and guided through the column by the electromagnetic lenses and the deflection scan coil. Both the scanning system and the $x$ - $y$ - $z$ stage are used to define the working point on the workpiece (Wang et al. 2003). ....	152
Figure 8.2 a) Cross section SEM showing the undercut of the poly-Si and SiO <sub>2</sub> beneath the resist. b) Tilted 45° view of the microcathode after nanotube growth. c) Top view clearly shows the centrally located nanotubes (bright dots) with respect to the gate hole. d) Cross section SEM of the microcathode (Teo et al. 2003).....	153
Figure 8.3 Single CNT vertically aligned with an extraction gate and a focusing gate. ....	154

Figure 8.4 Effect on the total emission current of the different cases shown in Table 8.1. The dashed line indicates the cutoff below which the emission current cannot be measured. .... 155

## NOMENCLATURES

$V$	applied voltage (V)
$F$	electric field strength (V/m)
$e$	electron charge ( $1.602 \times 10^{-19}$ C)
$y$	functional form of field strength
$t(y)$	functional form of field strength
$v(y)$	functional form of field strength
$D$	tunneling probability
$W$	total electronic energy (eV)
$p(x)$	electron momentum perpendicular to surface (eV)
$k_F$	Fermi wave number (1/m)
$\hbar$	Orbital Planck constant ( $1.054 \times 10^{-34}$ Js)
$N(F,T,\Phi)$	Supply function
$p$	Non-dimensional parameter
$J$	Electron current density ( $A/m^2$ )
$d$	Function form of field strength (eV)
$s$	Separation distance (m)
$q''$	Heat flux ( $W/m^2$ )
$I$	Total field-emission current (A)
$R$	Electrical resistance ( $\Omega$ )
$Q'''$	Joule heating ( $W/m^3$ )
$C$	heat capacity ( $J/m^3K$ )
$T$	temperature (K)
$k$	thermal conductivity ( $W/mK$ )
$J_i$	Radiosity from surface $i$ ( $W/m^2$ )
$F_{ij}$	Radiation view factor between surfaces $i$ - $j$
$A_i$	Area of surface $i$
$f$	Particle distribution
$G$	electron-phonon coupling constant ( $W/m^3K$ )
$S$	source term ( $W/m^3$ )
$t$	time (s)
$m$	mass (kg)
$r$	atomic position (m)
$U$	interatomic potential (eV)
$N$	number of atoms
$v$	atomic velocity (m/s)
$V$	volume ( $m^3$ )
$L$	length (m)
$x$	coordinate in x-direction (m)
$y$	coordinate in y-direction (m)
$z$	coordinate in z-direction (m)
$a_0$	lattice constant (m)
$A$	matrix element (m)
$k_B$	Boltzmann's constant ( $1.381 \times 10^{-23}$ J/K)

$P$	pressure (GPa)
$g(\mathbf{r})$	Radial distribution function
$V_1$	Voltage at extraction gate
$V_2$	Voltage at focusing gate
$r_1$	Radius of extraction gate
$r_2$	Radius of focusing gate
$z_1$	Height of extraction gate
$z_2$	Height of focusing gate
$z_3$	Separation between focusing gate and workpiece

#### Greek symbols

$\Phi$	work function (eV)
$\epsilon_0$	Dielectric constant of vacuum ( $8.85 \times 10^{-12} \text{ Fm}^2$ )
$\lambda$	Field amplification factor
$\rho_e$	Resistivity ( $\Omega\text{m}$ )
$\sigma$	Stephan-Boltzmann constant ( $5.67 \times 10^{-8} \text{ W/m}^2\text{K}^4$ )
$\epsilon$	Emissivity
$\rho$	Density ( $\text{kg/m}^3$ )
$\chi$	velocity rescaling factor
$\omega$	relaxation parameter
$\Psi$	order parameter

#### Subscripts

$F$	Fermi
$I$	inversion
$N$	Nottingham
$W$	Tungsten
$\infty$	infinity
$i$	index
$j$	index
$k$	index
$e$	electron
$l$	lattice

## PREFACE

The purpose of this dissertation is to study the different aspects of a process of electron heating and nanomachining of metallic surfaces using electrons that result from a phenomenon of field-emission from a carbon nanotube (CNT). It comes from the desire to understand, develop a knowledge base and determine the feasibility, experimental requirements, limitations and potential applications of a process that was envisioned as a tool to pattern surfaces in the nanoscale.

This dissertation is divided into several Chapters that give the required background of the physics of the process of electron field-emission from CNTs, transport equations used to model heat transfer phenomena inside the CNT and the workpiece, and numerical schemes used to solve these equations. It begins with an introduction to nanomanufacturing and a brief overview of different tools available, emphasizing tools based on electron beams. It is followed by two Chapters solely devoted to describe the process of field-emission and the effects that the geometry of the CNTs have on the resulting electron emission. All the subsequent models used to study the heating of metallic surfaces due to these electrons, are based directly on realistic electron emission from single or multiple CNTs, the latter organized in controllable arrays. In pursuing this work, considerable effort was given to validate the numerical approaches used with available experimental data found in the literature.

Following the discussions of electron field-emission, the next Chapters describe the transport equations used to study the heating of metallic surfaces. More importantly, the combination of different numerical approaches, one based on a continuum formulation and the other based on discrete-atomistic approximation, allows to study, with high confidence, the process of material removal and phase change. This effort is essential to the advances of the field of nanomanufacturing, especially if one needs to design new tools and predict their performance.

Finally, recommendations that will guide future experiments and conclusions based on the modeling efforts carried in this work are given in the last two Chapters.



## CHAPTER 1 INTRODUCTION

Nanomanufacturing is a research area that has been growing rapidly in recent years. The current demands of industry require the precise modification of surfaces to make holes, lines, arrays, structures and so on, that can be used for a diverse number of applications. Thus, the desire to pattern in the nanoscale is the main driver behind the development of new manufacturing tools. The tools available to accomplish these tasks are currently being developed and improved.

The most traditional and well documented tool used in microfabrication is photolithography which consists in using light from a laser channeled through a photomask with a given pattern to expose this pattern onto a resist. This resist is usually a photosensitive polymer that is spun on top of a substrate, such as SiO<sub>2</sub>. This is followed by chemical processes that eventually lead to getting the pattern onto the substrate. In the microprocessor industry, the use of this technique allowed for the rapid development of the transistor. However, with the desire of continuously shrink devices to give faster, more powerful processors, microfabrication techniques will need to evolve accordingly.

### 1.1 Nanomanufacturing using electron beams

An established technology such as electron-beam lithography (EBL) has been for a long time a very common candidate to meet the challenge of the continuously shrinking devices. One can find many books today that give extensive overviews of the details of EBL and here only the most important features are summarized (Campbell 2001; Franssila 2004). EBL utilizes high energy electrons to expose a resist which can be later developed to resolve a particular pattern. By coating a surface with such a resist and combined with several chemical etching techniques one can finally obtain a desired pattern on top of a surface such as a metal or semiconductor. Electron-beam resists are usually polymers that are electron-sensitive rather than light-sensitive used in photolithography.

Since the EBL is a serial process, it takes a very long time to produce a given pattern which in an electronic device could be very complex. Thus, EBL technology is traditionally adapted to manufacture photomasks that are then used as templates to print patterns on surfaces using photolithography. From then on, one needs to expose the resist to high energy electromagnetic radiation such as X-rays or extreme ultra-violet (EUV), as the diffraction limit of light poses a limit on the minimum feature size that can be resolved. Though costly, the main advantage of photolithography with X-rays or EUV is that it can be done in parallel thus allowing the fabrication of multiple devices in a single exposure. A comprehensive review that discusses and compares all the methods available that take advantage of an electron beam to pattern surfaces or materials was given by Rajurkar et al. (2006). Other techniques are currently being investigated that are aimed to overcome the diffraction limit of light by taking advantage of near field radiation effects (Grafstrom 2002; Huang et al. 2002).

Some time ago, Vallance et al. (2003) envisioned a process dubbed “nanomachining” that utilizes electrons to induce phase change of a nanometer-sized spot on a metallic surface. The process requires laser heating of a large (micron-sized spot) to raise the temperature of a metallic workpiece to the melting threshold, and then electrons emitted from a CNT would provide the required amount of energy to achieve melting and phase change of a nanometer sized spot on the surface. The CNT was then also considered as a characterization tool that could be used in STM mode, so that visualization of the desired pattern could be achieved. Figure 1.1 shows a schematic of the original concept.

Considerable work in the modeling of this process has already been done as outlined by Wong and Mengüç (2008). With the use of continuum models based on the basic transport equations, the heat transfer problem on a metallic workpiece was studied. First, a numerical approach was developed to solve the electron-beam Boltzmann transport equation (EBTE) based on a Monte Carlo method (Wong and Mengüç 2004). This method gave insight into how the electrons are deposited inside the workpiece, assuming that their initial positions on the surface followed a predetermined profile. While this work was extensive, it began with the assumption of a given electron profile on the

surface of the workpiece, which in general is not known. Another assumption regarding the amount of heating power available to the electrons was made. For a given accelerating voltage, it was required to assume a field-emission current, so that the total heating power available to the electrons, and thus for the heat transfer problem, was given by Ohm's law. The solution of the heat transfer problem required yet more assumptions as to the thermophysical properties of the workpiece, and how they evolved as a function of the temperature (Wong et al. 2004, 2006). It needs to be understood that even with these apparent limitations, the previous work represents the state-of-the-art in the field, and tackling existing problems with this formulation is not trivial by any means. Still, there is room for improvement, and so several questions can be asked.

First, in the modeling efforts carried so far, the connection between the electron field-emission from the CNT and the heating of the workpiece was not established. Determining this connection is crucial because it allows us to make accurate predictions for potential experiments. The real profile of the electron beam that reaches the surface of the workpiece and how it is affected by parameters such as the gap distance, applied voltage, and geometry of the CNT, need to be known. Also determining what happens to the CNT during the process is desired. This is important, because it allows the determination of the robustness of the CNT and its effectiveness as a potential source of electrons for nanomachining. Finally, what happens to the workpiece when it is heated by an electron beam needs to be studied with atomistic detail. If there is phase change such as melting or vaporization, how can it be characterized at the nanoscale? If material is removed, how much energy is required to achieve that?

## 1.2 Phase change and material removal in the nanoscale

Throughout the years, many explanations of melting phenomena have been sought. These definitions are usually provided for bulk materials, i.e. far away from a free surface. One of these definitions is based on the Lindemann criterion where melting is said to start when the RMS displacement of the atoms exceeds  $\sim 10\%$  of the lattice constant (Lindemann 1910) or  $\sim 11.83\%$  for FCC materials (Cho 1982). Another one, the Born criterion, defines the mechanical melting as the failure of the crystal which occurs

when the shear strength modulus vanishes at a particular temperature, e.g. the melting point (Born 1939). Free surfaces, however, exhibit a different behavior. When a crystal is heated to its bulk melting point, melting starts at the free surface (van der Veen 1999). Therefore, the definitions for bulk melting may not be applicable to these cases and require independent evaluations. Specific experiments on surface melting were reported by Pluis et al. (1987, 1990); they found that surface melting is dependent on the crystallographic orientation of the surface. Further studies for Pb (van Pinxteren and Frenken 1992; van Pinxteren et al. 1994) and for Al (Vandergon et al. 1990) were conducted finding similar surface melting dependence on the crystallographic orientation. More recently, Siwick et al. (2004) “visualized” the melting process of an Al crystal by means of femtosecond electron diffraction. They were able to capture in real time the evolution of the correlation functions derived from the atomic motion.

The results from the studies mentioned above are applicable only to the cases when the material, be it a bulk or a free surface, is heated uniformly. A surface process, such as nanomachining using field-emission electrons is a more disruptive process, as the electron beam incident on the workpiece has limited spatial extent, which yields a clear boundary. Within the symmetry axis of the beam, the melting, and ablation or material removal, or a complicated combination of the two at the nanoscale level are explored. As we move away from the center, the problem becomes much more complicated to have an unambiguous demarcation of phase change contours. The aim of this dissertation is to find an answer to this and the other questions posed.

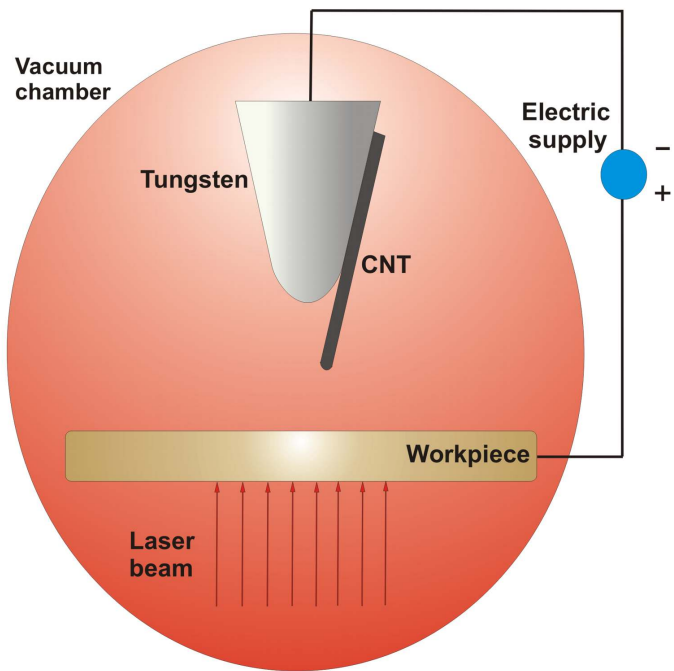


Figure 1.1 Nanomachining concept as proposed by Vallance et al. (2003)

## CHAPTER 2 ELECTRON FIELD-EMISSION FROM CARBON NANOTUBES

In this Chapter, the concept of electron field-emission and discuss the physics of the phenomena obtained from CNTs is introduced. The numerical method that is used throughout this Dissertation to study the effects that emission of electrons has on the CNT is presented here. Answers to questions such as, what is the effect of the geometry of the CNT on the emitted electrons and what happens to the CNT during the process are sought. This approach allows the determination of the potential robustness and limitations of the field-emission process with the aim of guiding future experiments.

### 2.1 Theoretical Background

Field-emission of electrons from a surface involves quantum tunneling through a potential barrier into vacuum. The potential field is created by a workpiece at a lower electron potential. Fowler and Nordheim (1928) described the physics of field-emission from a planar metallic surface. Later, it was found that elongated emitter structures can substantial enhance emission by an increasing the local electric field near the tip of the emitter (Spindt 1968). In Fig. 2.1 a comparison between the field-emission from two flat plates and field-emission from a sharp needle (such as a CNT) are depicted.

A distinction has to be made between two other types of emission of electrons from a surface (Gomer 1993):

- a. Thermionic emission occurs when a metal is heated until a sufficient number of electrons acquire kinetic energies such that  $E > \Phi + E_f$ , where  $\Phi$  is the work function and  $E_f$  is the Fermi energy.
- b. Photoemission occurs when the surface of a metal is irradiated with light of energy  $h\nu > \Phi$ . The threshold wavelength for clean metals lies in the visible or near ultraviolet.

While in thermionic and photoemission electrons are given enough energy to overcome the potential barrier, in field-emission, this barrier is deformed so strongly that unexcited electrons can leak out through it, in a quantum–mechanical phenomenon called tunneling. Thus, field-emission is defined as the emission of electrons from the surface of a condensed phase into another phase, usually a vacuum, under the action of a high (3-9 V/nm) electrostatic field (Murphy and Good 1956).

The spontaneous emission of electrons into vacuum is a function of three physical parameters (Gomer 1993; Fransen 1999): the emitter temperature  $T$ , the electric field strength on the emitter surface  $F$ , and the work function of the material  $\Phi$ . The work function was classically defined as the amount of energy to bring an electron in the solid to a distance far away from the surface. In field-emission one often encounters the work function on an atomic scale, although it has never been defined before. Here, the distance to bring an electron out of solid should be comparable to the lattice size.

As shown in Fig. 2.2, electrons in the solid are confined in a potential well whose depth  $\Delta v_{eff}$  is the sum of the cohesive force potential  $|V_{xc}(\rho_+)|$  and the electrostatic force potential  $\Delta\phi$ . The former is a bulk property that arises from exchange and correlation interactions among electrons in the solid, while the latter is a surface property that depends on surface atomic structures. Electrons in the solid are filled in the potential well following their wave number in order until the Fermi wave number  $k_F$  is reached. Thus, the electron filling is completed when the electron with the energy  $(\hbar^2/2m)k_F^2$  is filled in place. The work function is then defined as (Tsukada 1983)

$$\Phi = \Delta v_{eff} - \frac{\hbar^2}{2m} k_F^2 \quad (2.1)$$

The origin of the electrostatic force is the spill-out of electrons in the solid to vacuum. Spill-out electrons and positive charge left behind in the solid build up an electric dipole field that then suppresses electrons coming out of solid. As spill-out electrons smear out the space outside ion cores, the surface averaged spill-out electron density should vary with the surface atom concentration. Closely packed surfaces having less smearing action

feel greater electrostatic force than loosely packed surfaces. This creates the dependence of the work function on crystal planes.

The electric field  $F$  can be determined from the electrostatic analysis on the vacuum surrounding the CNT. Assuming that space charge effects are negligible, the electrostatic equation is to be solved (Edgcombe 2001):

$$\nabla^2 V = 0 \quad (2.2)$$

with  $\nabla^2 V = \nabla F$ , where  $V$  is the applied voltage. The boundary conditions for the solution of Eq. (2.2) are established by setting the surface of the CNT to ground potential (0 V) and setting the workpiece anode surface to a bias voltage of  $V_e$  (Edgcombe 2001; Walker et al. 2004; Zheng et al. 2004). Boundaries far away from the cathode and anode are considered to be electrically insulated to account for the vacuum. Space charge effects close to the CNT surface or variations in the field  $F$  due to electron emission are neglected in this formulation since the error in this assumption is small (Walker et al. 2004).

The total electric current per unit area  $J(F, T, \Phi)$  is found by integrating over all accessible energies, the product of the charge of an electron  $e$ , the number per second per unit area incident on the barrier  $N(F, T, \Phi)dW$ , and the transmission coefficient  $D(F, W)$  (Murphy and Good 1956)

$$J(F, T, \Phi) = e \int_{-W_a}^{\infty} D(F, W) N(T, \Phi, W) dW \quad (2.3)$$

with  $W = [p^2(x)/2m] + V(x)$  where  $x$  is the coordinate normal to the surface and out of the metal,  $p(x)$  is the electron momentum normal to the surface,  $V(x)$  is the effective electron potential energy, and  $W_a$  is the effective constant potential inside the metal. The transmission coefficient  $D(F, W)$  represents the probability that an electron will tunnel from the solid into the vacuum. It depends strongly on the width of the potential barrier



encountered by the electron. A general form of the transmission coefficient can be obtained by considering the solution of the time-independent Schrodinger equation in potential barrier of height  $V(x) - W$  and width  $x_2 - x_1$  (Miller and Good 1953). Equation (2.4) is known as the Wentzel-Kramers-Brillouin (WKB) approximation (Miller and Good 1953).

$$D(F, W) = \exp \left[ - \int_{x_1}^{x_2} \sqrt{\frac{8m}{\hbar^2} |V(x) - W|} dx \right] \quad (2.4)$$

where  $\hbar$  is Planck's constant ( $6.626 \times 10^{-34}$  Js) divided by  $2\pi$ . The free-electron model gives the following expression for the number of electrons per second per unit area having energy within the range  $dW$  incident on the barrier, also known as the supply function (Fowler 1952).

$$N(T, \Phi, W) dW = \frac{4\pi m k_B T}{h^3} \ln \left\{ 1 + \exp \left[ - \frac{(W - \Phi)}{k_B T} \right] \right\} dW \quad (2.5)$$

The integration of Eq. (2.3) can now be done assuming some function for the potential energy of electrons  $V(x)$ . For the case of two parallel plates in a vacuum (Fig. 2.1a) one can assume (Murphy and Good 1956)

$$V(x) = \begin{cases} -e^2(4x)^{-1} - eFx, & \text{when } x > 0 \\ -W_a, & \text{when } x < 0 \end{cases} \quad (2.6)$$

where  $-e^2(4x)^{-1}$  is the contribution from the image force and  $-eFx$  is the contribution from the externally applied field  $F$  as shown in Fig. 1b. It has been shown experimentally, that one can use this same formulation for the case of field-emission from a CNT, considering that the applied field  $F$  is enhanced by geometrical effects (Spindt 1968; Edgcombe 2001; Bonard et al. 2002; Hii et al. 2006), even though the floating sphere approximation has also been used (Walker et al. 2004; Shang 2007). This ‘‘field enhancement factor’’ is discussed at the end of this section. Using the potential function defined in Eq. (2.6) the total current density is given as (Murphy and Good 1956)

$$J(T, F, \Phi) = \frac{4\pi m_e k_B T e}{h^3} \int_{-\infty}^{W_i} \frac{\ln \{1 + \exp[-(W - \Phi)/k_B T]\} dW}{1 + \exp\left[\left(\frac{4}{3}\right)\sqrt{2} \left(\frac{\hbar^4 F}{m_e^2 e^5}\right)^{-1/4} y^{-3/2} v(y)\right]} + \frac{4\pi m_e k_B T e}{h^3} \int_{W_i}^{\infty} \ln \{1 + \exp[-(W - \Phi)/k_B T]\} dW \quad (2.7)$$

where

$$W_i = -\sqrt{\frac{e^3 F}{8\pi\epsilon_0}} \quad (2.8)$$

$$y = \frac{1}{|W|} \sqrt{\frac{e^3 F}{4\pi\epsilon_0}} \quad (2.9)$$

and

$$v(y) = \begin{cases} \sqrt{1+y} \left[ E\left(\frac{1-y}{1+y}\right) - yK\left(\frac{1-y}{1+y}\right) \right], & y \leq 1 \\ -\sqrt{\frac{y}{2}} \left[ (y+1)K\left(\frac{y-1}{2y}\right) - 2E\left(\frac{y-1}{2y}\right) \right], & y > 1 \end{cases} \quad (2.10)$$

In Eq. (2.10)  $K$  and  $E$  denote the complete elliptic integrals of the first and second kind (Abramowitz 1964).

Numerical methods have been used in the past to solve Eq. (2.7) for a range of work functions, field strengths and temperatures (Paulini et al. 1993). However, a widely used approximation to this equation is the so-called Fowler-Nordheim approximation (Good 1956)

$$J(F, T) = J_0 \frac{\pi p}{\sin \pi p} \quad (2.11)$$

where  $p$  is a dimensionless parameter that measures the number of electrons emitted that have energies above the Fermi level due to the temperature (Fransen 1999). The total current density  $J_0$  at 0 K is given in Eq. (2.12) (Fowler and Nordheim 1928). The

functions,  $t(y)$  and  $v(y)$ , given in Eqs. (2.14) and (2.15), are slow varying functions of the field  $F$  and work function  $\Phi$  expressed in Eq. (2.13) (Good 1956).

$$J_0 = \frac{1.54 \times 10^{-6} F^2}{\Phi t^2(y)} \exp \left[ -\frac{6.83 \times 10^7 \Phi^{3/2}}{F} v(y) \right] \quad (2.12)$$

$$y = 3.7947 \times 10^{-4} \frac{F^{1/2}}{\Phi} \quad (2.13)$$

$$v(y) = 1 - 1.0125 y^{1.71} \quad (2.14)$$

$$t(y) = 1 + 0.1156 y^{1.4} \quad (2.15)$$

An expression for the dimensionless parameter  $p$  is given in Eq. (2.16), and it depends on the temperature  $T$  and the parameter  $d$ . A Taylor series expansion of the tunneling probability in the WKB approximation (Swanson et al. 1966) yields the expression for  $d$ , given in Eq. (2.17)

$$p = \frac{k_B T}{d} \quad (2.16)$$

$$d = 9.76 \times 10^{-9} \frac{F}{t(y) \Phi^{1.5}} \quad (2.17)$$

In Eqs. (2.11) through (2.17) the units are  $J, J_0$  (A/m<sup>2</sup>),  $F$  (V/m),  $\Phi, d$  (eV),  $T$  (K) and  $k_B$  ( $8.62 \times 10^{-5}$  eV/K) is Boltzmann's constant. Equation (2.11) breaks down at high temperatures when  $p \geq 1$  and it becomes unreliable when  $p$  exceeds about 0.7 (Fransen 1999). The dimensionless parameter  $p$  corresponds to a measure of the number of electrons emitted with energies above the Fermi level due to the effect of temperature. For field strengths considered in this work, which are typically below 8 V/nm, this corresponds to temperatures on the order of 1600 K. Results presented later suggest that the temperature of the CNT can reach this range, and so this limit on Eq. (2.11) provides an upper bound in the validity of these simulations. An effective value of  $p$  can be estimated by calculating the total emission current as a function of temperature,

integrating Eq. (2.11), and comparing it to the emission current obtained by integrating Eq. (2.12). The results are shown in a latter section. Paulini et al. (1993) studied the validity of Eq. (2.11) for a range of work functions and applied electric fields. They found that it deviates from the actual current density [Eq. (2.7)] when  $\Phi < 3.5$  eV and  $F > 9$  V/nm. This is limit is not of concern to the present work since lower fields are considered in this work and the work function of a CNT is typically  $\sim 4.7$  eV<sup>1</sup>.

Finally, the field amplification factor as defined by Hii et al. (2006) is calculated in Eq. (2.18)

$$\lambda = \frac{F}{V/s} \quad (2.18)$$

where  $s$  is the separation distance between the anode and the tip of the CNT. Enhancement of the field strength close to a very sharp tip during field-emission was first observed by Spindt (1968) and attributed mainly to geometrical effects of the emitter. Traditionally, this is calculated through the field enhancement factor defined as  $\gamma = Fd/V$  where  $d = s + h$  and  $h$  is the height of the CNT (Bonard et al. 2002). In this way, the field enhancement factor is defined as a function of the distance between two flat surfaces. When the separation distance is large,  $s \approx d$  and the two formulations are equivalent. However, for smaller distances, the amplification factor  $\lambda$  should approach unity (no amplification) as  $s$  approaches zero, but the enhancement factor  $\gamma$  mathematically approaches infinity or  $h/s$  as  $s$  approaches zero (Hii et al. 2006).

The field enhancement factor is an important quantity in field-emission because it relates the effects of the geometry to the current that can be obtained with given emitter in a specific experimental setting. This is because the field-emission current is an explicit function of the field strength [Eq. (2.7)]. The finite element solution of the electrostatic equation, Eq. (2.2), directly includes the amplified field strength  $F$  so that the amplification factor can be calculated.

---

<sup>1</sup> See Section 2.4 for a complete list of all thermophysical properties considered in this work

## 2.2 Heat Transfer Models

In 1936, Nottingham discovered that a heat flux is present during field-emission from tungsten filaments. Considering that the presence of the field-emission current should cause heating of the cathode, it was found that the temperature attained by the field emitter was in some instances less or more than that was predicted by traditional calculations. Charbonnier et al. (1964) found that there is a stabilizing factor provided by the energy exchange resulting from the difference between the average energy of the emitted electrons,  $E$ , and that of the replacement electrons,  $E'$  during the process. In general  $E'$  is taken as the Fermi energy  $E_f$ . Energy levels above  $E_f$  are empty, and in pure-field-emission at 0 K, all emitted electrons have less than the Fermi energy, and the Nottingham effect produces heating of the cathode. However, if the cathode temperature is increased (thermo-field-emission), energy levels above  $E_F$  become populated and contribute preferentially to the emission, causing a decrease in the average heat transfer per emitted electron. If the temperature of the emitter exceeds an “inversion” temperature  $T_I$ ,  $E$  becomes greater than  $E_F$ , reversing the effect and cooling the cathode. The inversion temperature can be quantized with (Charbonnier et al. 1964):

$$T_I = 5.67 \times 10^{-5} \frac{F}{\Phi^{1/2} t(y)} \quad (2.19)$$

This Nottingham effect therefore provides a heat flux  $q_N''$ , given in Eq. (2.20), that acts on the surface region where the field-emission occurs. It can be quantified with (Gratzke and Simon 1995):

$$q_N'' = \frac{J \varepsilon}{e} \quad (2.20)$$

where  $J$  is the current density given in Eq. (2.11),  $\varepsilon = -\pi p d \cot(\pi p)$  and  $e$  ( $1.602 \times 10^{-19}$  C) is the electron charge. If the temperature of the cathode  $T$  is such that  $T < T_I$  then the sign of the heat flux is positive and thus the Nottingham effect acts a heating mechanism. It will be a cooling effect when  $T > T_I$ .

The flow of current through the cathode also causes the temperature to rise due to Joule heating and it was discussed by different groups. Swanson et al. (1966) considered both the Nottingham effect and Joule heating in determining the temperature variation produced by the energy-exchange processes accompanying field-electron emission. In the case of the Nottingham effect, the energy exchange between the conduction electrons and the lattice is expected to occur within a fraction of an emitter-tip diameter (approximately 100 nm) because of the extremely short mean free path of conduction electrons near the Fermi energy with respect to electron-phonon and electron-electron interactions.

Gratzke and Simon (1995), on the other hand, found that the Joule heating due to field emitted electrons produces a negligible effect. They considered the emitter as a thin rod of gold of length  $l$  that was heated by a current density  $j$ , with boundary conditions  $\partial T/\partial x = 0$  at  $x = 0$  and  $T = 0$  at  $x = 1$ . They found that the temperature increase of the emitter due to Joule heating alone was almost negligible and they concluded that the Nottingham effect was responsible for heating the emitter.

The heat transfer in the cathode is modeled using the transient heat conduction equation with volumetric heat generation (Gratzke and Simon 1995; Huang et al. 2004; Yang 2005):

$$\rho C_p \frac{\partial T}{\partial t} = \nabla(-k\nabla T) + Q''' \quad (2.21)$$

where  $k$  is the thermal conductivity,  $\rho$  is the density,  $C_p$  is the specific heat,  $T$  is the temperature and  $Q'''$  is the volumetric heat generation term due to Joule heating. It is defined as

$$Q''' = \frac{I^2 R}{\mathcal{V}} \quad (2.22)$$

where  $I$  is the total emission current from integrating Eq. (2.11),  $R$  is the resistance and  $\mathcal{V}$  is the volume of the probe.

Recently, Yang (2005) studied the heat transfer on a single wall CNT (SWCNT) using the transient heat conduction equation [Eq. (2.21)] with heat generation. In his work, a 3D solution based on FEA was implemented considering that the finite elements had a hexagonal shape where each node corresponded to a carbon atom. The SWCNT simulated in that work had a radius between 1 to 1.5 nm. Also recently, Huang et al. (2004) analyzed a SWCNT with a finite difference solution of the 1D heat conduction equation for a CNT with radius of 10 nm. Even though these formulations are continuum approaches, their validity has been established by comparison with finer numerical methods such as discrete molecular-mechanical simulations based on quantum mechanics (Das and Wille 2002; Li and Chou 2003). Nevertheless, because these methods are more computationally expensive, the continuum approaches are still used when the dimensions of the CNTs are large, as in this work.

Equation (2.21) is subject to conduction and radiation boundary conditions. Because only a section of the tungsten filament is modeled, the heat conducted to the remainder part is modeled using Eq. (2.23)

$$q_w = \sqrt{h_r P k A_c} \frac{\cosh mL}{\sinh mL} (T - T_\infty) \quad (2.23)$$

where  $h_r = \varepsilon \sigma (T + T_\infty)(T^2 + T_\infty^2)$  is the equivalent radiative coefficient (Incropera 1996),  $A_c$  is the cross sectional area of the cylinder, and  $m^2 = h_r P / k A_c$ .

The radiation heat transfer from the cathode is also considered, although the near-field radiation effects are neglected. The radiative transfer exchange between the cathode and the anode is very complicated because of the small gap distance between them. It is known that when the distance between two hot bodies is smaller than the wavelength of the thermal radiation there exist radiation enhancement by tunneling of evanescent waves (Pendry 1999). The critical separation between the two bodies can be estimated from Wien's displacement law as  $T\lambda_T = 2898.8 \mu\text{m K}$ . Recently, Francoeur and Mengüç (2008) have found that the critical distance is actually three times larger than that predicted the Wien's law. This means that for  $T = 293 \text{ K}$ ,  $\lambda_T \sim 30 \mu\text{m}$ . The mathematical formulation to

study near field effects in radiative transfer is very cumbersome even for the relatively simpler case of two parallel plates (Francoeur and Mengüç 2008), let alone for cylindrical geometries. In this paper the radiosity node method is used to estimate the radiation exchange (Incropera 1996):

$$\frac{E_{bi} - J_i}{(1 - \varepsilon_i) / \varepsilon_i A_i} = \sum_{j=1}^N \frac{J_i - J_j}{(A_i F_{ij})^{-1}} \quad (2.24)$$

where  $E_{bi}$  is the irradiation,  $A_i$  is the total area, and  $\varepsilon_i$  is the emissivity of surface  $i$ ;  $F_{ij}$  is the shape factor between surfaces  $i$  and  $j$ ,  $J_k$  is the radiosity from surface  $k$  and  $N$  is the total number of surface. The formulation in Eq. (2.24) neglects any effects attributed to near field radiation. In order to estimate the error in our calculations the total radiative heat flux derived from Eq. (2.24) is multiplied by a factor of 1000. This is done to study any potential variations in the resulting temperature profile on the cathode that may arise from an enhanced radiative effect. This is discussed further in Section 2.6.2.

### 2.3 Thermophysical Properties

Table 2.1 shows the properties used for tungsten (Forsythe and Worthing 1925; Muller 1955; Lide 1995; Incropera 1996) and the CNT (Gao et al. 1998, 2001; Hone et al. 1999, 2002; Yi et al. 1999; Berber et al. 2000; Kim et al. 2001; Purcell et al. 2002; Fujii et al. 2005) as reported in the literature. The thermophysical properties used for the CNT and shown in Table 2.1 fall in the range of the most probable values reported for multiwalled CNTs.

Finding adequate properties for the CNT is not as straight forward as for tungsten. Several authors have investigated the thermophysical properties of single-wall (Davisson 1920; Hone et al. 1999, 2002) and multi-wall (Yi et al. 1999; Berber et al. 2000) CNTs, with a wide range of variation of the properties depending on the experimental conditions. Yi et al. (1999) performed experiments on MWCNT (obtained by CVD and geometrically similar to the ones in our experiments (Hii et al. 2006)) and determined the specific heat, resistivity and conductivity.



## 2.4 Electron Trajectories

With the electric field distribution determined in every point of the simulation domain [Eq. (2.2)], the electron trajectories are calculated assuming that electrons are emitted from the points in the periphery of the CNT. Two general cases shown in Fig. 2.3 are analyzed: a CNT with a closed, perfectly hemispherical tip; and a CNT with an open ended, flat tip.

Once an electron is launched from its starting position, its trajectory is governed by (Sanchez et al. 2007):

$$\frac{d^2}{dt^2}\mathbf{r} = \frac{e\mathbf{F}}{m_e} + \frac{1}{4\pi\epsilon_0 m_e} \sum_{i,j>i} \frac{e^2}{|\mathbf{r}_{ij}|^2} \quad (2.25)$$

The first term on the right-hand side of Eq. (2.25) corresponds to the electrostatic force applied on a traveling electron due to the presence of the electric field; the second term on the right-hand side corresponds to the Coulomb repulsion forces between moving electrons. Given an ensemble of particles with known location  $\mathbf{r}_i$  and velocity vectors  $\mathbf{v}_i$  at time  $t$ , new positions and velocities at time  $t + \Delta t$  can be found from the expansions (Walker et al. 2004)

$$\mathbf{r}_i(t + \Delta t) = \mathbf{r}_i(t) + \mathbf{v}_i(t)\Delta t + \frac{1}{2}\mathbf{v}'_i(t)\Delta t^2 + \frac{1}{3}\mathbf{v}''_i(t)\Delta t^3 + O(\Delta t^4) \quad (2.26)$$

$$\mathbf{v}_i(t + \Delta t) = \mathbf{v}_i(t) + \mathbf{v}'_i(t)\Delta t + \frac{1}{2}\mathbf{v}''_i(t)\Delta t^2 + O(\Delta t^3) \quad (2.27)$$

The first time derivative of velocity (i.e., acceleration) is found from summation of forces on each particle (Jansen 1988)

$$\mathbf{v}'_i = \frac{e\mathbf{F}}{m} + \frac{C_0}{m} \sum_{j \neq i}^{N_e^-} \frac{\mathbf{r}_{ij}}{|\mathbf{r}_{ij}|^3} \quad (2.28)$$

In Eq. (2.28) the first term is the force on the particle by the applied field, the second term is the space charge between each particle and all its neighbors and  $C_0 = e^2/4\pi\epsilon_0$ .

Because the applied field is assumed constant time derivatives of  $e\mathbf{F}$  are zero and the second order time derivative of velocity is given as

$$\mathbf{v}_i'' = \frac{C_0}{m} \sum_{j \neq i}^{N_e} \left[ \frac{\mathbf{v}_{ij}}{|\mathbf{r}_{ij}|^3} - \frac{(\mathbf{r}_{ij} \cdot \mathbf{v}_{ij}) \mathbf{r}_{ij}}{|\mathbf{r}_{ij}|^5} \right] \quad (2.29)$$

In the simulations presented later a time-step of 2.5 fs is considered in the expansions in Eqs. (2.26) and (2.27).

## 2.5 Finite Element Methods

A multiwalled CNT synthesized by chemical vapor deposition (CVD) attached to an etched tungsten filament is modeled. Figure 2.4 shows an SEM image of the ensemble.

As seen in Fig. 2.4 the CNT is attached to the side of the etched tungsten filament's tip. From a simulation point of view, this creates an anti symmetric model that requires 3D analysis of the geometries. However, the tilt angle of the CNT with respect to the tungsten filament is of approximately  $0.15^\circ$ . In this way, one can assume a model in which the CNT is placed directly on top of the tip of the tungsten filament allowing for a 2D axi-symmetric model shown in Fig. 2.5.

The way that the CNT was attached to the tungsten filament is shown in Fig. 2.5b. Because this represents a revolving geometry, the section shown of the CNT corresponds to a cut of the wall. The number of elements used in Comsol Multiphysics 3.2b was optimized in the following way: the electric field was calculated from Eq. (2.2) for a given number of elements and plotted it on the surface of the CNT until a smooth profile was obtained.

The length, radius, wall thickness and shape of tip of the CNT are varied in this work while the geometry of the tungsten filament remains unchanged. The shape of the tip was considered closed, with a hemispherical cap or open and flat. Also in this work, the effect on the thermal behavior of the CNT for the mentioned parameters are explored. Because

the geometry was continuously changed, the mesh used in the finite element analysis also changes. The discretized mesh is shown below for the closed and open ended tip (Fig. 2.6a and 2.6b respectively):

The adaptive meshing available in Comsol Multiphysics 3.2b allows us to consider more elements close to the apex of the CNT where the curvature is large. However, a problem might arise for the case of the open tip because the edges of the wall might affect the meshing. When the tip of the CNT is perfectly hemispherical fewer elements are required because the curvature of the round tip is smaller when compared to the case of the open tip. Instead of considering straight corners in the simulations where the tip is open, it was assumed that the edges of the wall close to the tip have a very large curvature, 0.8 nm in radius, to avoid discontinuities in the solution of the electro-static equation [Eq. (2.2)] that are caused otherwise. This is also physically accurate because the CNT has a finite number of atoms that result in curved edges. This requires, however, the use of a larger number of elements, especially close to these edges. The electric field distribution on the surface of the CNT was monitored to make sure that any discontinuities caused by potentially deformed mesh elements are avoided. The solution domain of Eq. (2.2) and (2.21) are different. The former is solved outside of the CNT/W geometry to consider only the surrounding vacuum and the latter is solved in the region where the CNT and W filament are defined. The solution methodology is illustrated in Fig. 2.7

The simulations are run in a Windows XP machine, Pentium 4, 3.2 GHz and 4 Gb of ram. For each applied voltage considered, the elapsed time to determine the electric field distribution is approximately 8 s. However, the electron trajectories require a larger time because the integration of the equations of motion is done for various electrons at the same time. An average time of 3 hours is required to determine the trajectories for each applied voltage. The heat transfer calculations required approximately 30 s for each applied voltage.

## 2.6 Field-Emission Simulations and Experimental Validation

The algorithm in Fig. 2.7 was tested based on the experiments carried by Hii et al. (2006). The SEM image in Fig. 2.4 corresponds to the CNT used in their experiments. Their field-emission experiments began with the detection of the surface of the cathode. This was accomplished by measuring the emission current when the separation distance was slowly closed and a small bias voltage produced a sudden current increase under a vacuum base pressure of about  $4 \times 10^{-8}$  mbar ( $3 \times 10^{-8}$  Torr). Once the surface was detected, the voltage was increased to obtain the  $I(V)$  curve for that separation distance. The first separation distance considered was 13.43  $\mu\text{m}$ . The voltage was increased up to a certain point and the 24 measurements of current made. Then, the separation distance was decreased and the experiment was repeated.

### 2.6.1 Electro-static calculations

The electric field distribution on the CNT's tip and the current density determined using Eq. (2.12) are shown in Fig. 2.8 for a gap distance of 13.43  $\mu\text{m}$  for three applied voltages.

A range of input voltages from 65 to 145 V was studied. In Fig. 2.8, only three applied voltages are shown for clarity. The curves in Fig. 2.8 do not correspond to constant electric field (Fig. 2.8a) or constant current density (Fig. 2.8b). They represent the variation of those quantities on the surface of the CNT as a function of applied voltage. The dashed line shown in both figures can be rotated centered on the middle of the wall of the CNT to give the values of the electric field and current density (Figs. 2.8a and 2.8b respectively). The main trend is that when the voltage increases, so does the electric field on the tip. It is noticeable that the maximum electric field for a given voltage is not on the apex of the CNT wall, but rather located in positions outside of the CNT. Also, the electric field exhibits a variation of approximately 50% between its maximum and minimum values found closer to the sides of the wall. This is because the apex of the wall creates a large enhancement of the electric field. The field amplification factor defined as  $\lambda = dF/V$  where  $V$  is the applied voltage,  $d$  is the gap distance and  $F$  is the electric field was calculated. It was found that the field enhancement factor is not

sensitive to the applied voltage and its maximum value of 671.5 correlates well with the experimental data of Hii et al. (2006) for a gap distance of 13.43  $\mu\text{m}$ . The current density in Fig. 2.8b shows even larger variations. The log of the current density is plotted because of differences in the order of magnitude between applied voltages. Comparing Figs. 2.8a and 2.8b, it can be seen that the variations in the electric field, of approximately 50% on the wall produce large variations in the current density. These small values of current density are observed specially in the lower parts of the apex of the wall.

One of the key parameters in estimating the total emission current from the CNT is the knowledge of the emitting area (Hii et al. 2006). In our simulations, the total emission current can be determined by integrating the current density on the surface of the CNT assuming that emission occurs for every point in the surface. Because the current density shows large variations, there are parts of the wall surface that make negligible contributions to the current. Therefore, considering the entire wall surface in the integration should provide a minimum error in the calculation. As the voltage increases, however, it is possible that larger areas on the surface become active electron emission sites and an increase in the emitting area is expected. This effect is shown in Fig. 2.9a.

The emitting area is estimated by calculating the area on the CNT surface for which the local values of the field strength  $F$  exceed 3 V/nm. Only the case with a separation distance of 13.43  $\mu\text{m}$  is considered, however a similar trend is expected for other cases. It was found that as the applied voltage increases so does the emitting area, in an almost linear fashion. As the voltage increases, the field strength on the surface of the CNT also increases creating new sites for electron emission. This increasing area is in contrast with the findings of Hii et al. (2006). In their work an effective emitting area was calculated to fit the Fowler-Nordheim theory [Eq. (2.12)] that was assumed constant with the separation distance and the applied voltage.

Excellent agreement was found between the predicted emission current and their measured values, particularly for the largest separation distance as seen in Fig. 2.9b. However, the calculations also predict a current much lower than what was measured for

the other separation distances considered. This could be attributed to changes in the morphology of the tip due to the process of field-emission. It has been reported that during field-emission the outer carbon rings of the CNT can become detached (Fujieda et al. 2005). This would cause a sudden increase in the sharpness of the tip and thus create additional field enhancement.

Also, the electron trajectories from the tip of the cathode towards the anode were determined following the procedure in (Sanchez et al. 2007). Each point on the tip of the cathode is assumed as a possible electron emission site. From there, we calculate the trajectories of the emitted electrons via integrating Eqs. (2.26) and (2.27). The final position of the emitted electrons on the surface of the anode can then be used to map the current density on the surface. The electron trajectories and the mapped current density on the workpiece are shown in Fig. 2.10 for a gap distance of 13.43  $\mu\text{m}$ .

In Fig. 2.10a the initial position of an electron on CNT's tip (abscissa) with its final position on the workpiece (ordinate) is plotted. For a given separation distance the electron spread on the workpiece is not sensitive to increases in voltage (Sanchez et al. 2007). It was found that the maximum electron spread is approximately three times the gap distance for this particular CNT geometry. Next, the current density on the workpiece was mapped using the final positions of the electrons (Sanchez et al. 2007). The pattern that results on the surface corresponds to a ring with the highest current density at approximately 500 nm away from the center of the CNT. Ring-like patterns due to emission from CNT have been reported in the past (Walker et al. 2004) and result from a large radial component of the electric field near the flat tip of open-ended CNT. This gives the electrons a large radial velocity component that gives a large spread of the emitted electron beam.

The results presented in this section are used in the heat transfer calculations. Because the closest match between experiment and simulation was found with a separation distance of 13.43  $\mu\text{m}$  the results presented below are based only on that case.

### 2.6.2 Heat transfer calculations

With the results of the previous sections, Eq. (2.21) was solved to find the temperature evolution of the CNT as a function of the applied voltage. In Fig. 2.11, the maximum temperature on the CNT is shown as a function of the applied voltage for a separation distance of 13.43  $\mu\text{m}$  (Fig. 2.11a), as well as the main sources of heating of the CNT during the process (Fig. 2.11b). The time required to reach a steady state solution of Eq. (2.21) was approximately 0.01 ms.

The temperature increase of the CNT is almost negligible up to approximately 120 V, as seen in Fig. 2.11a. When the voltage is increased, the temperature rises steeply, almost exponentially. Given that the melting point of a multiwalled CNT can be considered as that of carbon (3773 K), even with an exponential rise in temperature, larger currents could be obtained providing the substrate where the CNT is deposited can withstand the high temperatures (She et al. 2003; Huang et al. 2004). In the work by She et al. (2003) the heat transfer during field-emission from a CNT deposited on top silicon tip was studied. At high emission currents, it was found that the temperature of the CNT increased far beyond the melting point of the silicon tip where it was deposited ( $> 1683$  K), therefore causing a breakdown of the emitter (CNT-silicon tip). In their work the field-emission current was calculated by integrating the full current density equation studied in the work by Murphy and Good (1956) that has no discontinuities for large temperatures. The mechanism responsible for this breakdown was attributed to a “thermal runaway” in which the field-emission current increased uncontrollably with temperature past a certain critical electric field. As the electric field increases, the temperature rise of the CNT is steady and reaches a plateau at a certain value. Slight increases in the electric field beyond this point (less than 0.01%) cause a rapid uncontrollable rise in the temperature. Given that tungsten has a much higher melting point (3680 K) it could probably withstand the higher temperatures attained during this process. The validity of Eq. (2.11) breaks down when the non dimensional parameter  $p$  is greater or equal to unity which mathematically causes the equation to asymptote to infinity at high temperatures. Therefore, the simulations were only carried up to  $p \sim 0.5$ , where 0.7 is the highest recommended value (Fransen 1999).

The main heat sources on the CNT are the Joule heating [Eq. (2.22)] and the Nottingham effect [Eq. (2.20)]. The former is always positive because it is a function of the emission current and the resistance. The latter, however, can have negative values depending on the temperature: if it is lower than the inversion temperature  $T_I$  [Eq. (2.19)] then the Nottingham effect heats the emitter. If it is higher, it cools it. To determine the overall Nottingham effect Eq. (2.20) was integrated on the surface of the CNT. The Joule heating was determined by integrating Eq. (2.22) over the volume of the probe (CNT attached to tungsten filament). Both effects are compared in Fig. 2.11b as a function of the applied voltage. Our calculations show that the main source of heating of the cathode is the Joule heating. For small voltages, it seems that the Nottingham effect and the Joule effect tend to be comparable. As the voltage increases the Nottingham effect is negligible in comparison to the Joule heating. This is in contrast to the findings of Gratzke and Simon (1995) in which the Joule heating was found to be negligible. In their work, the volume considered in the calculation of the Joule heating was that of the CNT only. However, in more realistic conditions, the cathode where the CNT is located also contributes to the Joule heating because the field-emission current flows through it. There is a noticeable decrease in the Nottingham effect close to 140 V indicating the possibility that some points on the tip have a temperature above the inversion temperature. The inversion temperature is shown in Fig. 2.12.

The behavior of the Nottingham effect for high voltages (Fig. 2.11b) is explained in Fig. 2.12 via the magnitude of the inversion temperature. At some points on the tip of the CNT the temperature rise exceeds the inversion temperature and the Nottingham effect switches from heating to cooling. The maximum value of the latter is approximately  $18 \times 10^9 \text{ W/m}^2$  and remains positive for a larger area on the tip. Points that are below a radius of 28.8 nm do not contribute significantly to the Nottingham effect because for these points the magnitude of the current density and electric fields are low and affect Eq. (2.20) in the same way. The overall Nottingham effect is of heating of the cathode, even though the negative values on the integral decrease its magnitude when compared to the Joule heating.



Finally, in Fig. 2.13a a comparison was made between the temperature dependent field-emission current [integral of Eq. (2.11)] with the zero-Kelvin approximation [integral of Eq. (2.12)] and the experimental data of Hii et al. (2006) for a separation distance of 13.43  $\mu\text{m}$ . It was found that the temperature dependent emission current is almost the same as the temperature independent emission current for most of the voltage range considered. This means that the effect of temperature is negligible when it comes to calculating the emission current, especially for lower voltages. Additionally, the effect of neglecting near field thermal radiation effects on the transient temperature increase of the cathode (Fig. 2.13b) was investigated. Two cases are considered based on an arbitrary “field enhancement factor” that multiplies the total radiative flux. In the first case, it was assumed that the field enhancement factor is unity (neglecting all potential near field effects). In the second case, a value 1000 was used. For an applied voltage of 130 V, it was found an error of less than 1% in neglecting all near field thermal radiation effects. Therefore, it can be concluded that using the classical radiative transfer formulation is adequate for the calculations presented above.

## 2.7 Geometrical effects

The numerical methods developed in the previous section are now extended to study the effects on the electro-statics, heat transfer and electron trajectories that variations in the geometry of the CNT have on calculated quantities. Since it is well known that the methods to grow CNTs differ in their production yield and the geometrical characteristics of the CNTs they produce (Iijima 1991; Joseyacaman et al. 1993; Guo et al. 1995), it is compelling to study the effect of CNTs’ geometry in their field-emission characteristics and thermal behavior.

### 2.7.1 Effects on electro-statics

The effect of different geometries of the CNT on the electro-static solution of the problem was considered first. The field amplification factor [Eq. (2.18)] is used for this purpose as it encompasses several parameters at once. The results are shown in Fig. 2.14 for a CNT with an open tip and a CNT with a closed tip.

The most noticeable feature in Fig. 2.14 is the difference between the amplification factor for the CNT with an open (Fig. 2.14a) and one where the CNT has a closed tip (Fig. 2.14b). Since the curvature of the edges in the case of the CNT with an open tip is much larger than when the tip is closed, and perfectly hemispherical, the electric field is amplified the most. The main trends are that for longer CNTs and larger the gap distances, the field strength is amplified the most. It was found that this is more noticeable as the radius of the CNT increases. For a CNT of 30 nm in radius the field amplification factor is approximately 12.8 for a gap distance of 500 nm. A similar calculation done for a CNT of 50 nm in radius and the same gap distance gives a factor of 8.35 which means that as the radius of the CNT increases and the gap distance decreases the condition of two parallel plates ( $\lambda = 1$ ) can be achieved (Sanchez and Mengüç 2008a). For very large gap distances the field amplification factor is comparable to the field enhancement factor. The latter can reach values of up to 3000 for a combination of large gap distance (greater than 500  $\mu\text{m}$ ) and small CNT radius (1.4 nm) (Walker et al. 2004). For smaller gap distances, regardless of the length, the curvature of the tip is flatter as seen from the perspective of the anode. Therefore, the condition of two parallel plates is achieved for very small gap distances as exhibited by the lower magnitudes of the amplification factor in Fig. 2.14. Even though matching a given experimental data set might require specific knowledge of the CNT geometry, the trends that were observed are consistent the experimental observations using tungsten tips (Olson and Panitz 1998) and with CNTs grown on silicon tips (Minh et al. 2003)

Using Eq. (2.11) one can calculate the total field-emission current after integrating along the surface for both cases (Fig. 2.15).

The effect of the shape of the tip is shown in Fig. 2.15 where the  $I(V)$  characteristics of a closed-ended CNT against an open-ended CNT keeping everything else constant (radius, height, and gap distance) are compared. The main conclusion being that at small gap distances, a lower voltage is required to achieve a given emission current. An even smaller voltage is required if the CNT is open ended. It is clear that a voltage that is almost three times smaller is required to achieve field-emission when the CNT is open-

ended. An even smaller voltage would be required if the radius of the open-ended CNT was smaller, such as the case of the CNT used by Hii et al. (2006).

### 2.7.2 Electron Trajectories and Deposition Profiles

One can now study the effect that the geometrical characteristics considered above have on the profile of the emitted electrons. The methodology described in Section 2.4 is followed. Assuming that electrons are emitted from points in tip of the CNT (see Fig. 2.3) Newton's equations are integrated with a time-step of 2.5 fs. The results of this analysis are shown in Fig. 2.16. When a given parameter was varied, all the others were considered constant.

The results shown in Fig. 2.16 were done for a wide range of geometrical characteristics of the CNT, as well as potential experimental conditions such as the applied voltage and gap distance. The most noticeable effect on the final electron positions on the workpiece is realized for variations of the gap distance. It is interesting to see, that as the gap distance decreases, the electron spread on the surface of the workpiece does the same. This is essentially because the electrons do not have enough time to travel further outwards and rather hit closer positions to the center of the workpiece. A lower spread of the electrons on the surface of the workpiece, also means that the concentration of electrons that are deposited inside the material and could be used for the heating process, increases. However, a smaller gap distance also means that in order to achieve a given emission current one needs to apply a smaller voltage which also translates in electrons with a smaller kinetic energy. In the next Chapter, the methodology is followed to see how some of these geometrical variations affect the electron deposition profiles inside the workpiece. First, the effects that these geometrical parameters have on the heat transfer problem on the CNT during field-emission are studied in detail.

### 2.7.3 Heat Transfer

The heat transfer problem during field-emission from the finite element solution of Eq. (2.21) can now be considered. Five different situations were analyzed in which one geometrical parameter was changed while leaving the others the same. As in the case of

the electro-static problem in the previous sections, the length, radius, wall thickness, shape of the CNT tip and its gap distance from the workpiece have been changed and their effects on the final temperature on the CNT compared. First, the results for a combination of geometrical parameters whose variation did not affect the final temperature are shown in Fig. 2.17.

The results in Fig. 2.17a are shown in the form of temperature vs. emission current plots, where the emission current corresponds to the integral of the Eq. (2.11) on the surface of the CNT. All the results correspond to the maximum temperature obtained on the CNT after the steady state solution was obtained localized very close to the tip of the CNT. It was observed small temperature gradients on the CNT which had an almost uniform temperature distribution. Larger temperature gradients were observed on the contact between the CNT and the tungsten. The emission current actually encompasses the effects of the amplification of the electric field and the geometry of the CNT therefore it can be considered as a normalized parameter made of various changing contributions. Even though in the previous section the complicated behavior of the electro-static solutions as a function of the length, gap distance and shape of the tip, was shown in the form of the field amplification factor, it seems that these parameters have no effect on the overall temperature increase on the CNT.

It was observed in the simulations that the predominant contribution to the heat transfer is the Joule heating term [Eq. (2.22)], which was up to five orders of magnitude larger than the Nottingham effect [Eq. (2.20)] (see Fig. 2.17b). This is because of the larger volume of the tungsten filament to which the CNT was attached. When the length of the CNT increased, or the shape of its tip changed, its volume was altered. However, this small change in volume had a negligible effect on the overall Joule heating term. Also, even though a smaller voltage may produce the same emission current for a given geometry, say the same current is obtained with 600 V for a CNT with a closed tip and 200 V for one with an open ended tip, the current, not the voltage, is the key parameter that defines the Joule heating term. As shown in the previous section, the field amplification factor increases when the gap distance is large, meaning that a smaller

voltage is required to obtain the same emission current keeping all other geometrical parameters of the CNT constant. Again, this does not affect the Joule heating term that depends only on the emission current. Further, for all cases the temperature rise of the CNT is negligible up to emission currents of  $\sim 1 \mu\text{A}$ . The shape of the plots in Fig. 2.17 exhibits an almost exponential rise on the temperature for high emission currents due to the same mechanism described in Section 2.6.2.

It was found that two geometrical parameters have an effect on the temperature increase on the CNT (Fig. 2.18). The effect of the CNT radius shows that for small radii, smaller currents produce high temperatures; the same effect was observed when the wall thickness was small. As seen in Fig. 2.17b, the main contribution to the heat transfer is the Joule heating; however, for the cases depicted in Fig. 2.18 the volume change of the CNT on the overall Joule heating is negligible. For instance, one can compare the change in the CNT volume when its length is increased from  $2 \mu\text{m}$  to  $4 \mu\text{m}$ , setting its radius to  $50 \text{ nm}$  and its wall thickness to  $10 \text{ nm}$ . This corresponds to increasing (or decreasing) the total volume of the CNT by 50%. The percentage change on the volume of the CNT after varying the wall thickness from  $10 \text{ nm}$  to  $5 \text{ nm}$ , keeping the length and radius constant, is approximately 50%. Both cases produce approximately the same variation on the total volume of the CNT, however their effect is markedly different, namely as shown in the temperature vs. emission current results as seen in Figs. 2.17 and 2.18. The reason for this change in temperature is due to the variations in the contact region between the CNT and the tungsten filament. As this region decreases, the energy that is dissipated to the tungsten becomes restricted due to the smaller contact area. More energy is left on the CNT that serves to heat it up. However, even though the plots show marked variations, the differences in the emission current are not necessarily large (not in orders of magnitude), and maybe subjected to errors in thermophysical properties or the variations in physical dimensions of CNT. Because in real experiments the CNT is physically attached to the side of the tungsten filament, the effect shown in Fig. 2.18 might only be a computational issue for this particular configuration since the actual way in which the contact between the CNT and the tungsten filament is done is far more complicated than the assumption that was made in the model (see Fig. 2.5b). Nevertheless, in many cases

the CNTs are deposited on top of a flat surface that serves as the cathode for which a thermal behavior such as the one depicted in Fig. 2.18 might be observed.

The effect of the variation of the thermophysical properties of the CNT in the results presented in this section should also be mentioned. It was found that using a larger electric resistivity produces a larger temperature rise for a lower current. For instance, considering  $\rho_{elec} \sim 8 \times 10^{-6} \Omega\text{m}$  after (Dai et al. 1996) the steady state solution of Eq. (2.21) gives a temperature of 1177 K when a voltage of 500 V is applied on a CNT with a closed tip, 50 nm radius, 10 nm wall thickness, 2  $\mu\text{m}$  height and a gap distance of 10  $\mu\text{m}$ . In contrast, using the value shown in Table 2.1, after (Purcell et al. 2002), gives a steady state temperature of approximately 442 K for the same geometrical considerations as in the previous case. In both cases, the calculated field-emission current is 10  $\mu\text{A}$ . The latter is subject to the magnitude of the work function which was considered as 4.7 eV after (Gao et al. 2001). However, values used in the literature for the calculation of the field-emission current range from 4.5 eV (Walker et al. 2004) to 5.1 eV (Purcell et al. 2002) which give currents of 26  $\mu\text{A}$  and 1.3  $\mu\text{A}$  respectively. In the first case, the temperature rise is fast and unbounded, whereas in the second, a steady state temperature of 296 K is achieved. This means that one could model the heat transfer problem considering larger magnitudes of the work function and the resistivity of the CNT and find steady state solutions for larger applied voltages based on published experimental data. It was observed that the variations in the thermal conductivity of the CNT had negligible effects on the overall heat transfer predictions (Yang 2005). Additional numerical errors may be found in the contact between CNT and the tungsten filament, for which no special considerations were given here.

## 2.8 Comments

In this Chapter the numerical methodology was developed to study the problem of electron field-emission from CNTs in depth. The effect that realistic experimental settings have on the overall process were analyzed, and what the limitations are as far as maximum voltage that can be applied and maximum current that can be achieved. The

knowledge of these parameters is important because it affects the potential of using the CNTs for machining applications.

Table 2.1  
Thermophysical properties

Property	Tungsten (W)	CNT
Density $\rho$ ( $Kg/m^3$ )	19250 (Incropera 1996)	1330 (Gao et al. 1998)
Emissivity $\varepsilon$	$-0.0434+1.8624E-4T-1.954E-8T^2$ (Forsythe and Worthing 1925)	1 (Huang et al. 2004)
Resistivity $\rho_{elec}$ ( $\Omega m$ )	$48E-9(1+4.8297E-3(T-273)+1.663E-6(T-273)^2)$ (Lide 1995)	1.7E-6 (Purcell et al. 2002)
Specific Heat $C_p$ ( $J/kg K$ )	$4E-14T^5 - 3E-10T^4 + 7E-07T^3 - 0.0008T^2 + 0.4501T + 53.299$ (Incropera 1996)	$0.0004 T^2 + 1.4429T - 10.238$ (Yi et al. 1999)
Conductivity $k$ ( $W/mK$ )	$1E-11T^4 - 8E-08T^3 + 0.0002T^2 - 0.2568T + 230.88$ (Incropera 1996)	3000 (Kim et al. 2001)
Work function (eV)	4.8 (Muller 1955)	4.7 (Gao et al. 2001)



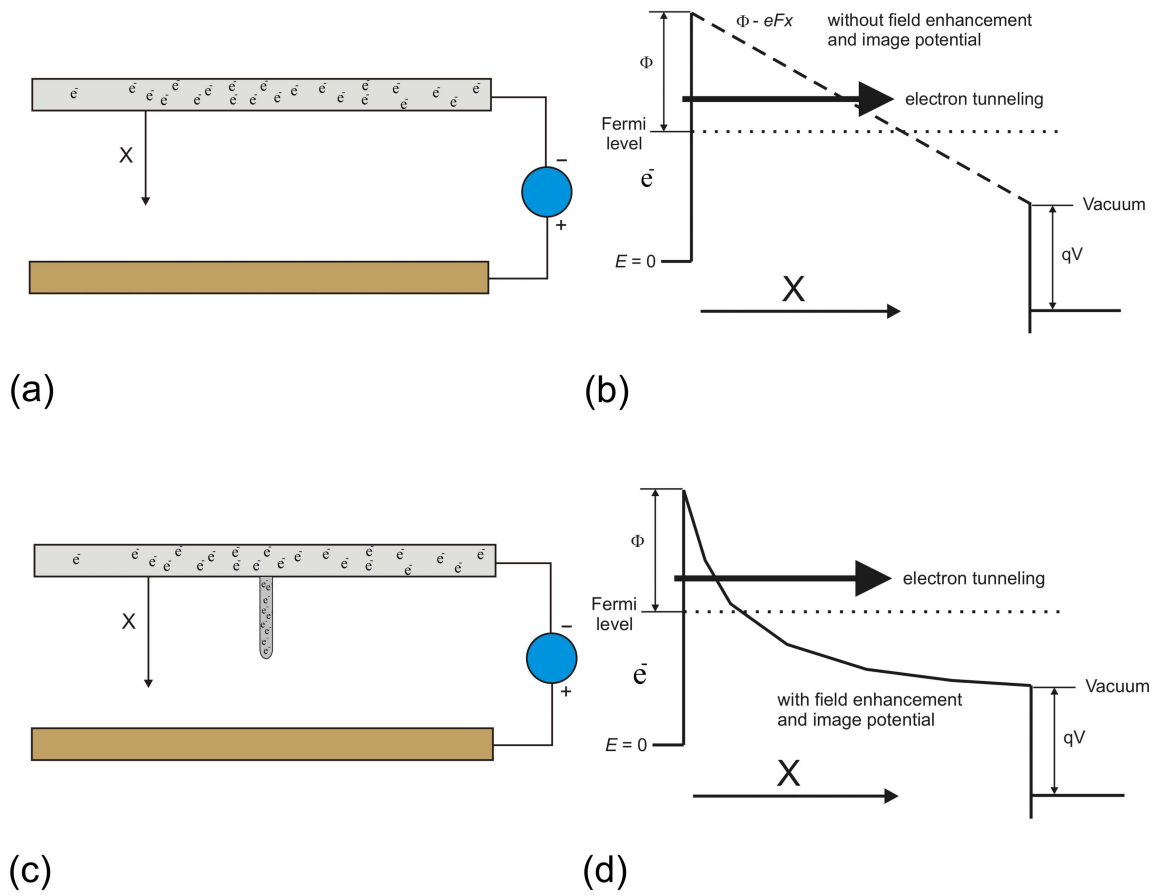


Figure 2.1 a) Two flat plates separated by a finite distance in the vacuum; b) energy diagram for a); c) CNT placed on top of a flat plate and separated by a finite distance from second plate; d) energy diagram for c).

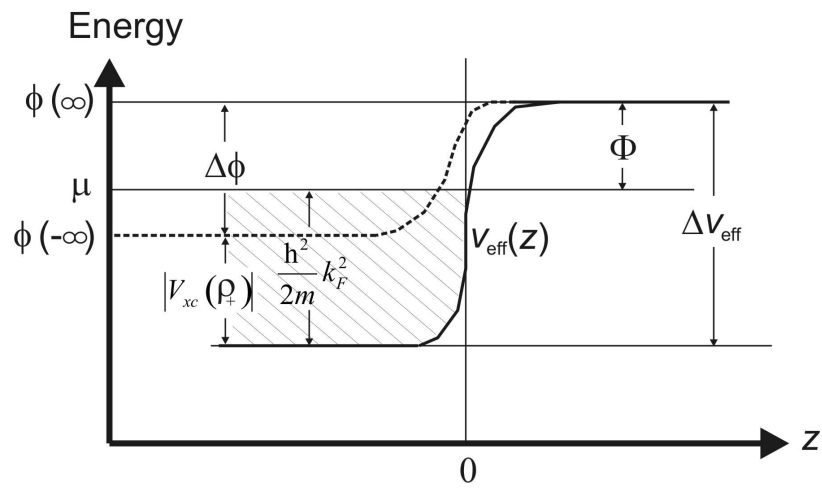


Figure 2.2 Potential energy diagram for defining the work function (Tsukada 1983)

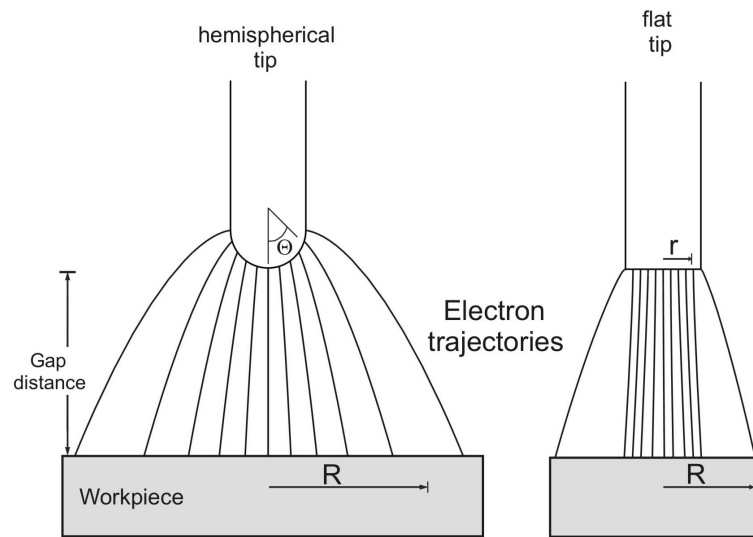


Figure 2.3 Side-view schematic of the electron stream and radial coordinate at the surface of the workpiece (Sanchez et al. 2007)

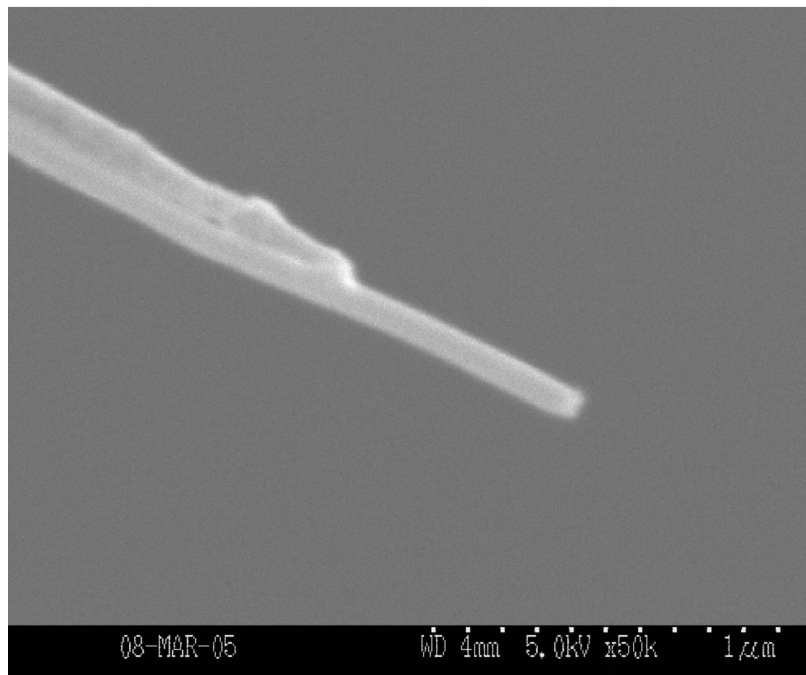
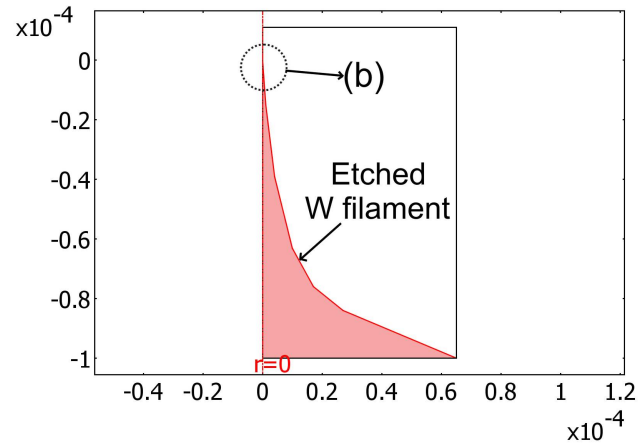
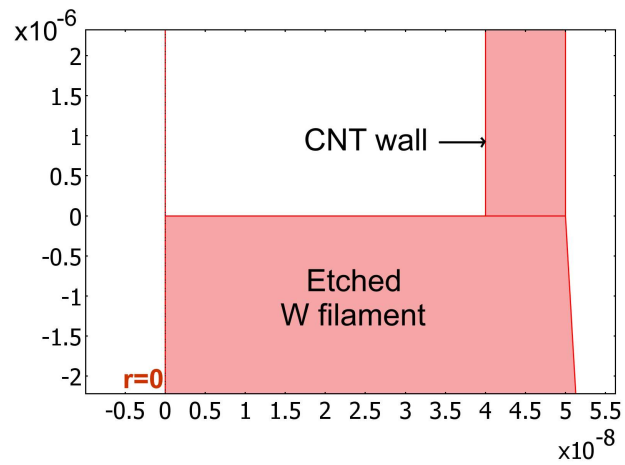


Figure 2.4 SEM image of CNT attached to an etched tungsten probe. The CNT has dimensions of  $\sim 60$  nm in diameter and  $2.1 \mu\text{m}$  in length. The protruding length is  $\sim 600$  nm.



(a)



(b)

Figure 2.5 a) Geometry of the CNT attached to the tungsten filament. b) attachment point. The model is axi symmetric with the revolving axis depicted as  $r = 0$ . The dimensions are in meters.

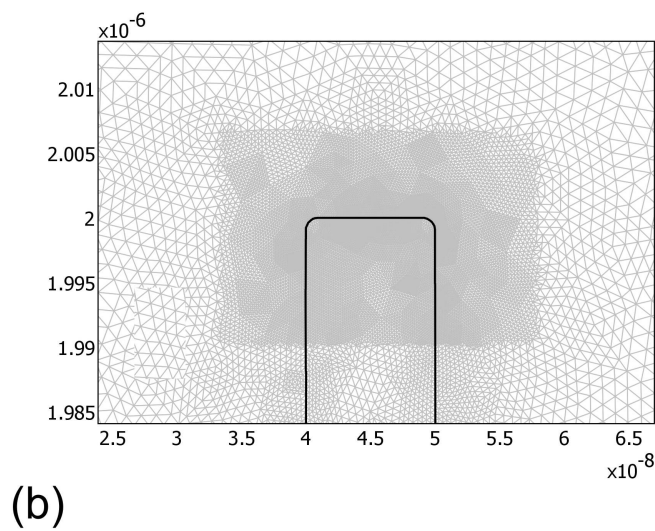
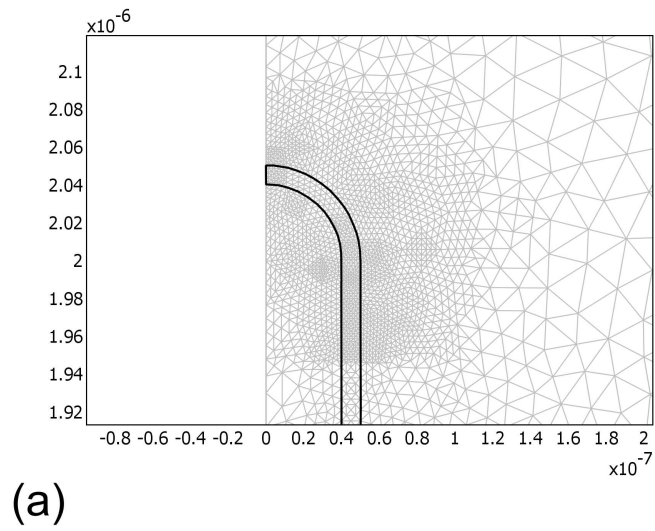


Figure 2.6 Meshing used in the simulations for a CNT with a) closed tip; b) open tip, 10 nm wall thickness.

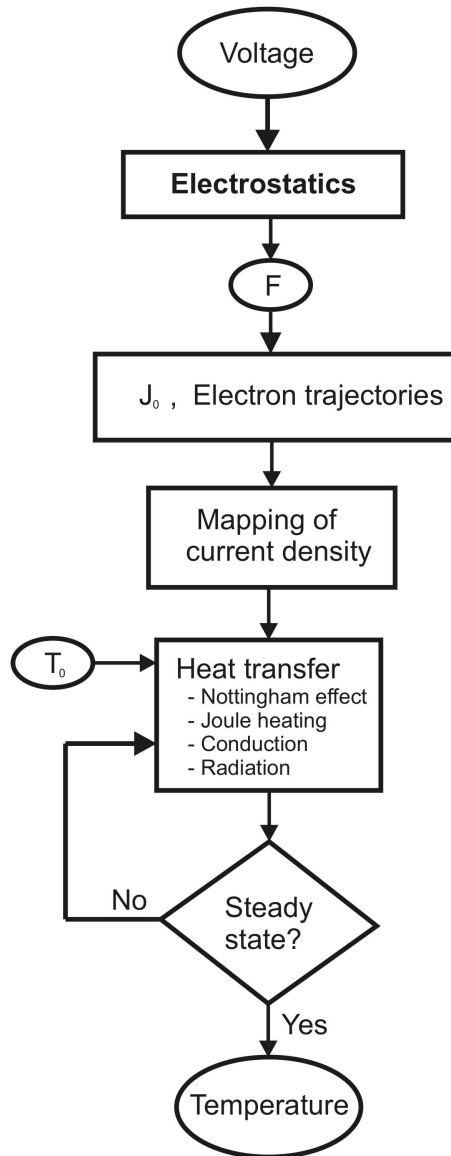


Figure 2.7 Solution methodology of the finite element problem discussed in Section 2.5

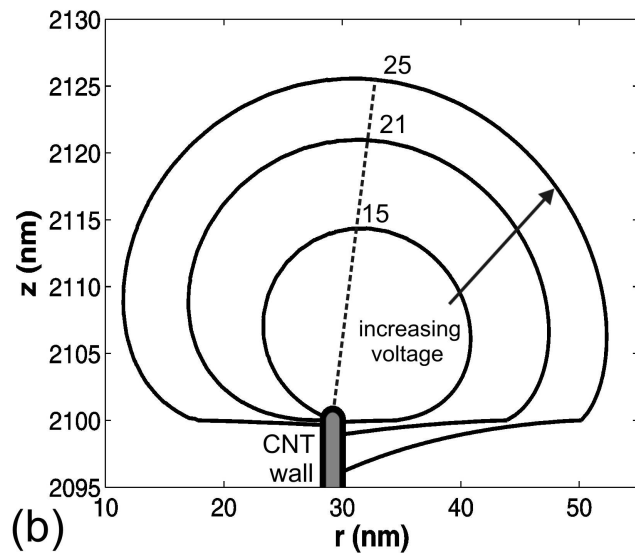
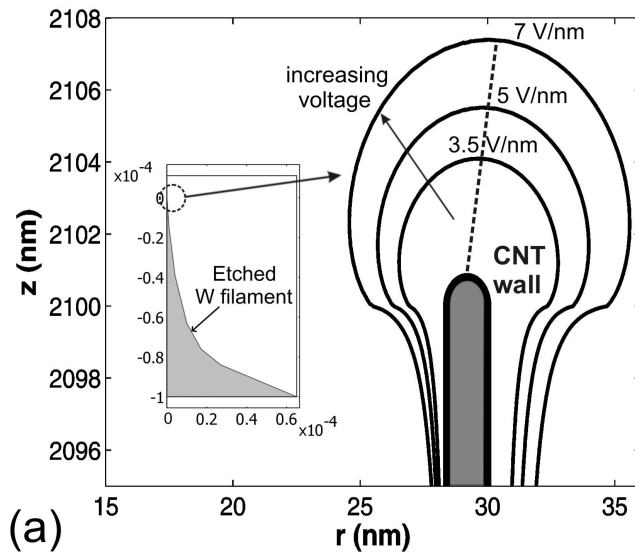


Figure 2.8 a) Electric field distribution on the CNT's tip (inset is in meters). b) Log of the current density on the CNT's tip. The gap distance is  $13.43 \mu\text{m}$  and the plots correspond to 70, 100 and 140 V. Figures a) and b) are enlarged from the inset in a). The axis of symmetry is at  $r = 0$ . The dashed line can be used for reference as the values indicated for each intersection correspond to the magnitudes of the normal electric field or current density at that point. The dashed line can be rotated on the center of the wall of the CNT to give the values of the electric field or current density at the intersection points. The values shown correspond to the values of the electric field and current density at that particular intersection (Sanchez et al. 2008a).



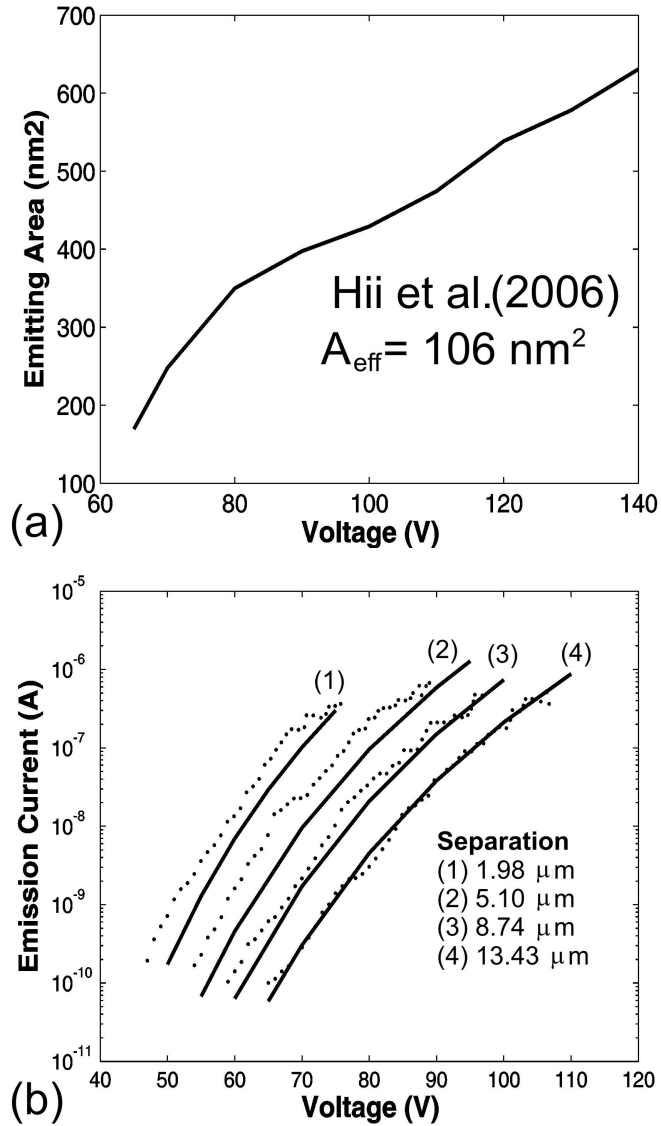


Figure 2.9 a) Emitting area as a function of the applied voltage for a separation distance of 13.43  $\mu\text{m}$ . b) Emission current vs. voltage. The points correspond to the experimental data by Hii et al. (2006).

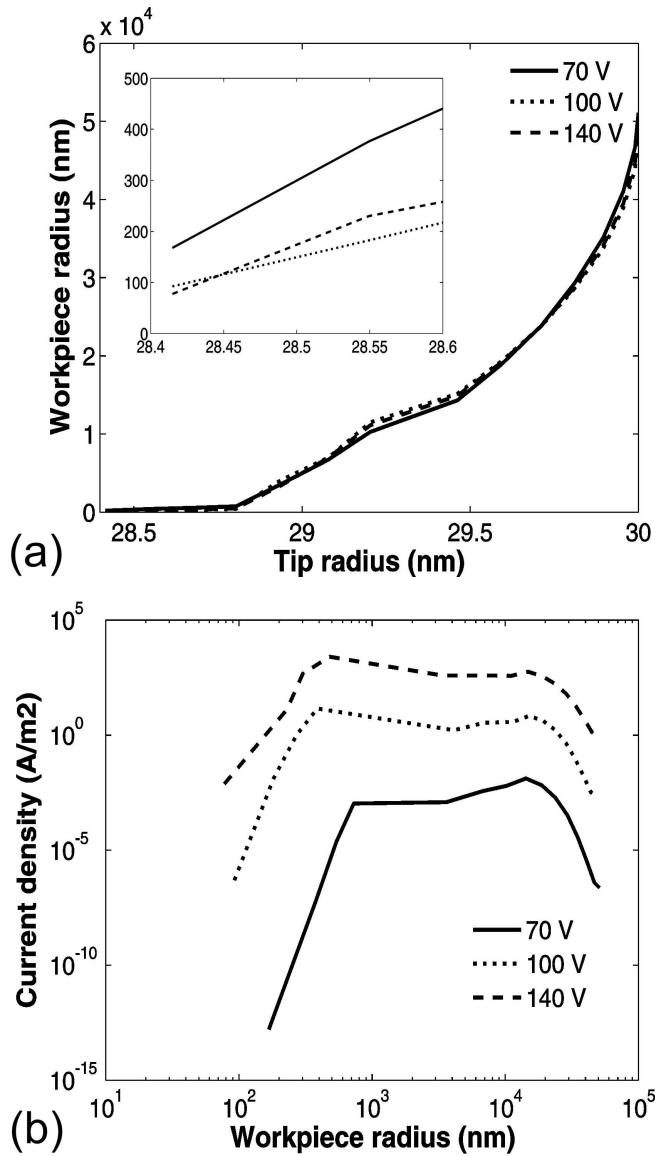


Figure 2.10 a) Electrons that are emitted from a radial location on the tip (abscissa) impact at a radial location on the workpiece (ordinate). The inset has the same dimensions. b) Current density on the workpiece mapped following (Sanchez et al. 2007). The axis of symmetry is at  $r = 0$ . The separation distance is  $13.43 \mu\text{m}$ .

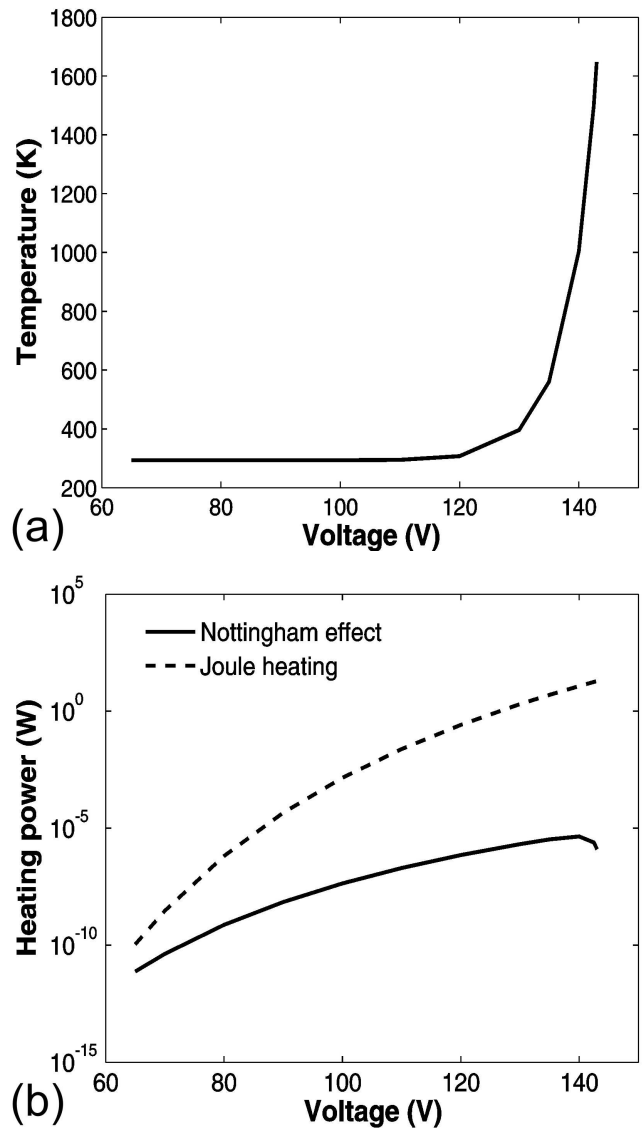


Figure 2.11 a) Maximum temperature vs. applied voltage. b) Comparison between the Nottingham effect and the Joule heating.

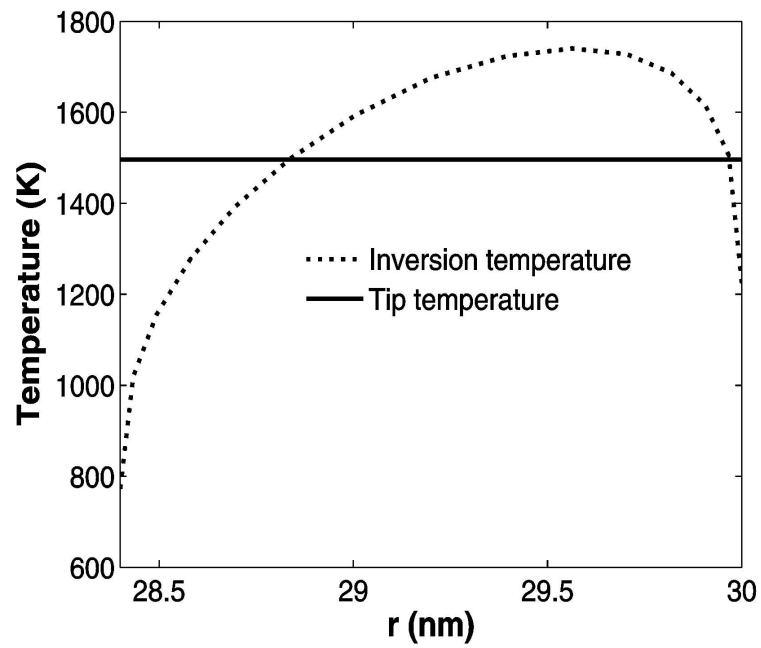


Figure 2.12 Comparison between the temperature on the tip and the inversion temperature, Eq. (2.19).

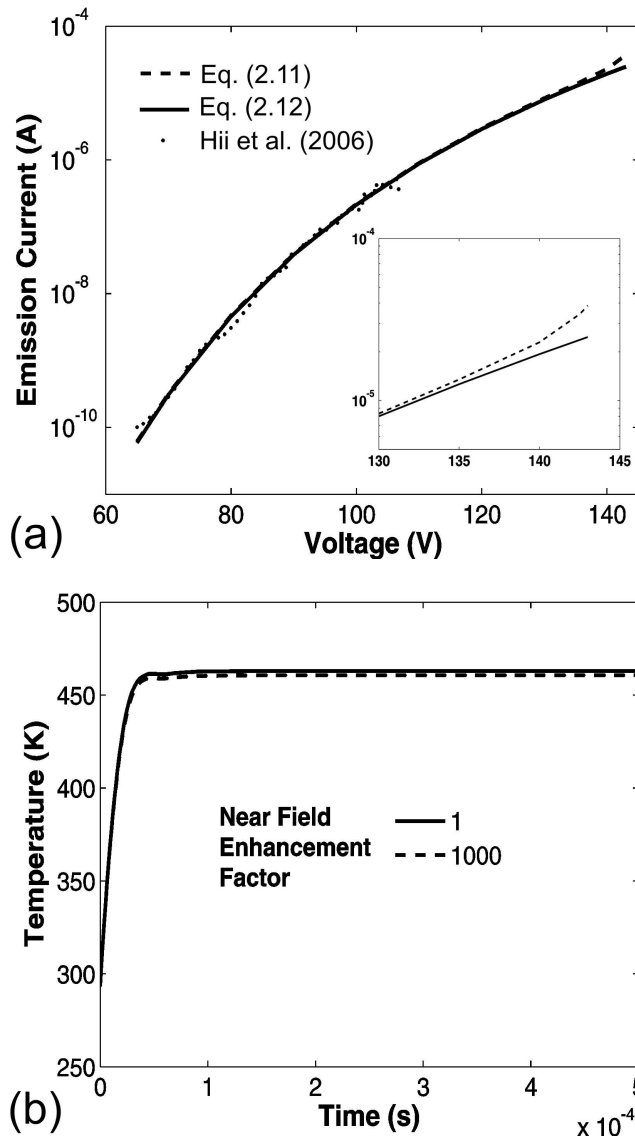


Figure 2.13 a) Comparison between the total emission current from integrating Eqs. (2.11) and (2.12) with the experimental data of Hii et al. (2006). The inset has the same dimensions. b) Near field thermal radiation effects compared based on a constant factor. The applied voltage is 130 V.

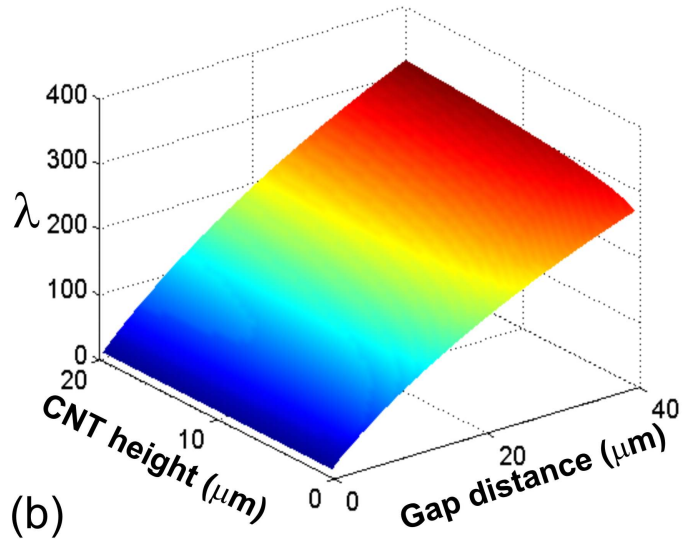
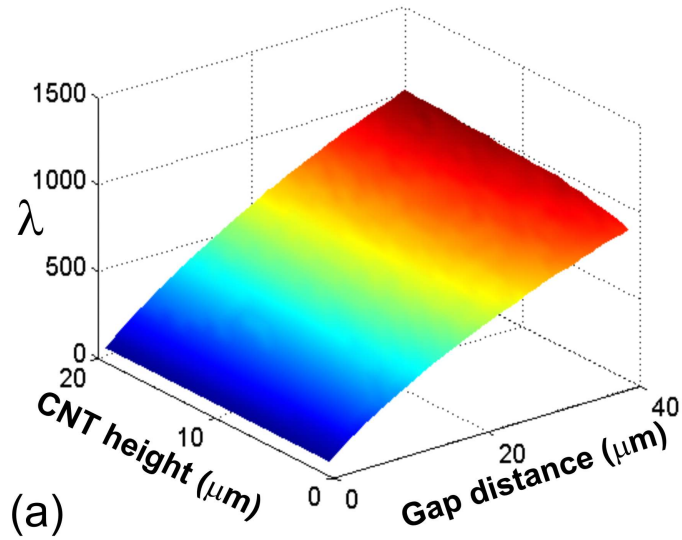


Figure 2.14 Field enhancement factor contour plots for a CNT to a tungsten filament to show the effect of length of the CNT and gap distance from the anode. The radius of the CNT is 30 nm; the minimum gap distance and length considered were 500 nm. a) open tip with a wall thickness of 5 nm; b) closed tip.

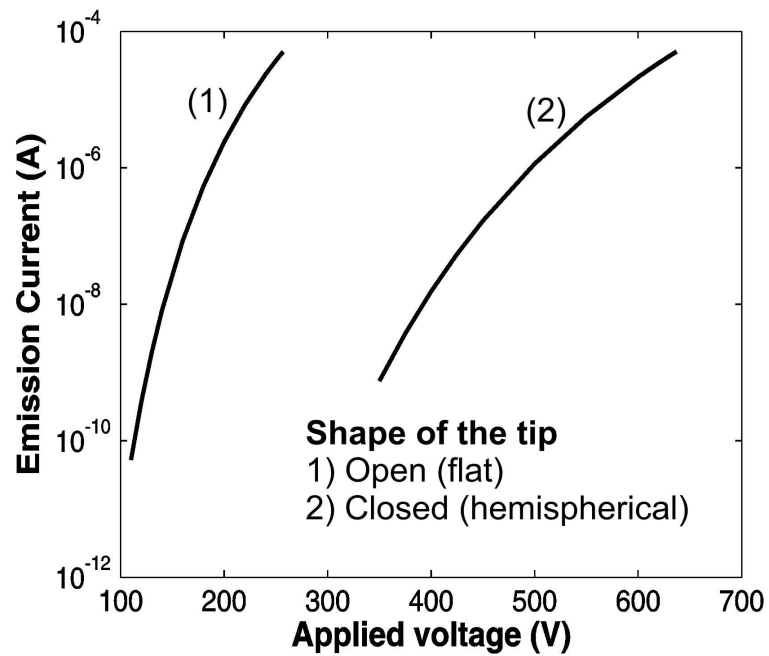


Figure 2.15 Comparison between the emission characteristics [ $I(V)$  plot] between an open ended and closed CNT with length of  $2 \mu\text{m}$ , radius of  $50 \text{ nm}$  and gap distance of  $18 \mu\text{m}$ .

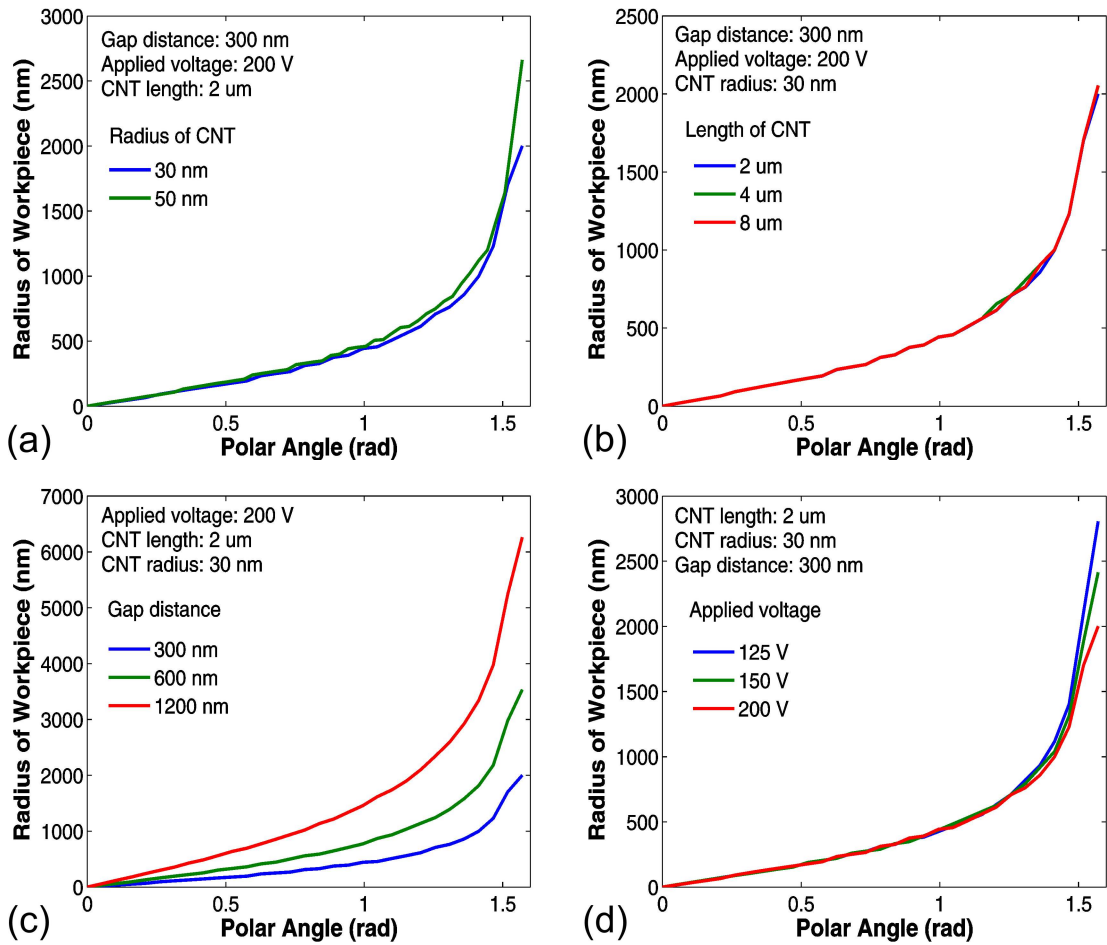


Figure 2.16 Radial profile of electrons on the workpiece as a function of electron emission from a particular polar angle on the tip (see Fig. 2.3). a) effect of radius of the CNT; b) effect of length of the CNT; c) effect of the gap distance; d) effect of the applied voltage. In every case, all other geometrical parameters remained constant.



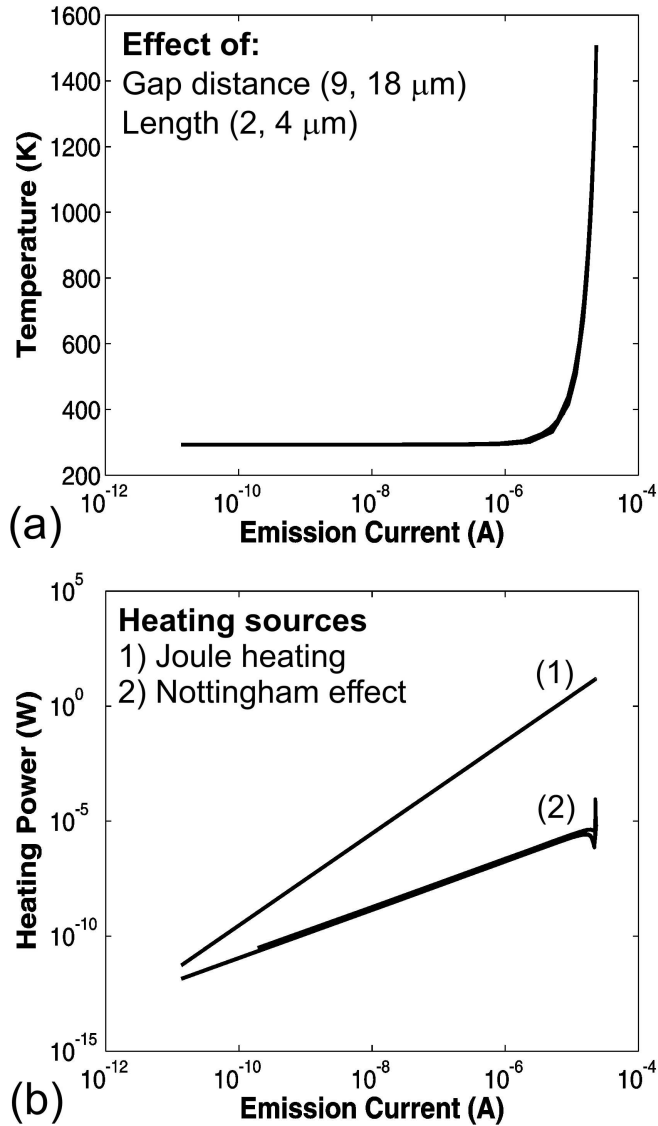


Figure 2.17 a) Maximum temperature distribution vs. emission current for different geometries of the CNT. b) Comparison between the heating sources acting on the CNT. The Joule heating term was integrated over the entire volume of the CNT and the tungsten filament, whereas the Nottingham effect was integrated over the surface of the CNT. For all cases the CNT had a radius of 50 nm and wall thickness of 10 nm. In b) all the cases shown in a) are considered. Different shapes of the tip do not have any significant effect on these results.

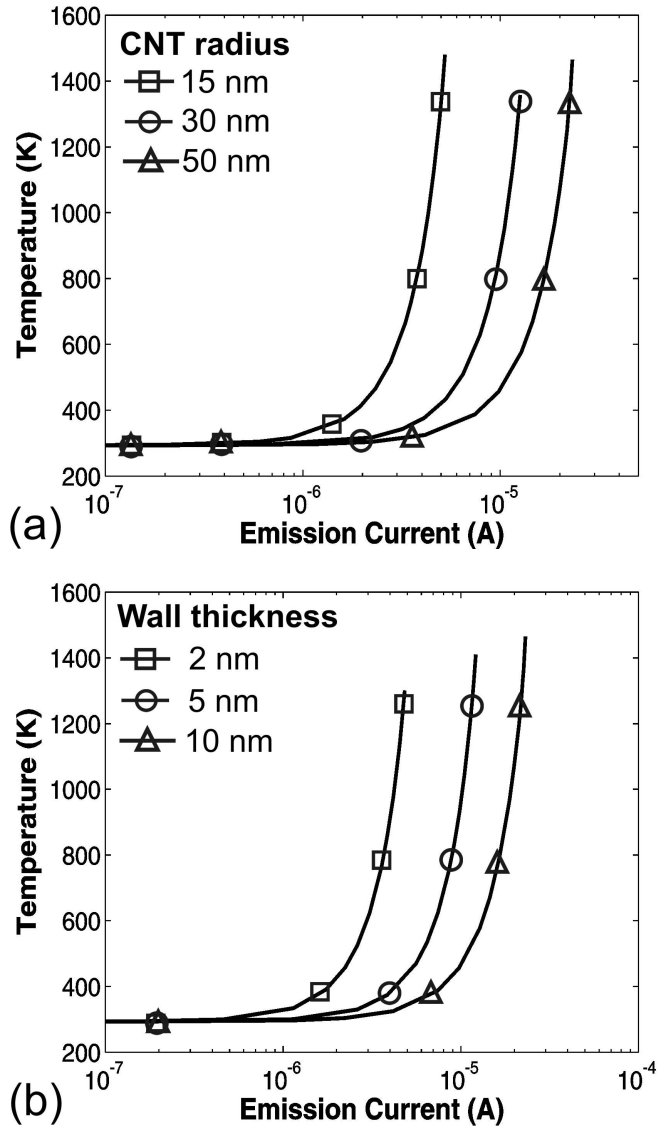


Figure 2.18 Maximum temperature distribution vs. emission current for different geometries of the CNT: a) effect of CNT radius; b) effect of wall thickness. In a) the wall thickness remained constant at 10 nm and in b) the outer radius of the CNT was fixed at 50 nm.

CHAPTER 3  
ELECTRON ENERGY DEPOSITION IN METALS  
AND HEAT TRANSFER MODELS

In the previous Chapter, the background of electron field-emission from CNTs was established. The results suggest that there is a limitation in the maximum voltage that can be applied to a single CNT based on heating during the process. It was also determined that the geometry of the CNT and the gap distance between it and the workpiece play key roles in setting this voltage. The task is now to determine how these parameters affect the deposition of the emitted electrons inside the workpiece.

### 3.1 Electron beam propagation

The propagation of an electron beam inside a scattering and absorbing medium obeys the BTE, which describes the evolution of a particle distribution (say,  $f$ ) over time and space as particles undergo a number of scattering events. The general form of the BTE is written as (Ziman 1960, 1964; Ashcroft and Mermin 1976; Ferry and Goodnick 1997)

$$\frac{\partial f(\vec{r}, \vec{k}, t)}{\partial t} + \vec{v} \cdot \nabla f(\vec{r}, \vec{k}, t) = \left( \frac{\partial f}{\partial t} \right)_{col} \quad (3.1)$$

where the collision term on the right-hand side is expressed as

$$\left( \frac{\partial f}{\partial t} \right)_{col} = \sum_{\vec{r}', \vec{k}'} W(\vec{k}', \vec{k}) f(\vec{r}', \vec{k}', t) - \sum_{\vec{k}'} W(\vec{k}, \vec{k}') f(\vec{r}, \vec{k}, t) \quad (3.2)$$

At the right hand side of Eq. (3.2),  $W$  denotes the scattering rate, the first summation is the rate of change of  $f$  due to the in-scattering of particles while the second is the rate of change of  $f$  caused by the out-scattering of particles. Note that the particle distribution  $f$  in general depends on its location in space  $\vec{r}$ , its wave vector  $\vec{k}$ , and time  $t$ . In its general form, the BTE is difficult to solve owing to the seven independent variables and its integro-differential form. In order to simplify the equation, the BTE is transformed into

the intensity form where the particle distribution is conveniently removed. The intensity form of the BTE for governing electron-beam propagation (or the electron-beam transport equation (ETE)) is given as (Ashcroft and Mermin 1976; Ding and Shimizu 1996):

$$\frac{\partial I_e}{\partial t} + \vec{v}_e \cdot \nabla I_e = - \left[ \sigma_e^{inel} (E) + \sigma_e^{el} (E) \right] I_e + \frac{\sigma_e^{el} (E)}{4\pi} \times \sum_{E'} \int_{\Omega'} \Phi_e (E', \theta', \phi'; E, \theta, \phi) I'_e (E, \theta', \phi', t) \quad (3.3)$$

To solve this equation, one can use a MCM called discrete inelastic scattering (DIS) method (Ashcroft and Mermin 1976; Ding and Shimizu 1996; Wong and Mengüç 2004). As the name implies, the DIS method treats the inelastic scatterings as point scattering events; hence, an inelastic scattering mean free path is employed. Ding and Shimizu (1996), and later Wong and Mengüç (2004) outlined this method in a very orderly fashion, and the procedures given in (Wong and Mengüç 2004) are followed closely here.

The method developed by Wong and Mengüç (2008) was validated by calculating the back-scattering yield of electrons as a function of the electron-beam energy. The results were compared with the experimental data compiled by Joy (2001). The agreement with experimental data is excellent as seen in Fig. 3.1, especially in the small energy range (0 to 5 keV).

### 3.2 Electron deposition profiles as a function of CNT geometry

The formulation described in the previous section is used as the input of the MCM of Wong and Mengüç (2008) the electron profiles determined as a function of the geometry of the CNT. Two cases were modeled: the first one using the beam profile of the perfectly hemispherical tip; the second, using the profile for a flat tip. Figure 3.2 shows the electron distributions obtained for 300 V and 50 V, although the other cases shown in Fig. 2.16 can be easily determined.

Figures 3.2a and 3.2c show the electron-energy distributions for the case where the tip is perfectly hemispherical, while Figs. 3.2b and 3.2d depict the electron distributions for the case in which the tip of the probe is flat. The reason for the appearance of a ring-like pattern is due to the fact that the electrons emitted from the CNT when its tip is open originate only from the edges. Also, for the cases where the electron beam forms a ring on the surface of the workpiece the width of the ring is usually thinner than the width of the distribution obtained when considering the perfectly hemispherical tip. This means that even though the electron beam is spread over a larger radius on the surface, the narrow ring formed tends to be more focused locally than the distribution obtained from the perfectly hemispherical tip.

In general, results presented in Fig. 3.2 reveal that the penetration of the electron beam inside the workpiece depends on the applied voltage, being larger for the highest simulated voltage since the initial kinetic energies of electrons are higher. This is commonly observed in our electron-beam simulations (Wong and Mengüç 2004, 2008; Wong et al. 2004). However, higher penetration depth implies deeper spreading of electron energy inside the material along the axial direction, as evident in Fig. 3.2a (300V) where the deposition magnitudes are two to three order smaller than those in Fig. 3.2c (50V). The similar trend can be observed between Figs. 3.2b and 3.2d.

### 3.3 The Two-Temperature Model

The transport of energy carriers can be treated, under a quasi-classical particle framework, by the Boltzmann transport equation (BTE) (Liboff 1998),

$$\frac{\partial f}{\partial t} = -\frac{d\mathbf{r}}{dt} \cdot \nabla_{\mathbf{r}} f - \frac{d\mathbf{p}}{dt} \cdot \nabla_{\mathbf{p}} f + \left( \frac{\partial f}{\partial t} \right)_s \quad (3.5)$$

It expresses the total rate of change of the particle distribution  $f(\mathbf{r}, \mathbf{p}, t)$  as the result of diffusion, external field driving, and scattering, respectively. The scattering term [last term of the right hand side of Eq. (3.5)] describes the change of particle numbers at an energy state due to collisions. Three basic assumptions are made to solve the BTE: (1) the relaxation time approximation; (2) the steady state-approximation, and (3) the near-

equilibrium approximation (Bube 1974) although later Qiu and Tien (1993) showed that only the last approximation is valid for femtosecond laser heating. In the relaxation time approximation it is assumed that the scattering term can be expressed as a function of a relaxation time  $\tau$  that is considered independent of the type of perturbation (for example, electric field, thermal gradient, etc.)

$$\left(\frac{\partial f}{\partial t}\right)_s = -\frac{f - f_0}{\tau} = -\frac{g}{\tau} \quad (3.6)$$

where  $f_0$  corresponds to the equilibrium distribution of the energy carriers, the Fermi-Dirac distribution for electrons and Bose-Einstein distribution for phonons. In Eq. (3.6) the function  $g = f - f_0$  corresponds to a small deviation from equilibrium, and corresponds to the near-equilibrium approximation described above (Chen 2005). Finally, in the steady state approximation, it is assumed that the transient effects on the particle distribution  $f$  are negligible.

Interactions between external sources of heating such as the photon- and electron-beams and the workpiece are well described through the BTE. The problem can be made tractable when three assumptions are made: (1) Electron-phonon interaction is the dominant scattering process for electrons; (2) the conduction of heat by phonons is negligible; and (3) phonons and electrons have temperatures  $T_l$  and  $T_e$  respectively<sup>2</sup>. The processes of laser- heating or electron-beam nanomachining involve the heating of the electron gas inside the workpiece causing the electron energy to elevate substantially when compared to the lattice energy. At the continuum level, the time evolution of the lattice and electron temperatures,  $T_l$  and  $T_e$ , can be described within the so-called two-temperature model (TTM) (Kaganov 1957). The TTM is derived by taking the moments of the BTE for both electrons and phonons (Wong and Mengüç 2008). It neglects the kinetic energy changes of electrons, and assumes interactions between electrons and phonons through a coupling constant  $G$ . It is modeled with two coupled nonlinear differential equations,

---

<sup>2</sup> It is assumed that the “temperature” of a particular point in the workpiece comprised of a finite number of atoms corresponds to the phonon temperature, and here it is also referred to as the lattice temperature.

$$C_e(T_e) \frac{\partial T_e}{\partial t} = \nabla [k_e(T_e) \nabla T_e] - G(T_e - T_l) + S \quad (3.7)$$

$$C_l(T_l) \frac{\partial T_l}{\partial t} = \nabla [k_l(T_l) \nabla T_l] + G(T_e - T_l) \quad (3.8)$$

where  $C$  and  $k$  are the heat capacities and thermal conductivities of electrons and lattice denoted by subscripts  $e$  and  $l$ . The first term on the right-hand-side of Eq. (3.8) responsible for the phonon heat conduction is typically negligible as compared to the electron heat conduction in metals and is often omitted. The source term  $S$  is used to describe the local energy deposition per unit volume and unit time during the energy-beam/lattice interactions for either electron- or laser-beams.

### 3.3.1 Electronic Properties

In metals, the energy transport by phonons is neglected, since the heat is carried mainly by free electrons (Makinson 1938). At very low temperatures, the electron heat capacity  $C_e$  is proportional to  $T_e$ ,  $C_e(T_e) = \gamma T_e$  (Ziman 1964); however, it has been common practice in recent years to use this expression for a wide temperature range as long as  $T_e$  is much smaller than the Fermi temperature, which is of the order of  $10^4$  K (Qiu and Tien 1992; Anisimov and Rethfeld 1997; Caffrey et al. 2005). This is, in general, a valid approximation because at higher temperatures the electronic component to the heat capacity is negligible in comparison to the lattice component (Ziman 1964). In the past, the latter has been assumed constant to its value at 273 K for the various materials studied even when phase change occurs (Qiu and Tien 1992; Hakkinen and Landman 1993; Anisimov and Rethfeld 1997; Schafer et al. 2002; Caffrey et al. 2005).

The electronic thermal conductivity  $k_e$  can be obtained from

$$k_e = \frac{L(T_e) T_e}{\rho_e} \quad (3.9)$$

where the  $\rho_e$  is the electric resistivity and  $L(T_e)$  is the Lorentz function which also depends on  $T_e$  (Williams 1969). In the Wiedemann-Franz law, which states that for metals at moderate temperatures (roughly for  $T_l > 0.48 T_D$ , where  $T_D$  is the Debye

temperature) the ratio of the thermal conductivity to the electrical conductivity is proportional to the temperature and the constant of proportionality is independent of the particular metal, the Lorentz function is usually assumed as a constant  $L(T_e) = L_0 = (k_B/e)\pi^2/3$  (Ziman 1964). However, deviations of  $L(T_e)$  from  $L_0$  occur due to inelastic electron-phonon and electron-electron scattering in metals as a function of the temperature (Williams 1969). Expressions for  $k_e$  have been suggested in the past that depend on the relation between the ratio  $\mathcal{G}_e = T_e/T_F$  where  $T_F$  is the Fermi temperature. An adequate expression for  $k_e$  valid for low electron temperatures ( $\mathcal{G}_e \ll 1$ ) is given as (Anisimov and Rethfeld 1997; Caffrey et al. 2005)

$$k_e = k_0 \frac{T_e}{T_l} \quad (3.10)$$

where  $k_0$  is the equilibrium thermal conductivity measured at room temperature. This expression is appropriate for metals such as nickel or aluminum that have  $T_F = 136000$  K (Ashcroft and Mermin 1976). As  $\mathcal{G}_e \sim 1$ , another expression was proposed that is applicable to copper or gold (Anisimov and Rethfeld 1997)

$$k_e = C \mathcal{G}_e \frac{(\mathcal{G}_e^2 + 0.16)^{5/4} (\mathcal{G}_e^2 + 0.44)}{(\mathcal{G}_e^2 + 0.092)^{1/2} (\mathcal{G}_e^2 + b\mathcal{G}_l)} \quad (3.11)$$

where,  $\mathcal{G}_l = T_l/T_F$ . In the low temperature limit,  $\mathcal{G}_e \ll 1$ , Eq. (3.11) is reduced to Eq. (3.10) For high electron temperatures,  $\mathcal{G}_e \gg 1$ , Eq. (3.11) reduces to the dependence characteristic for a low-density plasma,  $k_e \sim T_e^{5/2}$ .

The electron-phonon coupling constant,  $G$ , is the key parameter governing the rate of the electron-phonon thermal relaxation process and can be calculated from free electron theory (Kaganov 1957; Allen 1987). Within the limits of Wiedemann-Franz's law Qui and Tien (1992) expressed  $G$  as



$$G = \frac{\pi^4 (n_e v_s k_B)^2}{18k_e} \quad (3.12)$$

where  $k_B$  ( $1.381 \times 10^{-23}$  J/K) is Boltzmann's constant,  $n_e$  is the number density of the electron gas and  $v_s$  is the speed of sound. Measurements using the pump-probe technique (Hohlfeld et al. 2000) and approximations based on Eq. (3.12) (Qiu and Tien 1992) have been performed in the past for a wide variety of metals. Table 3.1 summarizes the different electronic properties available in the literature and considered in this work.

### 3.3.2 Heating of an Au workpiece with a single CNT

One can now study the heating effects on an Au workpiece when a CNT with a given geometry, applied voltage and gap distance emits electrons due to field-emission that hit the workpiece. A potential experimental case was considered with a CNT with a 30 nm radius, perfectly hemispherical tip, 2  $\mu\text{m}$  height, 200 V of applied voltage and a gap distance of 300 nm. For this particular case, the total emission current is 7.9  $\mu\text{A}$  and the maximum temperature rise of the CNT is 630 K. The electron spread on the surface of the workpiece and the electron deposition profile inside of it are shown in Fig. 3.3.

The results in Fig. 3.3 indicate that the radial spread of the electron beam that reaches the surface of the workpiece is several orders of magnitude larger than the maximum penetration depth inside of the workpiece. Numerically, this means that one could study the problem based on a one-dimensional (1D) formulation of the TTM [Eqs. (3.7) and (3.8)]. The following implicit discretization can be used for such a case.

$$A_1 (T_{e,i+1,j,k}^{t+1} + T_{e,i-1,j,k}^{t+1}) - A_2 T_{e,i,j,k}^{t+1} - A_3 = 0 \quad (3.13)$$

with

$$A_1 = \frac{k_e}{\Delta x^2} \quad A_2 = 2A_1 + G + \frac{C_e}{\Delta t} \quad (3.14)$$

$$A_3 = GT_{e,i,j,k}^t + \frac{C_e}{\Delta t} T_{l,i,j,k} + S \quad (3.15)$$

In the formulation shown above the electronic thermal conductivity,  $k_e$ , and the electronic heat capacity  $C_e$  are evaluated at the electronic temperature in a given timestep,  $T_{e,ijk}^t$ . The deposited electrons carry a heating power of  $S = 1.58 \times 10^{-3}$  W, where  $S$  is the source term in Eq. (3.7). Adiabatic boundary conditions are considered when solving the TTM implemented by using a ghost node method (Wong et al. 2004). The use of Eq. (3.13) results in a triple banded or tridiagonal matrix that can be solved using a standard numerical scheme (Kincaid 2002). Since the lattice thermal conduction in Eq. (3.8) is negligible in comparison to the electronic thermal conduction in Au, after the electron temperature is determined in a given timestep, one can determine the lattice temperature using

$$T_{l,i}^{t+1} = \frac{C_l T_{l,i}^{t+1} / \Delta t + GT_{e,i}^{t+1}}{G + C_l / \Delta t} \quad (3.16)$$

The initial temperature of the workpiece was set at 300 K. The results for this particular case indicate that the temperature rise of the workpiece is negligible after a simulation time of 1 ns with a timestep of 1 fs. Here the temperature profiles of the workpiece are not shown given that the observed temperature of both the electronic system and the lattice remains constant throughout the simulation. A previous numerical work by Fisher et al. (2003) shows that a maximum temperature rise of 10 °C is observed on a metallic workpiece after it is heated by field-emission electrons from a CNT. In their work, transient effects were neglected and the solution corresponds to steady state. In a more recent experimental work by Westover et al. (2007) the temperature rise of a metallic workpiece was measured while it was heated by the electrons emitted by a CNT. Their results also suggest a negligible temperature rise. All these results seem to indicate that the electron field-emission from a single CNT might not provide sufficient energy to achieve heating and material removal.

### 3.4 Electron Field-Emission from multiple CNTs

Nanomachining is a thermal process in which electrons with high energy penetrate inside a metallic workpiece, transfer their energy to the lattice and induce melting and material removal of a nanometer-sized spot. However, our modeling efforts discussed in the previous sections suggest that this might not be possible with a single CNT. Thus, the potential of using multiple CNTs in an array as depicted in Fig. 3.4 is analyzed.

Electron field-emission from arrays of CNTs have been numerically studied in the past (Wang et al. 2005) to investigate the effect of the axial separation distance between the CNTs on their electro-static characteristics. It was found that a critical intra-tubular distance exists which equals the height of the CNTs assuming that they are all of the same height. A more recent experimental work investigated the field enhancement characteristics of a mat of CNTs which had variable lengths (Park et al. 2006). When the intra-tubular distance is below the critical length the electro-static field enhancements on the tips of the CNTs decrease, and so does the total emission current of the array. This means, for instance, that if one was able to measure the current of one CNT while the intra-tubular distance is greater than the critical length, then one would measure the same current as if that CNT was the only one in the flat plate. When the intra-tubular distance is below the critical length, then the measured current would be much lower than the previous value.

Even though the floating sphere model has been used in the past to account for the electric field enhancement around sharp tips (Walker et al. 2004; Wang et al. 2005), a finite element methodology has been proven to be as reliable (Edgcombe 2001; Sanchez et al. 2007, 2008; Sanchez and Mengüç 2008a). Here, the finite element method developed by Sanchez et al. (2008) was used to determine the electro-static field around the CNTs. Then, assuming that electrons are emitted from the tips of the CNTs, Newton's equations of motion were solved for the electrons considering electro-static and Coulomb repulsion forces to determine the trajectories of the electrons from the CNTs towards the surface (Sanchez et al. 2007). The final positions of the electrons are used to map the current density from the tip of the CNTs on the surface. Finally, the Monte Carlo method

(MCM) developed by Wong and Mengüç (2004) was used to determine the electron energy density on the workpiece based on the multiple electron deposition profiles.

In order to reduce the number of finite elements required for the numerical solution of the problem, only five CNTs were considered in the array. One CNT was assumed to be in the center and the other four circling it within a certain intra-tubular distance from the center which was varied. In a real experiment, one could expect to have thousands of CNTs in the array, so here one is interested in the trends of the numerical results more than in their actual magnitude. CNTs with radii of 30 nm, perfectly round hemispherical caps and 2  $\mu\text{m}$  of height were considered. The gap distance, measured from the tip of the CNTs along their axis towards the surface was set as 300 nm and the applied voltage at 200 V.

Two general scenarios were explored: in the first, only one CNT was modeled and the procedure described above was followed; in the second, three different situations are considered as a function of the intra-tubular distance. Figure 3.5 shows the final positions of the electrons that reach the workpiece, that are emitted from the tip of the CNT from a given polar angle (Sanchez et al. 2007).

As seen in Fig. 3.5 a focusing effect is evident when the intra-tubular distance is less than the height of the CNT. This is mainly due to the Coulomb repulsion forces. As an electron emitted from the CNT in the center of the array travels through the vacuum, it only interacts with its neighbors up to a certain distance, beyond which the Coulomb forces are negligible as they decay following  $1/r^2$ , where  $r$  is the distance between traveling electrons (see Eq. (2.25)). As it was shown in previous studies, electrons emitted from a CNT tend to have a relatively large spread that is a function of the geometrical parameters of the CNT itself, as well as the gap distance between the tip and the surface (Walker et al. 2004; Sanchez et al. 2007). For the gap distance of 300 nm considered in the results presented in Fig. 3.5, it can be seen that the maximum spread is almost five times the gap distance. However, as the force field produced by the electrons emitted from surrounding CNTs becomes important, the electrons emitted from the CNT

in the center are slightly deflected off course towards the center of the surface and thus a small focusing effect is observed.

Figure 3.6a shows the field amplification factor on the CNT in the center normalized to its maximum value. It is defined as  $\gamma = dF/V$  (Hii et al. 2006) where  $\gamma_{\infty} = 7.34$  and was calculated for a single CNT emitter,  $d$  is the gap distance,  $V$  is the applied voltage, and  $F$  is the electric field. The calculations show, as expected, that as the intra-tubular distance decreases below the critical length (equal to the height of the CNT) the amplification of the electric field decreases given that as the CNTs get closer they start behaving as a flat plate. A more detailed study of the effect of the intra-tubular distance on the total emission current and field enhancement of an array of CNTs was given by Wang et al. (2005). Here, the same trend as reported in their work was observed. A decrease in the enhancement of the electric field also means that the total emission current of the array decreases (Fig. 3.6b). As the electric field on the tip of the CNT decreases, fewer sites on the surface of the CNT tip emit electrons as the probability that an electron tunnels out of the potential barrier is lowered (Sanchez et al. 2007, 2008). This results in a lower field-emission current. Note that even though our simulations were only done for five CNTs, it is expected that the same trend is observable in an array with thousands of CNTs (Wang et al. 2005; Park et al. 2006). Since nanomachining requires a large heating power to induce pronounced temperature gradients the number of CNTs that can be packed into an emitter island has to be balanced with respect to their expected total emission current, as a lower current would be obtained for CNTs that are very close together.

With the final positions of the electrons on the surface known, the methodology given in (Sanchez et al. 2007) was followed to map the current density from the CNT tip to the surface and determine a cumulative probability distribution function (CPDF) required for the MCM. The positions that the electrons reached on the surface of the workpiece are then the initial positions from which they propagate into the material. Note that in MC method developed by Wong and Mengüç (2004) the electrons are launched into the medium one at a time and the second electron does not interact with the first electron that was launched and so on. This means, that one could numerically launch multiple beams

and solve the EBTE to determine their propagation into the medium and thus the final electron energy density in a particular point in the material is just the addition of all the electrons in the medium.

The results in Fig. 3.7 show the electron energy density calculated from MCM simulations as a function of the depth into the material. All the cases considered in Fig. 3.5 are also shown in Fig. 3.7. For the applied voltage of 200 V, the maximum penetration depth was approximately 10 nm, which is the last point where the electron energy density was greater than zero. What this results show is that the final electron deposition inside the material is virtually independent of the number of CNTs that are used in the array. The main advantage of using an array of CNTs is that even though their final electron deposition is the same as for one CNT, the heating power available is proportional to the number of CNTs in the array. Therefore, the amount of energy available depends on the number of CNTs that can be packed into a substrate. The problem is now on finding the most appropriate focusing methods that can be applied to such a system. The use of such a mechanism could potentially allow the patterning of nanometer-sized features on a metallic surface using electron-beams.

Because now the amount of heating power available to the electrons is virtually a function of the number of CNTs in the array the simulation of the heating process using Eqs. (3.7) and (3.8) is not going to be attempted. These equations would require additional assumptions regarding thermal expansion and material properties that might become questionable in a continuum model. Thus, the modeling of such a system is left to the discussions presented in the following Chapters.

### 3.5 Comments

In this Chapter the heating effects on an Au workpiece due to the electron field-emission from a single CNT were determined with realistic experimental conditions. It was found that though the heating effect might be negligible as corroborated by previous experiments. However, the use of multiple CNTs acting at the same time might provide an alternative approach to nanomachining.

Table 3.1  
Material constants used for TTM calculations.

Metal	$G$ ( $10^{17}$ W/m <sup>3</sup> K)	$\gamma$ (J/m <sup>3</sup> K <sup>2</sup> )	$k_0$ (W/mK)	$C$ (W/mK)	$b$	$T_F$ (K)
Au	0.21 <sup>a</sup>	71 <sup>a</sup>	-	353 <sup>b</sup>	0.16 <sup>b</sup>	64000 <sup>c</sup>
Cu	1 <sup>a</sup>	96.6 <sup>a</sup>	377 <sup>b</sup>	14.9 <sup>c</sup>	-	81200 <sup>d</sup>
Ni	3.6 <sup>d</sup>	1065 <sup>d</sup>	91 <sup>d</sup>	-	-	136000 <sup>c</sup>

<sup>a</sup> (Hohlfeld et al. 2000); <sup>b</sup> (Anisimov and Rethfeld 1997); <sup>c</sup> (Ashcroft and Mermin 1976);  
<sup>d</sup> (Gray 1972); <sup>e</sup> (Schafer et al. 2002); <sup>f</sup> (Yamashita et al. 2006)

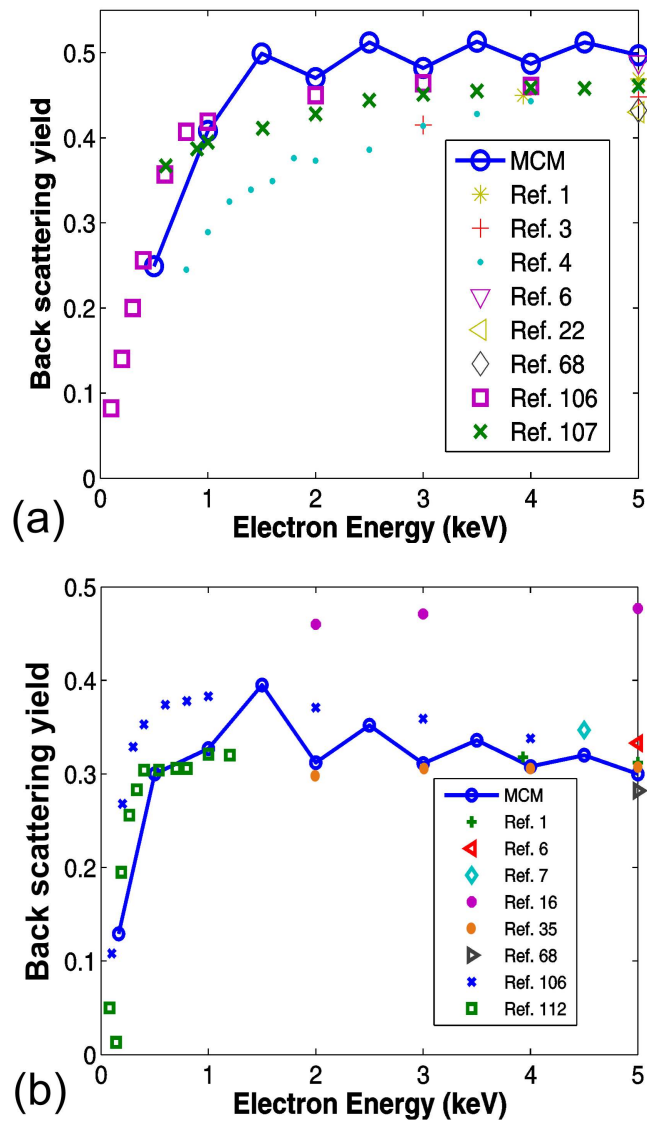


Figure 3.1 Back scattering electron yield as a function of the electron-beam energy for a) Au and b) Ni. The indicated references can be found in the compilation by Joy (2001). The line is just a guide to the eye.



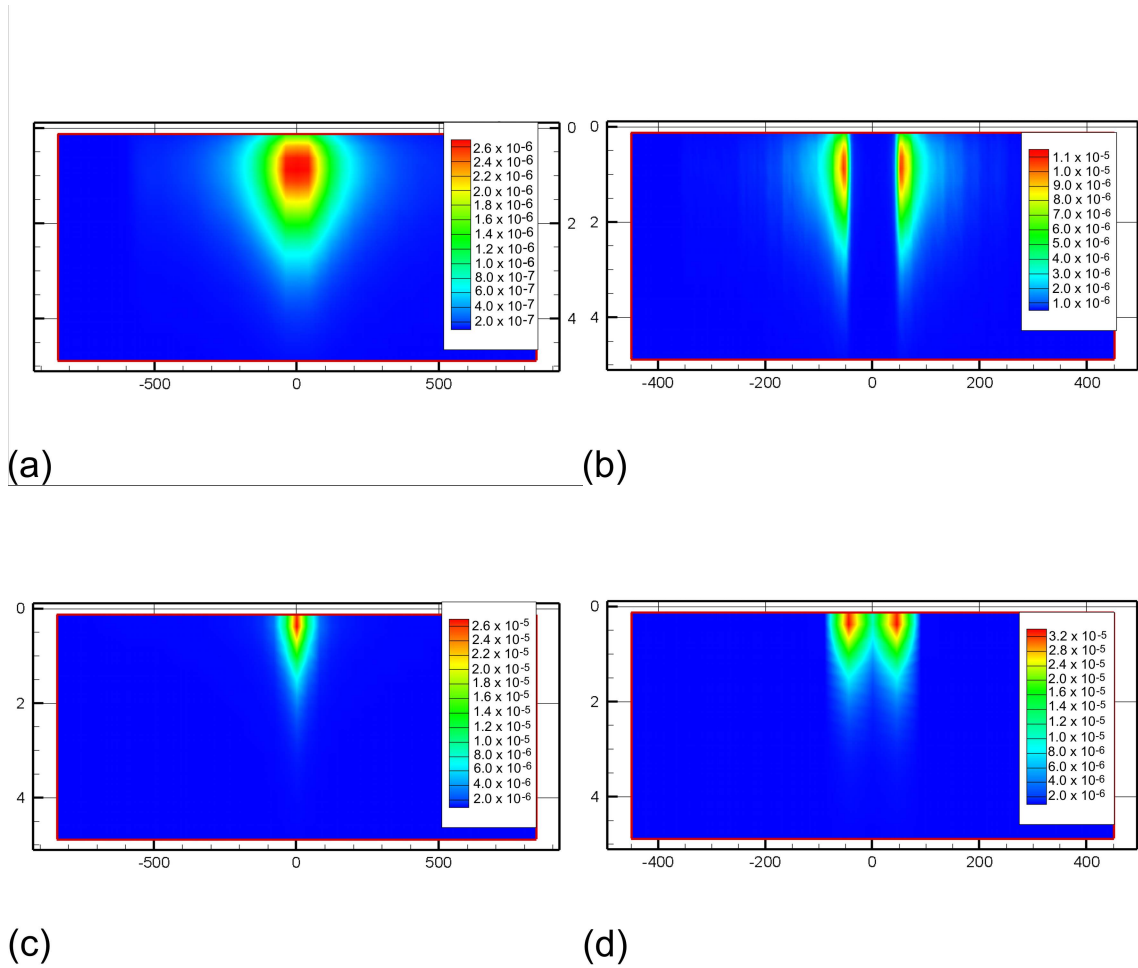


Figure 3.2 Electron distribution (in  $1/\text{nm}^3$  normalized using the initial kinetic energy of electrons) inside the workpiece for various applied voltages, gap distances and tip geometries: a) 300 V, 50 nm gap, round tip; b) 300 V, 50 nm gap, flat tip; c) 50 V, 10 nm gap, round tip; d) 50 V, 10 nm gap, flat tip. The axis are in nm and in all cases the CNT had a radius of 50 nm and a length of  $4 \mu\text{m}$ .

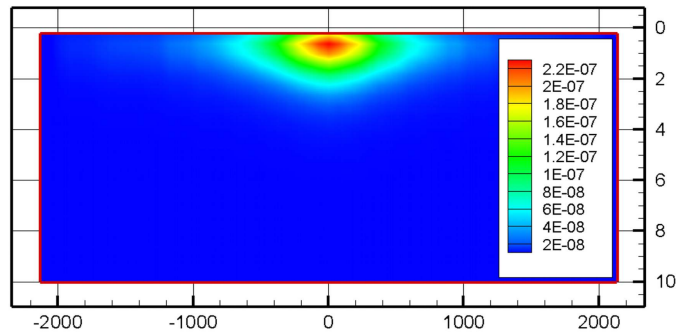
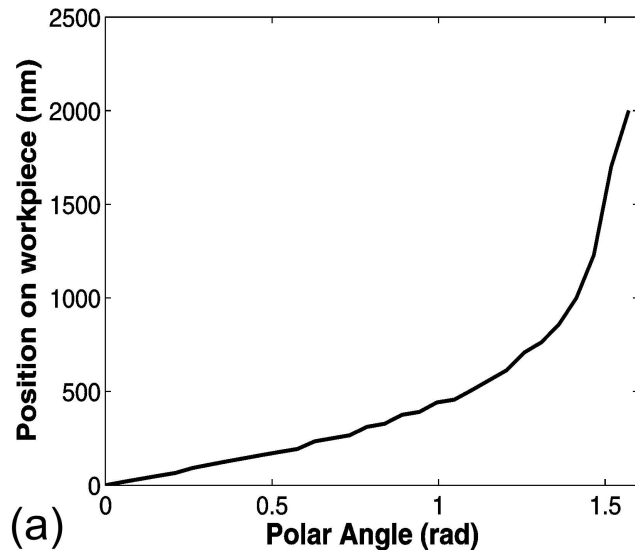


Figure 3.3 a) Electron spread on the surface of the workpiece. b) Electron energy density ( $1/\text{nm}^3$ ) obtained from the MC solution of the EBTE based on the input profile in a). The axes are in nm.

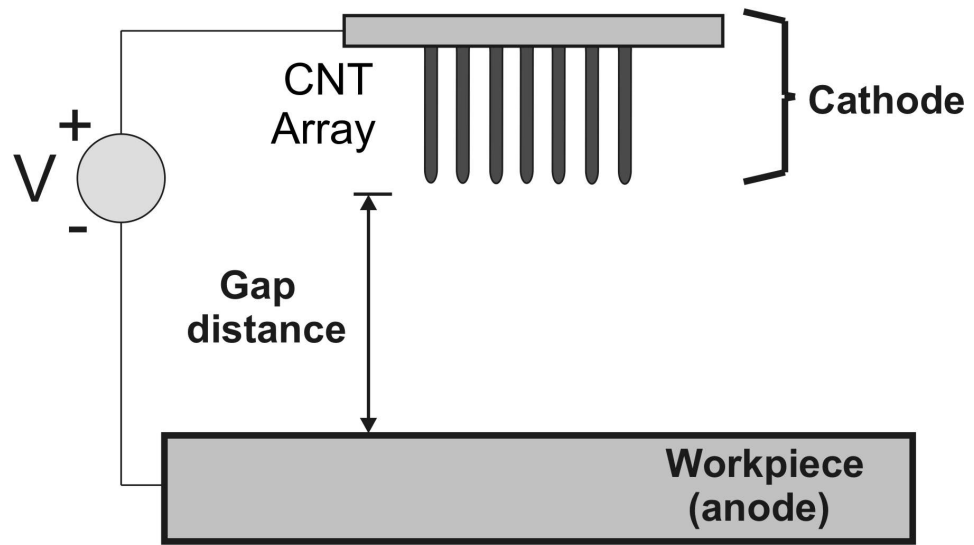


Figure 3.4 Field-emission from an array of CNT grown on a substrate.

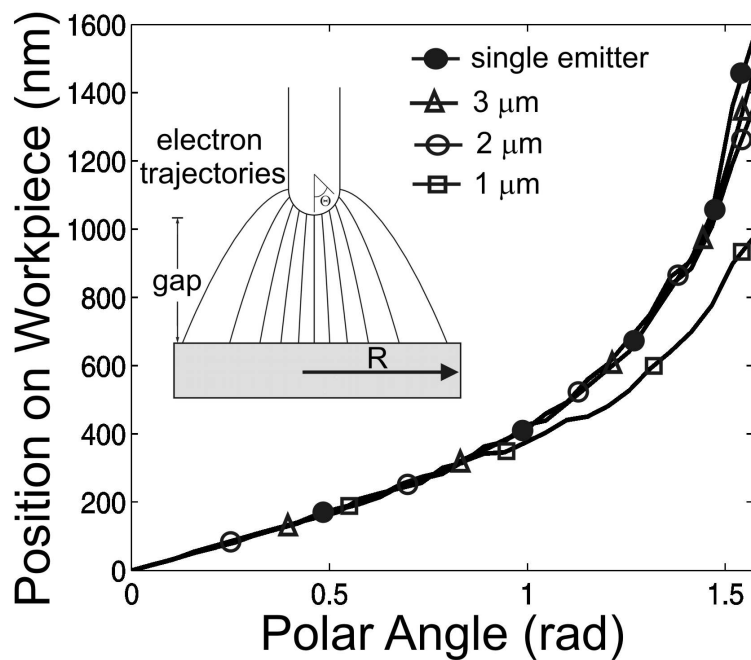


Figure 3.5 Radial profile of electrons on the workpiece as a function of electron emission from a particular polar angle on the tip. In all cases the applied voltage was 200 V and the gap distance 300 nm. The results are shown for a single CNT and for the CNT in the center with the effect of the emission of the CNTs around it separated by different distances. The inset shows the initial launching positions of the electrons on the periphery of the CNT tip.

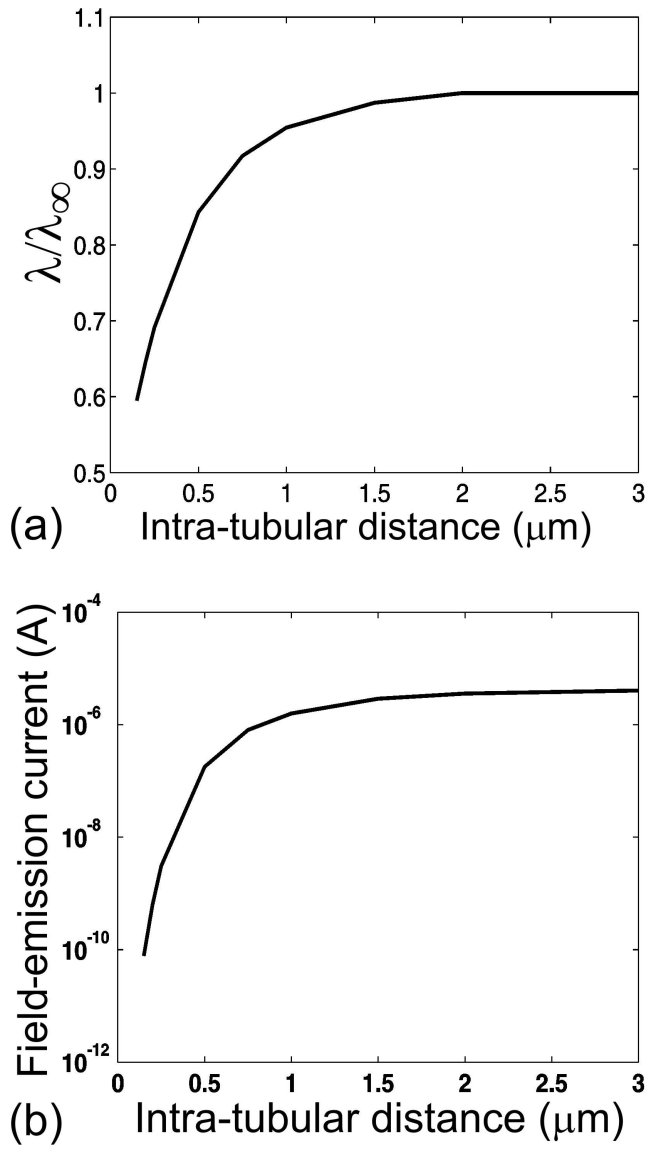


Figure 3.6 a) Normalized amplification factor as a function of the intra-tubular distance. b) Field-emission current on the CNT in the center as a function of the intra-tubular distance calculated following the methods in (Sanchez and Mengüç 2008b).

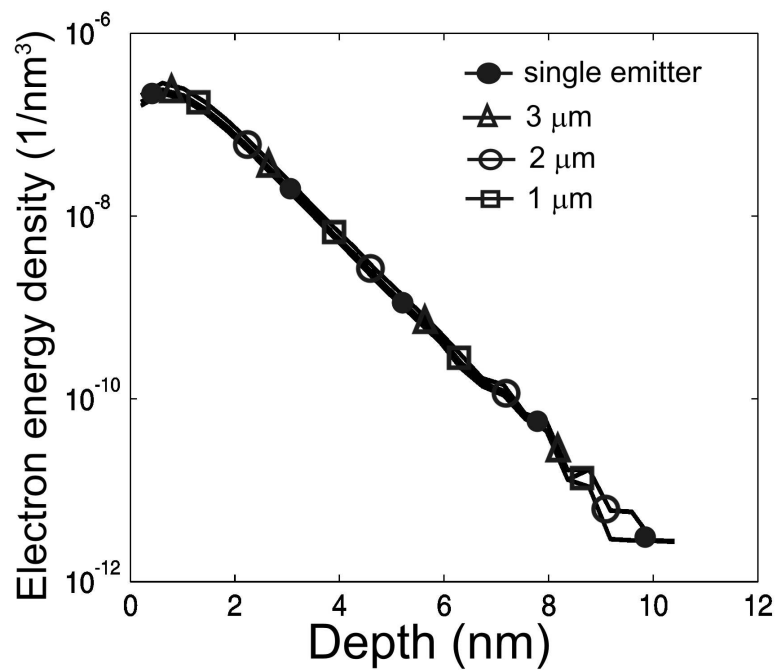


Figure 3.7 Electron energy density deposited inside a gold thin film for a single CNT emitter and multiple emitters separated by intra-tubular distances indicated in the plot. These results suggest that the electron deposition profiles are not a function of the array geometry.

## CHAPTER 4 MOLECULAR DYNAMICS THEORY

How does one define melting at the nanoscale? How much energy is required to make a “nano-hole” on a surface? How many atoms comprise this “nano-hole” and where do they go when the material is removed? How does one define a solid, a liquid or a vapor? None of these questions can be answered with the theory that has been presented thus far, as precise knowledge of atomic positions and velocities cannot be readily obtained from such continuum approaches. The purpose of this Chapter is to present the theory that can provide an answer to these questions, as well as the numerical methodology used to apply it to this problem.

### 4.1 An Adiabatic Theory of Lattice Vibrations

At first glance, a theory of lattice vibrations would appear impossibly daunting. One has  $N \approx 10^{23}$  atoms interacting strongly with  $M$  electrons. However, there is a natural expansion parameter for this problem, which is the ratio of the electronic to the atomic mass ( $m_e$  and  $m_a$  respectively):

$$\frac{m_e}{m_a} \ll 1 \quad (4.1)$$

which allows us to derive an accurate theory.

Due to Newton’s third law, the forces on the atoms and electrons are comparable  $F \sim e^2/a^2$ , where  $a$  is the lattice constant. If one can imagine that, at least for small displacements, the forces binding the electrons and atoms to the lattice may be modeled as harmonic oscillators, then

$$\frac{\omega_{atom}}{\omega_{electron}} \sim \left( \frac{m_e}{m_a} \right)^{1/2} \sim 10^{-3} - 10^{-2} \quad (4.2)$$

which means that the atom is essentially stationary during the period of the electronic motion. For this reason one may take an adiabatic approximation (Ashcroft and Mermin 1976):

- The atoms are treated as stationary at locations  $\mathbf{R}_1, \dots, \mathbf{R}_N$  and determine the electronic ground state,  $E(\mathbf{R}_1, \dots, \mathbf{R}_N)$ . This may be done using standard *ab-initio* band structure techniques.
- This potential is then used for the atoms; i.e.  $E$  is recalculated as a function of the atomic locations, always assuming that the electrons remain in their ground state.

Thus the potential energy of the atoms is

$$U(\mathbf{R}_1, \dots, \mathbf{R}_N) = E(\mathbf{R}_1, \dots, \mathbf{R}_N) + \text{atom-atom interaction} \quad (4.3)$$

Using the theorem of translational invariance (Ziman 1964), Eq. (4.3) can be rewritten as a function of the distance between the atoms

$$\begin{aligned} U(\mathbf{R}_1, \dots, \mathbf{R}_N) = & \sum_i u_1(\mathbf{r}_i) + \sum_i \sum_{j>i} u_2(\mathbf{r}_i, \mathbf{r}_j) + \sum_i \sum_{j>i} \sum_{k>j>i} u_3(\mathbf{r}_i, \mathbf{r}_j, \mathbf{r}_k) \\ & + \dots + \sum_i \sum_{j>i} \sum_{k>j>i} \dots \sum_{N>\dots>k>j>i} u_N(\mathbf{r}_i, \mathbf{r}_j, \mathbf{r}_k, \dots, \mathbf{r}_N) \end{aligned} \quad (4.4)$$

where  $\mathbf{r}_i$  is the position of the  $i$ th particle, and the inequality signs for the summations are to avoid repeated counting of individual atoms. Equation (4.4) corresponds to the interatomic potential of an  $N$ -body system of particles with one-body, two-body, three-body, and so on, interactions (Stillinger and Weber 1985).

From the derivative of the potential, Eq. (4.4), one can calculate the force on each atomic site so that the equation of motion is

$$m_i \frac{d^2 \mathbf{r}_i}{dt^2} = -\nabla_{\mathbf{r}_i} U(\mathbf{R}_1, \dots, \mathbf{R}_N) \quad (i = 1, 2, \dots, N) \quad (4.5)$$



Equation (4.5) represents a total of  $3N$  equations due to the three Cartesian components of  $\mathbf{r}_i$  (only if translational motion is considered). The major tasks of a MD simulation are to solve these  $3N$  equations, also known as the many-body problem, and then analyze the simulation results to obtain the information of interest.

## 4.2 Interatomic Potential

A crucial step in a MD simulation is the choice of the potential energy function between atoms or the “interatomic potential” in that it determines how realistic the simulations would be. In this work, the focus is on face-centered-cubic (FCC) materials and so a corresponding interatomic potential is discussed.

An interatomic potential suitable for FCC materials was proposed by Daw and Baskes (1984). Their model is based on the assumption that the total electron density in a metal is reasonably approximated by the linear superposition of contributions from the individual atoms. The electron density in the vicinity of each atom can then be expressed as a sum of the electron density contributed by the atom in question plus that contributed by all the surrounding atoms. This latter contribution to the electron density is a slowly varying function of position and can be approximated as constant. The potential energy of this atom is then the energy associated with the electrons of the atom plus a contribution due to the constant background electron density. This sum defines an embedding energy of an atom as a function of the background electron density and the atomic species. In addition, there is a repulsive electrostatic energy component due to core-core overlap of atoms. Under this picture, the embedded-atom method gives the total energy in the form:

$$U = \sum_{i=1}^N u_i \left[ \sum_{j \neq i} \rho_a(r_{ij}) \right] + \frac{1}{2} \sum_{i=1}^N \sum_{\substack{j=1 \\ j \neq i}}^N u_{ij}(\mathbf{r}_{ij}) \quad (4.6)$$

where  $u_i$  is the energy needed to embed atom  $i$  in the background electron density  $\rho$  with origins in the density functional theory (Kohn and Sham 1965),  $\rho_a$  is the angle-averaged radial electronic charge density function obtained from the Hartree-Fock calculations for free atoms (Clementi 1974), and  $u_{ij}$  is the core-core pair repulsion between atoms  $i$  and  $j$  separated by the distance  $\mathbf{r}_{ij}$ . The first term on the right-hand side of Eq. (4.6) represents a

many-body type of interaction if  $u_i$  is a nonlinear function, but reduces to a pair interaction otherwise (Daw and Baskes 1984). The forms of the embedding function of several FCC metals are chosen to be cubic splines fitted to bulk experimental data such as the sublimation energy, equilibrium lattice constant, elastic constants, and vacancy-formation energies of the pure metals and the heats of solution of the binary alloys (Foiles et al. 1986). When applied to solid surfaces, the parameters for the potential are not changed, nor are additional adjustable parameters introduced. Therefore, the model is surface parameter free. This is not the case, for instance, when an effective (classical) lattice Hamiltonian is used and the interaction between two surface atoms is different from that of two bulk atoms (Wang et al. 1988).

#### 4.3 Integration of Equations of Motion

Once a suitable interatomic potential is selected, Eq. (4.5) needs to be integrated to find the trajectories of the atoms in the system. The velocity-Verlet algorithm can be used for this purpose with the trajectory of atom  $i$  determined by (Swope et al. 1982):

$$\mathbf{r}_i(t + \Delta t) = \mathbf{r}_i(t) + \mathbf{v}_i(t)\Delta t + \frac{\Delta t^2}{2m}\mathbf{F}_i(t) \quad (4.7)$$

and the velocities by:

$$\mathbf{v}_i(t + \Delta t) = \mathbf{v}_i(t) + \frac{\Delta t}{2m}[\mathbf{F}_i(t + \Delta t) + \mathbf{F}_i(t)] \quad (4.8)$$

Note that in this algorithm, one can compute the new velocities only after computing the new positions and, from these, the new forces. Equation (4.7) is accurate to order  $\Delta t^4$  and it can be proven rigorously that Eq. (4.7) and Eq. (4.8) are equivalent to the original Verlet algorithm (Frenkel and Smit 2002). A detailed discussion of other integration schemes and the importance of numerical accuracy are given by Frenkel and Smit (2002). A timestep of 1 fs is usually recommended when using the EAM as the interatomic potential.

#### 4.4 Boundary Conditions

Molecular dynamics is typically applied to systems containing several hundreds or a few thousand atoms. Such small systems are dominated by surface effects – interactions of the atoms with the container walls. The problem of surface effects can be overcome by implementing periodic boundary conditions (Born 1912). The periodic boundary condition is equivalent to filling the whole space with identical copies of the simulated region as shown in Fig. 4.1. The central box in Fig. 4.1 is called the primary cell which has volume  $V$  and  $N$  particles; it is representative of the bulk material to the extent that the bulk is assumed to be composed of the primary cell surrounded by exact replicas of itself. These replicas are called image cells. The image cells are each the same size and shape as the primary cell and each image cell contains  $N$  atoms, which are images of the atoms in the primary cell. In the course of the simulation, as a particle moves in the primary cell, its periodic image in each of the neighboring cells moves in exactly the same way. Thus, as a particle leaves the primary cell, one of its images will enter through the opposite face. There are no walls at the boundary of the central box, and no surface particles.

As particle 1 moves through a boundary, its images 1' and 1'', move across their corresponding boundaries. The number density in the primary cell (and hence in the entire system) is conserved. It is not necessary to store the coordinates of all images in a simulation, just the particles in the primary cell. For a surface simulation, the model usually adopted is that of the *slab*: a thick slice of material, delimited by two free surfaces. This is simply obtained by removing the periodic boundary conditions along one direction (usually taken to be  $z$ ) while retaining them in the orthogonal plane. Therefore, a slab must be thought as replicated to infinity in the  $xy$  plane, but there is no replication along the slab normal  $z$ .

An effect of the periodic boundary condition is that an atom lying within a cutoff distance of a boundary interacts with atoms in adjacent copies of the system, or equivalently, with atoms near the opposite face. In general, the force acting on particle  $i$  is

$$\mathbf{F}_i = \sum_{\alpha} \sum_j \mathbf{F} \left[ \mathbf{r}_{ij} - (n_x L_x + n_y L_y + n_z L_z) \right] \quad (4.9)$$

where  $L_x$ ,  $L_y$  and  $L_z$  are the lengths of the simulation cell in each direction,  $n_x$ ,  $n_y$ , and  $n_z$  are integers, and  $(n_x L_x + n_y L_y + n_z L_z)$  is a translation vector. In the calculation of equilibrium properties, it has been found that using periodic boundary conditions introduces a negligible effect (Pratt and Haan 1981). For transport phenomena, such as in silicon (Sun and Murphy 2006), the correct size of the boundary needs to be set according to the wavelength of the thermal excitations.

#### 4.5 Statistical Ensembles

The integration of the equation of motion, Eq. (4.5), samples the microcanonical ensemble naturally. That is, the integration of the equations of motion is done conserving the number of particles  $N$  and the volume  $V$ ; since the system is assumed to be isolated, no energy exchange occurs so that the energy  $E$  of the system is also conserved. In practice, one is often more interested in determining how system properties depend on temperature or pressure. The former can be achieved by sampling the canonical ensemble (constant number of particles  $N$ , volume  $V$  and temperature  $T$ ) and the latter by sampling the isobaric ensemble (constant number of particles  $N$ , pressure  $P$  and temperature  $T$ ). Numerically, these ensembles can be sampled by direct modification of the equations of motion (Andersen 1980; Hoover 1986; Nose 1986) or by explicit velocity rescaling (Berendsen et al. 1984).

#### 4.6 Analysis of Atomic Trajectories

The general outputs of the simulation are the positions and velocities of the atoms. In order to extract useful information from these results, statistical methods can be used to find a correlation between trajectories and different quantities of interest. In the following subsections the general numerical tools available to analyze the atomic trajectories that link them to actual physical quantities that can be observed and measured are presented. In subsequent chapters these expressions are used for the calculations presented then.

#### 4.6.1 Equipartition Theorem and the Virial

The equipartition theorem is a principle of classical (non-quantum) statistical mechanics which states that the internal energy of a system composed of a large number of particles at thermal equilibrium will distribute itself evenly among each of the quadratic degrees of freedom allowed to the particles of the system (Haile 1992). In MD simulations, the equipartition theorem is used to set the velocities of a group of atoms to a given temperature:

$$\frac{3}{2} Nk_B T = \sum_{i=1}^N \frac{1}{2} m_i \left[ (v_{i,x} - v_{CM,x})^2 + (v_{i,y} - v_{CM,y})^2 + (v_{i,z} - v_{CM,z})^2 \right] \quad (4.10)$$

where  $k_B$  ( $1.381 \times 10^{-23}$  J/K) is Boltzmann's constant,  $T$  is the temperature of the system of  $N$  atoms,  $m_i$  is the mass,  $v_{i\alpha}$  is the instantaneous velocity of the  $i$ -th atom ( $\alpha = x, y, z$ ) and  $v_{CM,\alpha}$  is the velocity component of the center of mass of the group of atoms considered for the temperature calculations. This consideration distinguishes between the thermal velocity of the atoms and the velocity of their collective motion ( $v_{CM,\alpha}$ ).

In statistical mechanics and expression for the pressure is usually derived starting from the virial theorem of classical dynamics (Gray 1984). For spheres interacting with pairwise intermolecular forces the result is (Haile 1992):

$$P = \frac{Nk_B T}{V} + \frac{1}{3V} \left\langle \sum_{i < j} \sum \mathbf{F}_{ij} \cdot \mathbf{r}_{ij} \right\rangle \quad (4.11)$$

where  $P$  is the pressure on  $N$  atoms contained in volume  $V$  at temperature  $T$ ,  $\mathbf{F}_{ij}$  is the force acting between atoms  $i$  and  $j$ , and the angle brackets represent the time average. The time averaged quantity in Eq. (4.11) is the virial.

#### 4.6.2 Determination of Phase Change

For simulations of nanomachining via MD, one needs to identify the time at which a region of the simulation box that changed its phase from solid to liquid to gas. There are several qualitative ways to define a molten layer (Carnevali et al. 1987): (a) when the

interlayer pair correlation functions lose their crystalline shell structure (such as the radial distribution function (RDF) and structure factor described below); (b) if the diffusion is linear with time and large; (c) if the average energy per atom is larger than in a typical bulk layer; (d) if the in-plane orientational order parameter has dropped from close to 1 to close to 0.

A crystalline solid has two kinds of order, translational and orientational. Translational order means that, if one starts at a particular atom and take steps along well-defined paths over long distances, one will arrive in close proximity to another atom. Orientational order means that, if one looks at two atoms separated by large distances, their neighbors will be oriented relative to some fixed axis in the same way. A liquid has no long-range order of either kind, but it has short-range order: any atom will have some average number of nearest neighbors clustered around an average neighbor distance with no preferred orientation. Changes in structure of a surface are related to the loss of long-range translational order; melting refers to the loss of the short-range orientational order. To determine the latter the local order parameter is calculated (Morris and Song 2002)

$$\Psi_i = \left| \frac{1}{6} \frac{1}{Z} \sum_{j=1}^Z \sum_{k=1}^6 \exp(i\mathbf{q}_k \cdot \mathbf{r}_{ij}) \right|^2 \quad (4.12)$$

where the first summation with  $k$  is over a set of six vectors  $\{\mathbf{q}_k\}$  chosen so that  $\exp(i\mathbf{q}_k \cdot \mathbf{r}_{ij}) = 1$  for any vector  $\mathbf{r}_{ij}$  connecting atom  $i$  with atom  $j$  in the first- or second-neighbor shell in a perfect FCC lattice, and the second summation with  $j$  is over all the atoms found within a cutoff distance  $r_{cut}$  from atom  $i$ . Figure 4.2 depicts the idea behind the calculation using Eq. (4.12).

When the system is at 0 K  $\mathbf{q}_k$  and  $\mathbf{r}_{ij}$  are parallel to each other and  $\exp(i\mathbf{q}_k \cdot \mathbf{r}_{ij}) = 1$ . When the temperature increases, the natural displacement of the atoms makes  $\exp(i\mathbf{q}_k \cdot \mathbf{r}_{ij}) < 1$  as  $\mathbf{q}_k$  and  $\mathbf{r}_{ij}$  cease to be parallel. As the temperature increases further, the relative displacement of  $\mathbf{r}_{ij}$  with respect to  $\mathbf{q}_k$  makes  $\exp(i\mathbf{q}_k \cdot \mathbf{r}_{ij}) \rightarrow 0$  indicating loss of

orientational order as described above. This makes Eq. (4.12) useful for identifying the solid-to-liquid transition.

One of the most widely used means of identifying phase change is the calculation of the radial distribution function (RDF)  $g(\mathbf{r})$ . The RDF measures how atoms organize themselves around one another (Haile 1992). It is defined as:

$$\rho g(\mathbf{r}) = \frac{1}{N} \left\langle \sum_i^N \sum_{j \neq i}^N \delta[\mathbf{r} - \mathbf{r}_{ij}] \right\rangle \quad (4.13)$$

where  $\rho = N/V$  is the number density, and the angular brackets represent a time average. Physically, Eq. (4.13) can be interpreted as the ratio of a local density  $\rho(r)$  to the system density  $\rho$ . The behavior of  $g(\mathbf{r})$  in crystalline solids is very different from that for gases at low density. For atoms frozen onto the sites of regular crystal lattice structures-such as FCC, BCC, HCP-  $g(\mathbf{r})$  takes the form of a sequence of delta symbols (Fig. 4.3a). For liquids and amorphous solids the behavior of  $g(\mathbf{r})$  is intermediate between crystal and gas: liquids exhibit *short-range* order similar to that in crystals, but *long-range* disorder like that in gases (Haile 1992) (Fig. 4.3b).

#### 4.7 MD codes

There are several MD codes freely available. Among them, the most commonly used are CHARMM (Chemistry at Harvard Molecular Mechanics), AMBER (Assisted Model Building with Energy Refinement), GROMACS (Groningen Machine for Chemical Simulations) and LAMMPS (Large Atomic/Molecular Massive Parallel Simulator) (Plimpton 1995). The first three codes are designed primarily for modeling biological molecules, which are usually in the range of hundreds of atoms. Because of the way in which GROMACS is coded it can also be used to simulate a large number of atoms, such as the number required for a nanostructure; however, this code has been extended more towards the simulation of polymers. The code LAMMPS can be used to represent complex systems and comes with a variety of interatomic potentials readily available for implementation. It can also be used together with the other codes mentioned above to

simulate particular problems. Because of the ease of use of LAMMPS this code was chosen to perform for the nanomachining simulations.

Before running the simulations of nanomachining, one needs to establish the validity of the code. Specifically, the ability of the EAM, Eq. (4.6), to accurately represent FCC elements. For this reason, two specific cases were tested: bulk simulations (surface free materials with periodic boundaries) and surface simulations (one boundary fixed to represent a surface and the rest periodic).

#### 4.7.1 Bulk Simulations

A crystal consisting of 864 atoms arranged in a cube is used with periodic boundary conditions in all directions. The system contains 12 atomic layers with 72 atoms per layer. The linear thermal expansion of the crystal was studied as a function of temperature. Initially, the temperature of the system is scaled to 0 K; then one moves on to each successively higher temperature from the well equilibrated sample at the lower temperature, in steps of 100 K first (as suggested by (Bilalbegovic and Tosatti 1993)) and then 50 K. A 20 ps constant-temperature equilibration run is made to ensure that the surface relaxation process has completed and that the system is equilibrated at the desired temperature. Afterwards, the system is left undisturbed in a 2.5 ns constant-pressure simulation during which the volume of the box occupied by the atoms for each temperature is stored. Three materials (Au, Ag and Cu) are simulated and the results of the simulated thermal expansion are compared to available experimental data (Touloukian 1975). The time integration is carried following the isobaric ensemble where the number of particles, pressure and temperature (NPT) of the system remain constant (Hoover 1986; Nose 1986). The NPT ensemble was used because it allows for the crystal to expand under constant pressure. For each constant pressure/temperature run, the volume of the simulation box was measured and the ratio of that volume with the prescribed volume at 0 K was calculated. This ratio is directly proportional to the expansion coefficient which can be compared with published results. Figure 4.4 shows the results from these simulations.



Excellent agreement was found between the calculated linear thermal expansion of Cu, Ag and Au with available experimental data (Touloukian 1975) which validates the code.

#### 4.7.2. Surface Simulations

For these simulations, a system with a free surface along the  $z$ - axis was defined and periodic boundary conditions along  $x$ - and  $y$ -. This corresponds to a free standing thin film. In order to avoid size effects due to the finite thickness of the film a larger box size was used than in the previous case (Al-Rawi et al. 2000). A system consisting of 15264 atoms arranged in 53 layers with 288 atoms per layer is considered. As before, the temperature of the system is scaled initially to 0 K and then one moves on to each successively higher temperature from the well equilibrated sample at the lower temperature, in steps of 100 K first (Bilalbegovic and Tosatti 1993) and then 50 K. A 20 ps constant-temperature equilibration run is made to ensure that the surface relaxation process has completed and that the system is equilibrated at the desired temperature. Afterwards, the system is left undisturbed in a 2.5 ns constant-energy simulation (NVE) during which the positions and velocities of the atoms are stored. One can calculate the phonon spectral densities of the surface defined as the power spectrum of the velocity-velocity correlation function for a given wave vector  $\mathbf{k}$  (Yang et al. 1991)

$$g_{\alpha\alpha}(\omega, \mathbf{k}) = \int dt e^{i\omega t} \frac{\langle v_{\alpha}(\mathbf{k}, t) v_{\alpha}(-\mathbf{k}, t) \rangle}{\langle v_{\alpha}(\mathbf{k}, 0) v_{\alpha}(-\mathbf{k}, 0) \rangle} \quad (4.14)$$

where

$$v_{\alpha}(\mathbf{k}, t) = \frac{1}{N} \sum_{j=1}^N e^{i\mathbf{k} \cdot \mathbf{R}_j(t)} v_{j\alpha}(t) \quad (4.15)$$

is the staggered layer average,  $N$  is the number of atoms per layer,  $\alpha = x, y, z$  is the polarization,  $\mathbf{R}_j(0)$  is the equilibrium position of the  $j$ th atom and  $\langle \rangle_{\tau}$  represents an average over the starting times  $\tau$ . The values of  $v_{j\alpha}$  correspond to the decompositions of

the velocity of each atom  $v_j$  into three components to the approximate eigenvectors of the modes, i.e.

$$\mathbf{v}_j = v_{jL}\hat{e}_L + v_{jT}\hat{e}_T + v_{jz}\hat{e}_z \quad (4.16)$$

where the vectors  $\hat{e}_L$ ,  $\hat{e}_T$  and  $\hat{e}_z$  correspond to a particular polarization mode. These modes are characterized by a two-dimensional wave vector  $\mathbf{k} = (k_x, k_y)$  that is perpendicular to the surface normal  $\mathbf{n}$ ; the plane defined by  $\mathbf{k}$  and  $\mathbf{n}$  is called the sagittal plane (Derouffignac et al. 1981). The modes are labeled as  $\hat{e}_T$  as SH (shear horizontal) when the displacements are normal to the sagittal plane, and the modes  $\hat{e}_L$  as  $SP_{\parallel}$  and  $\hat{e}_z$  as  $SP_{\perp}$  mode when the displacements are in the sagittal plane, parallel or perpendicular to  $\mathbf{k}$  (Derouffignac et al. 1981). The phonon spectral densities of the Cu(100) surface are calculated at position X in the 2D surface Brillouin zone with the corresponding wave vector as described by Koleske and Sibener (1992). Figure 4.5 shows these calculations.

In Fig. 4.5 the green peak corresponds to the  $SP_{\parallel}$  ( $S_1$ ) mode, the red peak to the SH ( $S_4$ ) mode and the blue peak to the  $SP_{\perp}$  ( $S_6$ ) mode; these modes are labeled following their work. Yang et al. (1991) studied the temperature behavior (up to 600 K) of the phonon modes at various positions in the surface Brillouin zone for the Ag(100) and Cu(100) surfaces. Our results are in perfect agreement with theirs when comparing the frequency of the modes at 300 K. In their work, the results obtained for the power spectrum were convoluted with a Gaussian distribution due to the small number of averages. In our case, that was not necessary because of the longer simulation time during which the data was collected. Their analysis was extended up to 900 K and found similar trends in the temperature behavior of the modes. In general, the frequency of the  $SP_{\parallel}$  ( $S_1$ ) mode decreases by almost 50% at high temperatures. Also, comparison with experimental results obtained via electron energy loss spectroscopy (EELS) (Chen et al. 1991) show good agreement with our calculations.

#### 4.8 Comments

In this Chapter an overview of the molecular dynamics method was given. In order to simulate the process of nanomachining the EAM was chosen as the interatomic potential that is realistic as seen by the calculations of bulk thermal expansion as well as surface vibrations. The task is now the coupling between this method and ones described in the previous Chapters.

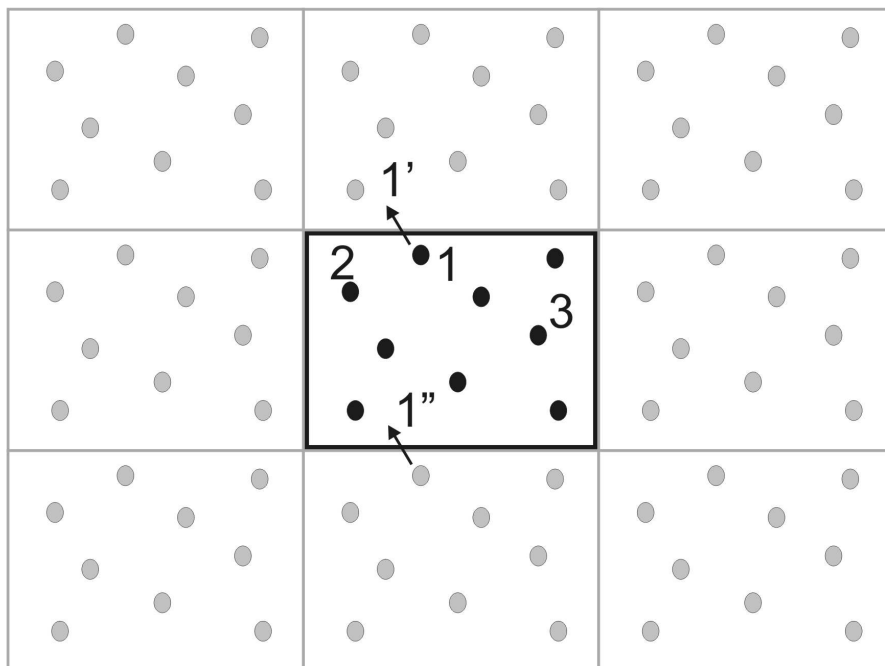


Figure 4.1 Periodic boundary condition used in molecular dynamics simulations

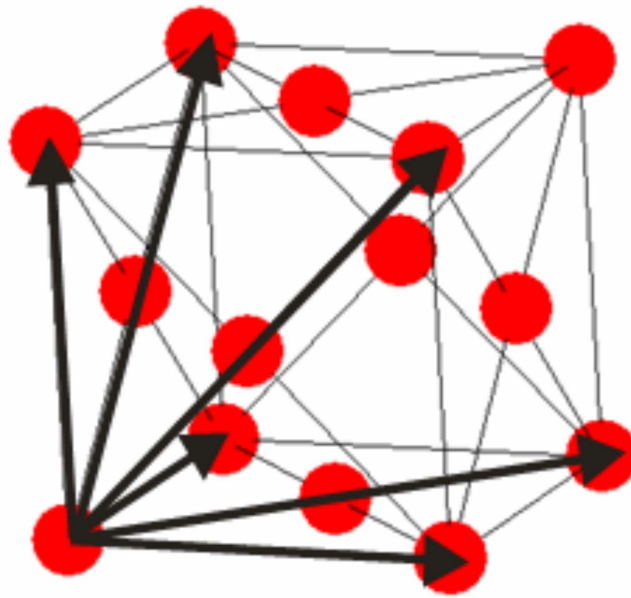


Figure 4.2 Equilibrium positions of atoms in the FCC structure. The arrows indicate the directions of vectors along the equilibrium lines.

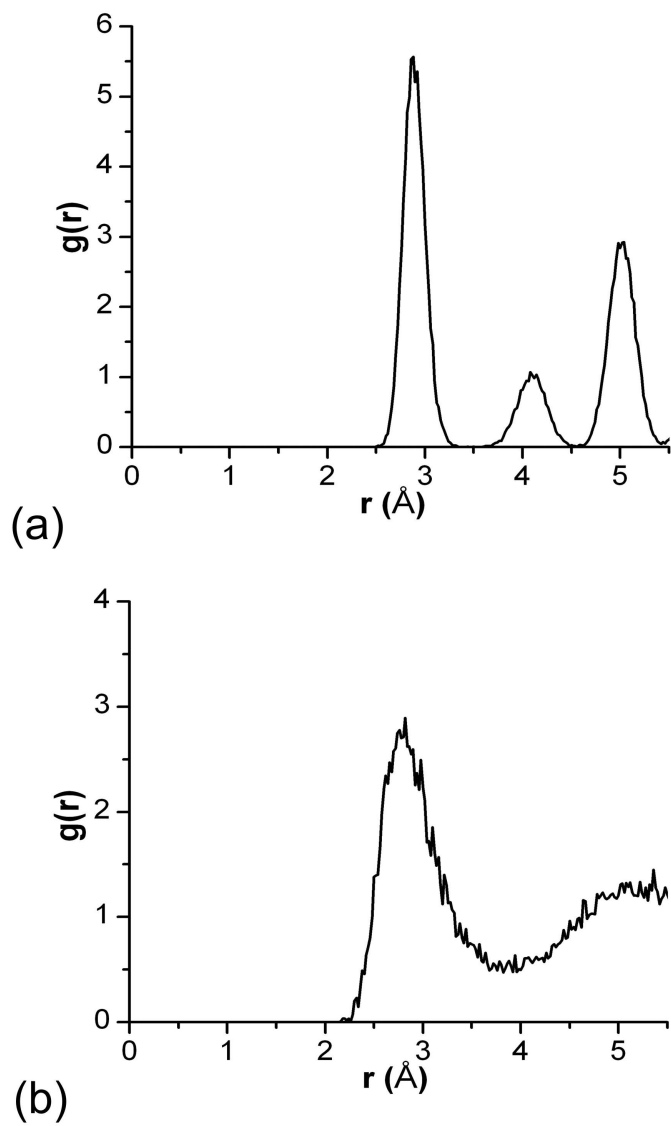


Figure 4.3 Common trends of the RDF: a) Solid phase; b) Liquid phase

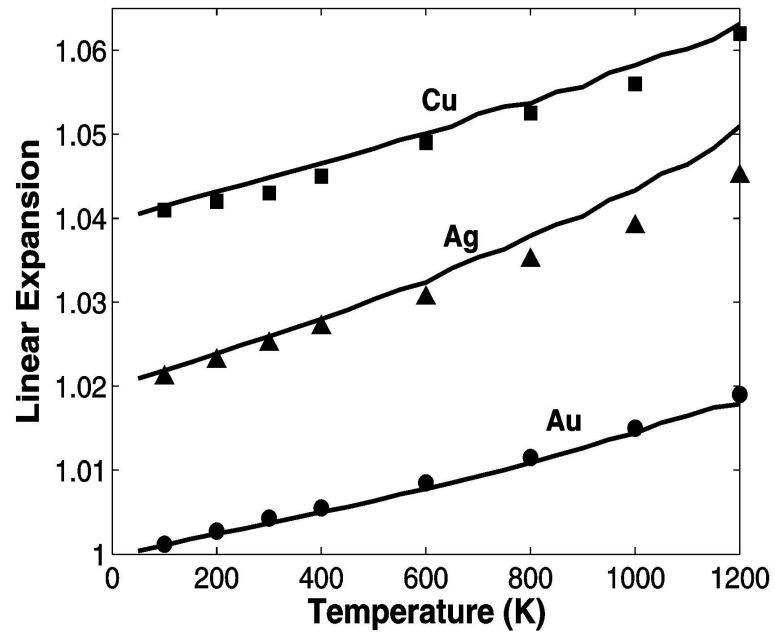


Figure 4.4 Linear thermal expansion for Cu, Ag, and Au. The vertical axis applies to Au and the other curves are offset by 0.02. The experimental data from (Touloukian 1975) are plotted as points, and the calculated values are plotted as curves.

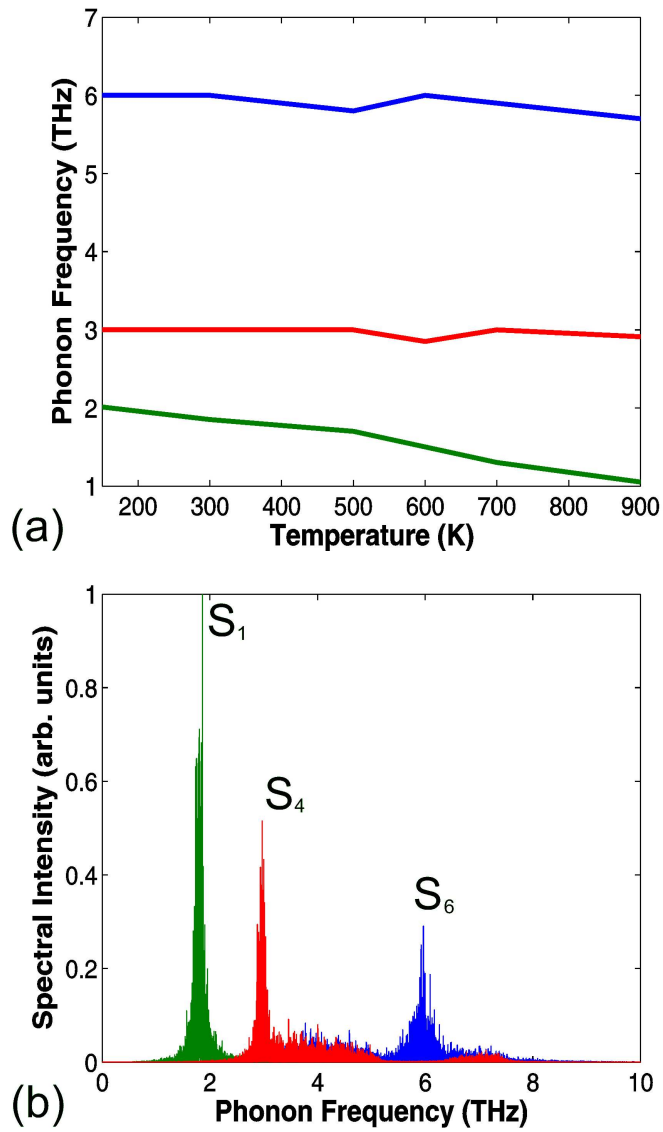


Figure 4.5 Phonon modes of the first atomic layer of Cu(100) at position X of the surface Brillouin zone: a) phonon frequency as a function of temperature; b) spectral intensity at 300 K.



CHAPTER 5  
THE TWO TEMPERATURE MODEL COUPLED WITH MOLECULAR DYNAMICS:  
A HYBRID CONTINUUM-DISCRETE NUMERICAL APPROACH

Even though MD simulations offer a large capability to simulate different kinds of phenomena, as seen in the previous Chapter, they do not readily include a mechanism of energy transfer between different carriers, such as electrons. In this Chapter, a review is given of all the different numerical methods that have been developed to couple MD methods with other numerical approaches.

### 5.1 Coupling of the TTM with MD

The coupling of MD with the TTM has been studied extensively in the past, mainly to simulate laser-beam/material interactions (Hakkinen and Landman 1993; Schafer et al. 2002; Ivanov and Zhigilei 2003; Xu et al. 2004). All of these methods have their origin in the Langevin equation in which stochastic and friction terms are inserted into the equations of motion to study Brownian motion or the coupling of an isolated system to a heat bath (Reif 1965)

$$m_i \frac{d^2 \mathbf{r}_i}{dt^2} = - \sum_{\substack{j=1 \\ j \neq i}}^N \frac{\partial U(\mathbf{r}_{ij})}{\partial r_{ij}} - m_i \gamma_i \frac{d\mathbf{r}_i}{dt} + \mathbf{R}_i(t) \quad (5.1)$$

where the damping constants  $\gamma_i$  determine the strength of the coupling to the bath and  $\mathbf{R}_i$  is a Gaussian stochastic variable with zero mean. This equation corresponds physically to frequent collisions with light particles that form an ideal gas at temperature  $T_0$ . Through the Langevin equation the system couples not only globally to a heat bath, but is also locally subjected to random noise. Berendsen et al. (1984) showed that Eq. (5.1) can be rearranged into Eq. (5.2) considering that the stochastic variable  $\mathbf{R}_i$  is uncorrelated with the velocity of the particle  $d\mathbf{r}_i/dt$ :

$$m_i \frac{d^2 \mathbf{r}_i}{dt^2} = - \sum_{\substack{j=1 \\ j \neq i}}^N \frac{\partial U(\mathbf{r}_{ij})}{\partial r_{ij}} - \gamma \left( \frac{T_i - T_0}{T_i} \right) m_i \frac{d\mathbf{r}_i}{dt} \quad (5.2)$$

where  $T_l$  can be obtained from the theorem of equipartition of energy (Haile 1992). Eq. (5.2) corresponds to the Berendsen thermostat (Berendsen et al. 1984) and can be used in MD simulations to sample the canonical ensemble. One can also consider an isolated system at temperature  $T$  in contact with an energy reservoir set at a temperature  $T_0$ . The heat flux  $J$  acting on the contact boundary with area  $A_c$  between the isolated system and the energy reservoir can be written as

$$J = \alpha(T_0 - T) \quad (5.3)$$

The total energy variation of the isolated system can be written as

$$\rho C_p V \frac{\partial T}{\partial t} = A_c J \quad (5.4)$$

Combining Eq. (5.3) and (5.4)

$$\begin{aligned} \Rightarrow \frac{T_{t+\Delta t} - T}{\Delta t} &= \frac{A_c \alpha (T_0 - T)}{\rho C_p V} \\ \Rightarrow T_{t+\Delta t} &= T + \alpha' \Delta t (T_0 - T) \\ \Rightarrow \frac{T_{t+\Delta t}}{T} &= 1 + \alpha' \Delta t \left( \frac{T_0}{T} - 1 \right) \end{aligned}$$

Using the equipartition theorem one can write

$$\begin{aligned} \frac{3}{2} k_B T &= \frac{1}{2} m \mathbf{v}_T^2 \\ \Rightarrow \frac{T_{t+\Delta t}}{T} &= \left( \frac{\mathbf{v}_{T,t+\Delta t}}{\mathbf{v}_T} \right)^2 = 1 + \alpha' \Delta t \left( \frac{T_0}{T} - 1 \right) \end{aligned}$$

Finally, and considering  $\alpha' = 1/\tau_T$

$$\frac{\mathbf{v}_{T,t+\Delta t}}{\mathbf{v}_T} = \sqrt{1 + \frac{\Delta t}{\tau_T} \left( \frac{T_0}{T} - 1 \right)} \quad (5.5)$$

Equation (5.5) is equivalent to an explicit atomic velocity re-scaling that is a function of  $T_0$ , the timestep of the simulation  $\Delta t$  and the total duration of the heat bath exposure  $\tau_T$ .

$$\mathbf{v}_{i,t+1} = (\mathbf{v}_{i,t} - \bar{\mathbf{v}}_{i,t})\chi + \bar{\mathbf{v}}_{i,t} \quad (5.6)$$

with

$$\chi = \left[ 1 + \frac{\Delta t}{\tau_T} \left( \frac{T_0}{T_l} - 1 \right) \right]^{1/2} \quad (5.7)$$

where  $\mathbf{v}_i$  is the velocity of atom  $i$  and  $\bar{\mathbf{v}}_i$  is the average velocity of the atoms. In this formulation, the canonical ensemble can be sampled with the original equations of motion [without the damping force, i.e. Eq. (5.2)] but by applying the velocity re-scaling at the end of every step after the integration (Berendsen et al. 1984). The formulation in Eq. (5.7) was slightly modified and used by Wang and Xu (2002) and then later by Wang (2005) to study laser heating of metals. Their modified formulation reads

$$\chi = \left[ 1 + \frac{E}{m\mathbf{v}_T^2/2} \right]^{1/2} \quad (5.8)$$

where  $E$  is the energy from the laser deposited at particular region of volume  $V$  and  $m\mathbf{v}_T^2/2$  is the thermal kinetic energy of the atoms contained in that volume as described before. In their original work, the stepwise nature of the TTM is neglected and it was assumed through the rescaling with Eq. (5.8) that the energy of the laser is directly transferred to the lattice. The validity of this assumption is investigated in Section 5.5. Equation (5.8) can be used to rescale the velocities of the atoms in the boundary regions to account for a radiation boundary condition. In this way the energy is dissipated into the vacuum considering  $E = -A_c \varepsilon \sigma (T^4 - T_\infty^4)$  where  $\sigma$  ( $5.67 \times 10^{-8} \text{ W/m}^2\text{K}^4$ ) is Stephan-Boltzmann constant,  $\varepsilon$  is the emissivity and  $A_c$  is the surface area.

Considering that during laser heating it is the electrons in the conduction band that comprise the heat bath, Hakkinen and Landman (1993) used Eq. (5.2) by replacing  $T_0$  with the electron temperature  $T_e$ , and assuming that the damping constant  $\gamma = G/C_l$ . Their expression reads

$$m_i \frac{d^2 \mathbf{r}_i}{dt^2} = - \sum_{\substack{j=1 \\ j \neq i}}^N \frac{\partial U(\mathbf{r}_{ij})}{\partial r_{ij}} - \frac{G}{C_l} \left( \frac{T_l - T_0}{T_l} \right) m_i \frac{d\mathbf{r}_i}{dt} \quad (5.9)$$

The main drawback of Eq. (5.9) is that *a priori* knowledge of the lattice heat capacity is required that is, in general, a function of the temperature. This problem was overcome by Ivanov and Zhigilei (2003) who modified the damping term in Eq. (5.2) by replacing the atomic velocity with their thermal velocity  $\mathbf{v}_i^T$  defined as  $\mathbf{v}_i^T = \mathbf{v}_i - \bar{\mathbf{v}}_i$  and by modifying the damping constant, which yields

$$m_i \frac{d^2 \mathbf{r}_i}{dt^2} = - \sum_{\substack{j=1 \\ j \neq i}}^N \frac{\partial U(\mathbf{r}_{ij})}{\partial r_{ij}} - \xi m_i \mathbf{v}_i^T \quad (5.10)$$

with

$$\xi = \frac{\frac{1}{n} \sum_{k=1}^n G(T_l - T_e^k) V}{\sum_i m_i (\mathbf{v}_i^T)^2} \quad (5.11)$$

Here  $V$  is the volume occupied by a group of atoms where the electron temperature and the kinetic energy (in the denominator) are defined. The summation of the term in the numerator indicates the transfer of the total energy of the electrons to the lattice, considering that the electron equation [Eq. (3.7)] is solved with a much smaller time-step. A comparison between the damping term in Eq. (5.9) and Eq. (5.11) shows that

$$C_l = \frac{3k_B N}{V} \quad (5.12)$$

where  $N$  is the total number of atoms in volume  $V$ . Equation (5.12) is an implicit function of the temperature because the number of atoms  $N$  in a given discrete volume  $V$  changes due to thermal expansion.

Later, Xu et al. (2004) followed the second approach of Berendsen et al. (1984) [Eq. (5.6) and (5.7)] and modified the velocity re-scaling factor  $\chi$  to account for the electron-phonon coupling.

$$\chi = \left[ 1 - \frac{\Delta t G (T_i - T_e) V}{\sum_i \frac{1}{2} m_i (\mathbf{v}_i^T)^2} \right]^{1/2} \quad (5.13)$$

As is shown later, the formulations in Eqs. (5.10) and (5.11), and the velocity re-scaling of Eq. (5.13) are equivalent.

## 5.2 Numerical Considerations

The combined TTM with MD is also referred to as a hybrid approach because it entails the use of continuum and discrete numerical methods for the same problem. The TTM is used to calculate the electron temperature of the system, as well as to account for electron diffusion inside the material. The MD simulations use this information to integrate the equations of motion of the atoms in the material. Depending on the spread of the energy beam on the surface of the workpiece one can neglect radial variations and solve the one-dimensional (1D) problem or solve the full three-dimensional problem (3D) when these variations are an important part of the solution. Both of these situations are described below.

### 5.2.1 One-Dimensional (1D) Problems

When the electron beam is not focused, this numerical approach is adequate because it saves computational time by neglecting radial variations. In the simulations presented later in this Chapter, a free standing film with a thickness of 50 nm was considered, and with a lateral area of  $\sim 6$  nm x 6 nm depending on the material. Periodic boundary

conditions are used in the  $x$ - and  $z$ - axis, with the  $y$ - axis representing a free surface. The energy exchange between the two parts of the combined model is schematically illustrated in Fig. 5.1.

In order to solve Eq. (3.7) an implicit discretization given in Eqs. (3.13)-(3.15) can be used. The thermal expansion of the lattice in FD scheme is accounted for by counting the number of atoms in each cell during the course of the simulations. The simulations begin with a fixed number of FD cells. However, the atoms can move in and out of the cells during the simulations because of changes in their energy due to the energy beam. When the number of atoms in a particular region exceeds 10% of the average number density per cell a new FD cell is activated (Schafer et al. 2002; Ivanov and Zhigilei 2003). Also, when the number of atoms decreases below this limit, the cell is deactivated and the TTM is solved in the active number of cells. In the event that a cell between the two free surfaces becomes deactivated due to possible ablation of the material, a new adiabatic boundary is created and the TTM is solved for each section of the material.

### 5.2.2 Three-Dimensional (3D) Problems

The heating effect of a focused electron beam acting on the workpiece falls in a category of 3D problems because, unlike the previous case, the radial effects are now important. The simulations based on this approach are given in Chapter 7, however, the numerical implementation is described here. The continuum domain with volume  $L_x L_y L_z$  is divided into grid elements of volume  $\Delta x \Delta y \Delta z$ . A grid element length of  $\Delta x = \Delta y = \Delta z = 3a_0$  where  $a_0$  is the lattice constant of the material was chosen. A schematic of this model is shown in Fig. 5.2.

Inside each discrete element of the continuum domain, the MD domain is initially defined with 109 atoms per element. As the simulation of nanomachining is done the number of atoms in each element changes due to their atomic motion. Initially, the dimensions of the domain are 100 x 100 x 25 nm with periodic boundary conditions in the  $x$ - and  $z$ - directions and a surface defined on the  $y$ - direction. This model represents a free standing thin film. Thermal expansion is a natural consequence of solving the

equations of motion because at each time step one can determine the position of each individual atom. To account for thermal expansion new elements on the  $y$ - axis are activated if the number of atoms in a particular point in space, defined with the same dimensions of a discrete element, exceed 10% of the initial number of atoms in a regular element. However, in the event that the number of atoms in a region is less than this limit, the element is deactivated. In order to solve Eq. (3.7) the following implicit discretization is used

$$A_1 \left( T_{e,i+1,j,k}^{t+1} + T_{e,i-1,j,k}^{t+1} \right) + A_2 \left( T_{e,i,j+1,k}^{t+1} + T_{e,i,j-1,k}^{t+1} \right) + A_3 \left( T_{e,i,j,k+1}^{t+1} + T_{e,i,j,k-1}^{t+1} \right) - A_4 T_{e,i,j,k}^{t+1} - A_5 = 0 \quad (5.14)$$

with

$$A_1 = \frac{k_e}{\Delta x^2} \quad A_2 = \frac{k_e}{\Delta y^2} \quad A_3 = \frac{k_e}{\Delta z^2} \quad (5.15)$$

$$A_4 = 2(A_1 + A_2 + A_3) + G + \frac{C_e}{\Delta t} \quad (5.16)$$

$$A_5 = GT_{e,i,j,k}^t + \frac{C_e}{\Delta t} T_{l,i,j,k} + S \quad (5.17)$$

Just as in the 1D case in the previous section, the electronic thermal conductivity,  $k_e$ , and the electronic heat capacity  $C_e$  are evaluated at the electronic temperature in a given timestep,  $T_{e,ijk}^t$ . The matrix form of Eq. (5.14) results in a 7-banded matrix with  $N_x N_y N_z$  equations which can be solved numerically with the use of the Successive Over-Relaxation (SOR) method (Kumar 2006; Wong and Mengüç 2008). The general form of the SOR requires the relaxation parameter  $\omega$  that gives the largest convergence with the least number of iterations. A constant of  $\omega = 1.2$  was selected based on trial and error and obtained a converged solution with an error of less than  $10^{-6}$  with less than 10 iterations in the most extreme case. This is because the SOR method uses the recently calculated values in one point to calculate the next value of another. The electron temperature at the previous step at the previous step is used as the initial guess to begin the iterations.

Finally, the ghost node method is used to account for the adiabatic boundaries when solving the TTM, and the electron energy is not “defined” when material is not present.

### 5.3 Simulations of Laser Heating

In metals, laser light is absorbed by the conduction band electrons. The deposited energy is equilibrated quickly, within femtoseconds, among the electrons. This energy is subsequently transferred to the atomic vibrations, although more slowly. The latter process is controlled by the strength of the electron-phonon coupling and can take from a fraction of a picosecond to several tens of picoseconds. Finally, the thermal equilibrium is established between the electrons and phonons, and the heat flow from the surface region into the bulk of the irradiated target can be described as the common thermal diffusion. This process is well described by the TTM (Kaganov 1957). As a validation of our code, and to compare the different methods available, the effect of laser heating in a 50 nm thin film of gold was simulated. In the simulations, the laser energy deposition, is described with a Gaussian temporal profile

$$S = \frac{I_0(1-R)}{L_p} \exp\left[-\frac{z}{L_p} - \frac{(t-t_0)^2}{2\sigma^2}\right] \quad (5.18)$$

where  $I_0$  is the peak intensity,  $R$  is the reflectivity,  $L_p$  is the optical absorption depth, and  $\sigma$  is the standard deviation of the Gaussian profile, related to the pulse duration as  $\tau_L =$  (full width at half maximum)  $= \sigma\sqrt{8\ln(2)}$ . The laser fluence  $F$  is related to the peak intensity  $I_0$  as  $F \approx 1.0645\tau_L I_0$ . The absorbed laser fluence, related to the incident fluence as  $F_{abs} = F(1-R)$ , is used in the discussion of the simulation results in this work. Equation (5.18) describes a laser that has a constant profile in the  $x$ - and  $y$ - directions, so the problem becomes one-dimensional (1D). This assumption is reasonable if the laser wavelength is in the visible light range (Scouler 1967).

The methods described above were compared against a finite element (FE) solution of Eqs. (3.7) and (3.8). The commercial software Comsol Multiphysics ® 3.2b was used for the FE solution. In the MD simulations the order parameter given in Eq. (4.12) was



monitored to make sure that the system remained in the solid state. For the maximum temperatures achieved in the MD simulations, the system exhibited solid-like behavior so that a continuum FE solution is valid. It is noted that in this software the equations are solved considering the spatial variation of the thermal conductivity  $k_l$ . The electronic properties shown in Table 3.1 were considered when solving Eq. (3.7).

A 200 fs laser pulse with absorbed fluence of  $130 \text{ J/m}^2$  and wavelength of 450 nm was considered. At this wavelength, the optical penetration depth,  $L_p$ , in gold is approximately 14 nm (Palik 1985). However, for  $s/p$ -band metals such as gold where the electron-electron collision rate is small, the ballistic motion of the excited electrons can significantly alter the initial energy deposition depth when a laser is applied. Before the excited electrons equilibrate due to collisions with other electrons near the Fermi level and form a Fermi distribution with a certain electron temperature, they can propagate from the optical absorption depth deeper into the bulk of the irradiated sample with velocities close to the Fermi velocity. This ballistic motion of the excited electrons leads to the fast, within  $\sim 100$  fs redistribution of the deposited energy within the ballistic range that is defined by the mean free path of the electrons. It has been suggested that the effect of ballistic electrons can be incorporated into the TTM by substituting the optical penetration depth  $L_p$  in the source term, Eq. (3.7), by an effective laser energy deposition depth defined by both optical absorption and ballistic energy transport,  $L_p + L_b$ , where  $L_b$  is the ballistic range (Wellershoff et al. 1999; Hohlfeld et al. 2000).

As can be seen in Fig. 5.3 the method used by Wang and Xu (2002) and later by Wang (2005) is not accurate for simulations of laser heating during femtosecond pulses. This is because this method assumes a direct energy transfer between the photons and the lattice as described by Eq. (5.8). The rest of the methods yield the same results and their differences are mainly based on their numerical efficiency. The method used by Xu et al. (2004) provides the fastest results because it does not integrate the equations of motion for each atom, but rather re-scales their velocities after the integration has been completed. In the traditional velocity-Verlet algorithm two loops over all the atoms are required to integrate their positions (first loop) and their velocities (second loop).

Because it comes from the same formulation as the method used by Ivanov and Zhigilei (2003) both provide the same results as can be seen from the overlap in Fig. 5.3. Additionally, our assumption of neglecting the spatial variation of  $k_l$  in the finite difference discretization of Eq. (3.7) is validated because the FE solution produces the same results.

It is interesting to note that the relaxation time (the time required for the electronic and atomic systems to equilibrate at the same temperature) is of approximately 20 ps. When the initial temperature rise is high once the laser beam is turned off, the equilibration between electron and lattice temperatures takes a longer time, than in the opposite case. The relaxation time is also a function of the thickness of the film. As reported in the work of Hohlfeld et al. (2000) the relaxation time for a 20 nm film of gold is of approximately 15 ps and decreases to 10 ps for a bulk material. Even though direct comparison to their work may be difficult because of different film thickness and absorbed laser fluence, our results exhibit a similar trend in the relaxation time.

In Fig. 5.4, the temperature evolution of the top and bottom surfaces of 50 nm thin films of gold (Fig. 5.4a) and nickel (Fig. 5.4b) are compared. For the latter thin film an optical penetration depth of 13.5 nm was assumed (Palik 1985) since ballistic electron transport is not significant for nickel (Wellershoff et al. 1999).

The differences in the maximum electron temperature achieved for gold ( $\sim 5000$  K) and nickel ( $\sim 2500$  K) also show an interesting behavior. This is due to the higher electronic heat capacity constant of nickel which is more than 11 times that of gold as seen in Table 3.1. Also, faster electron diffusion in gold causes an almost indistinguishable temperature rise on both the top and lower surfaces, whereas for nickel, there are marked temperature gradients on both the electronic system and the lattice. A faster energy transfer between the hot electrons and the lattice was observed for nickel than for gold due to a stronger electron-phonon coupling for nickel.

With respect to the lattice heat capacity, it was found that using the reported value of  $2.5 \times 10^6 \text{ J/m}^3\text{K}$  (Gray 1972) in the FE solution of Eqs. (3.7) and (3.8) or in the method by Hakkinen and Landman (1993), produced higher lattice temperatures at equilibrium. The mentioned value corresponds to this property evaluated at 273 K. These results are shown in Fig. 5.5.

In previous studies using the TTM for different materials a constant heat capacity evaluated at this temperature has been used (Qiu and Tien 1992; Schafer et al. 2002; Caffrey et al. 2005). In most metals, for applications in which the temperature is large, one can assume a constant lattice heat capacity based on the Dulong and Petite's law considering that the Debye temperature,  $T_D$ , for most metals is small ( $< 200 \text{ K}$ ) and the ratio  $T/T_D \gg 1$ . For the case of gold, however, with  $T_D$  of 165 K (Kittel 1995), assuming a constant heat capacity is in error because the ratio  $T/T_D$  is 1.8. For this ratio, the lattice heat capacity can be approximated by a linear functionality with temperature (at the higher end of the cubic dependence for low temperatures (Ashcroft and Mermin 1976)). It was found that using  $C_l = 8330T_l$  is a much better assumption for simulations of laser heating (Wong and Mengüç 2008). However, there is still the problem of defining this parameter during phase change. To overcome these problems the methods developed by Ivanov and Zhigilei (2003) and Xu et al. (2004) are the most adequate because their formulation is not based on knowledge of the lattice heat capacity. In what follows, Eq. (5.13) is used as the coupling between the TTM and MD.

#### 5.4 Comments

The numerical methods developed in this Chapter provide the basis for realistic computer simulations that are presented later. The use of the hybrid TTM-MD method presented here provides the best alternative to simulate the process of nanomachining by making the least number of assumptions regarding the thermophysical properties of the materials studied. This is a key advantage as the properties required to simulate the process might not be available in the wide range of phases needed.

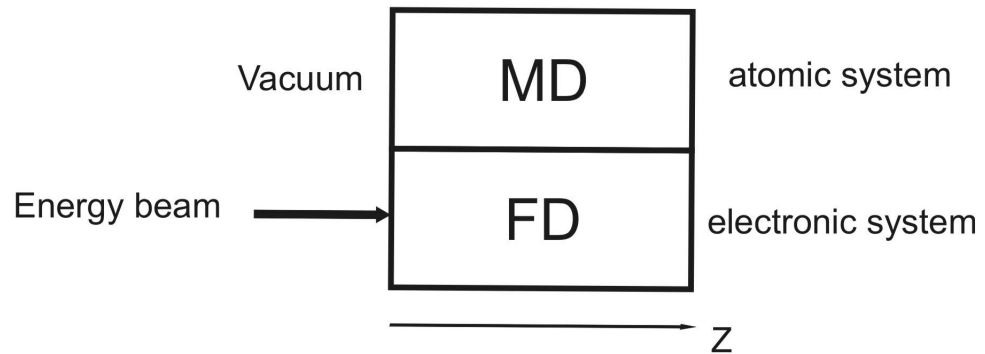


Figure 5.1 Schematic showing the system and our solution scheme. The electronic system is simulated using a finite difference scheme (FD). An energy beam (laser or electron) irradiates the electronic system with normal incidence. The atomic system is treated by a MD scheme. Electronic and atomic systems are coupled by the electron-phonon coupling.

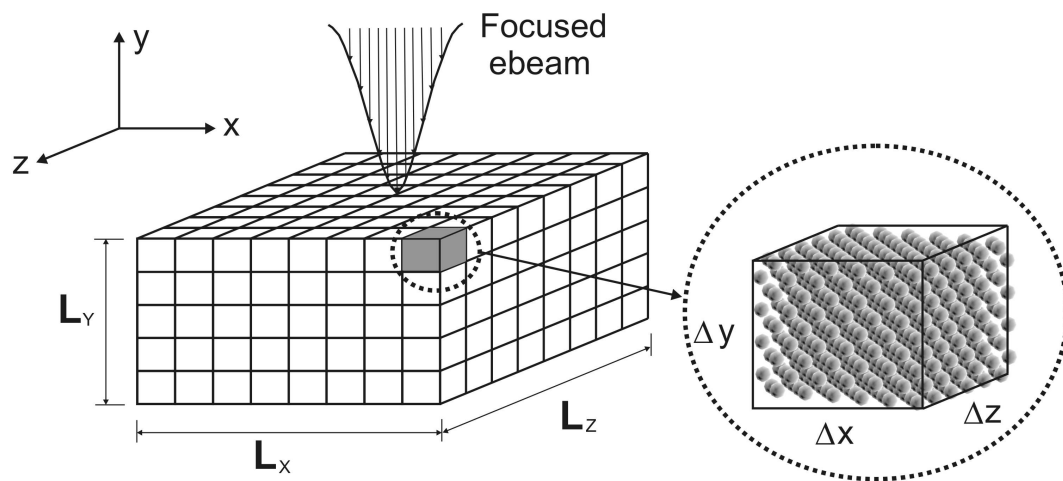


Figure 5.2 Schematic of the hybrid continuum-MD approach. Each discrete element of the continuum model contains initially 109 atoms.

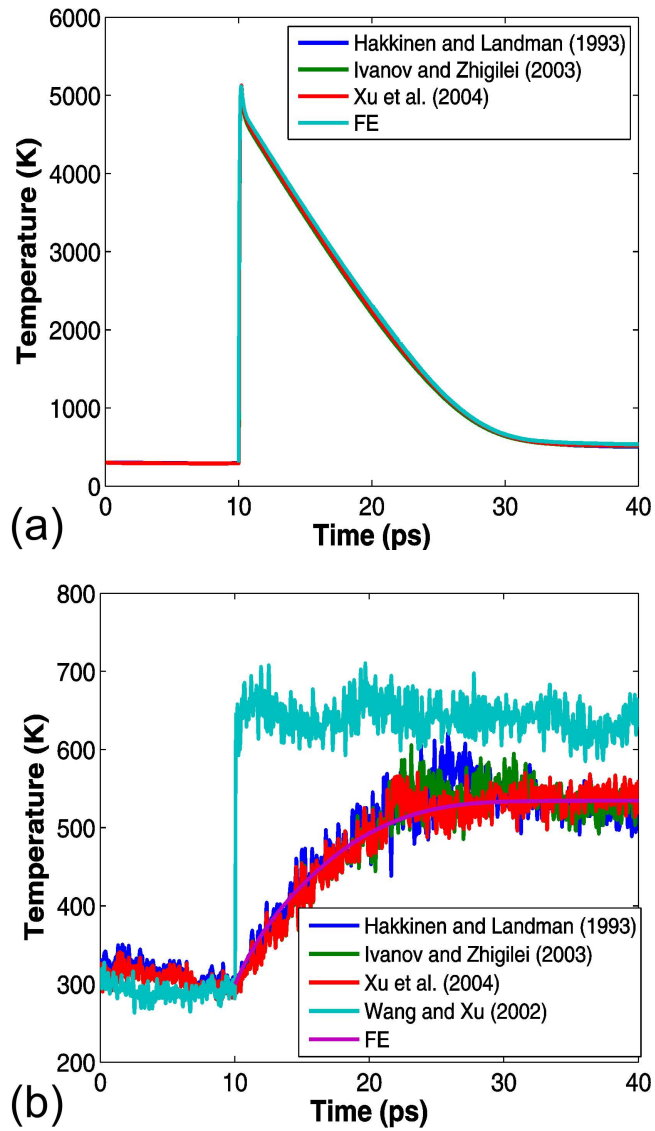


Figure 5.3 Comparison between numerical methods to predict the electron and lattice temperatures for a laser pulse of 200 fs with a fluence of  $130 \text{ J/m}^2$  on a 50 nm thin film of Au: a) electron temperature; b) lattice temperature.

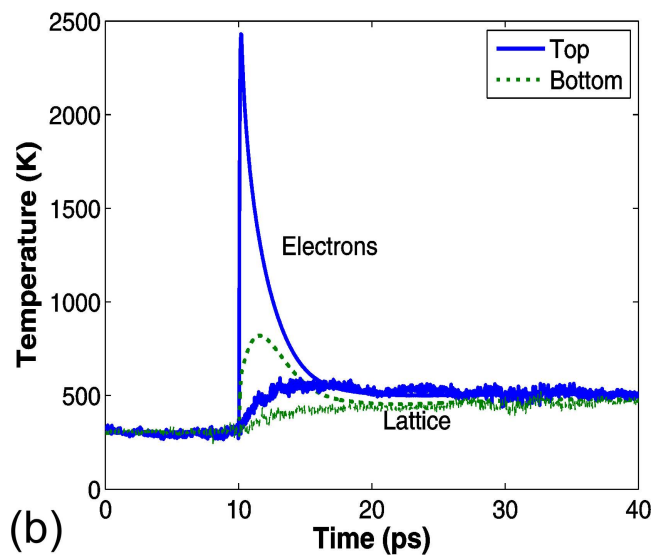
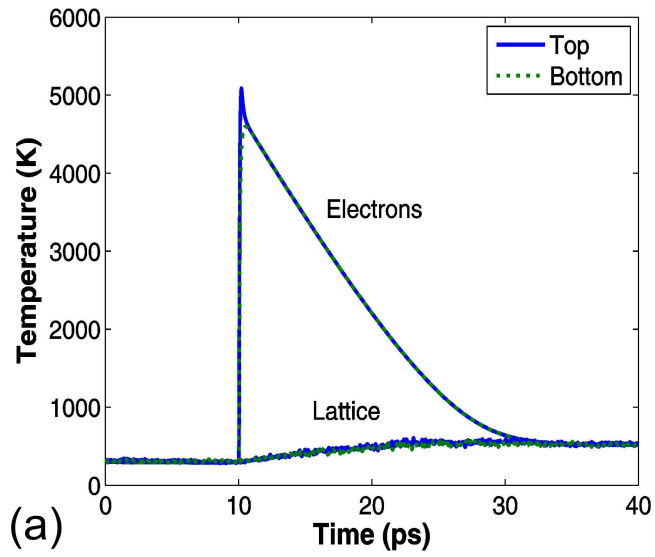


Figure 5.4 Electron and lattice temperature on the top and bottom surfaces of a) gold and b) nickel after laser irradiation with  $130 \text{ J/m}^2$  of absorbed fluence with pulse duration of 200 fs.

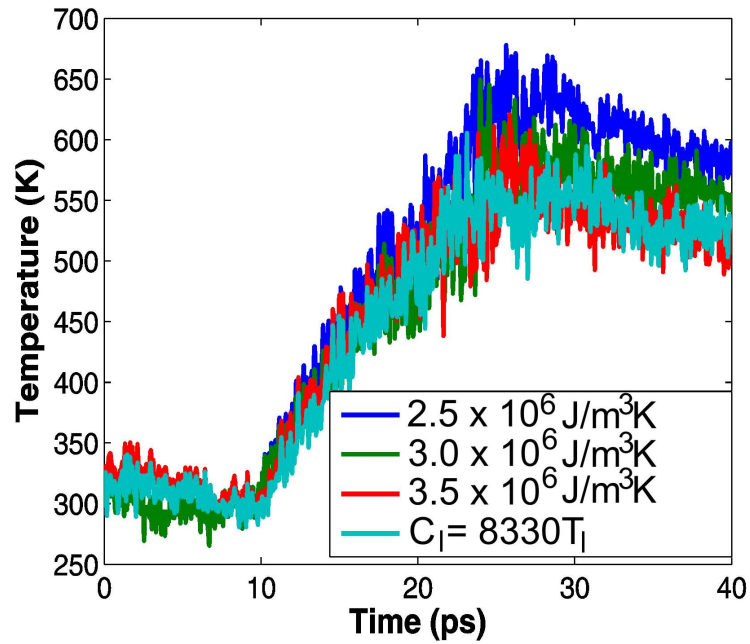


Figure 5.5 Lattice temperature of a 50 nm thin film of gold when heated by a 200 fs laser pulse with an absorbed laser fluence of  $130 \text{ J/m}^2$ . Different lattice heat capacities are compared when using Eq. (5.9) as the coupling between MD and the TTM.



## CHAPTER 6

### 1D SIMULATIONS OF ELECTRON HEATING USING THE HYBRID TTM-MD METHOD

The results from the previous Chapters can now be used to study the effect that the electrons emitted from an array of CNTs has on metallic films. This Chapter makes use of the hybrid numerical method derived in Chapter 5 to study the processes of phase change and material removal, considering a realistic electron emission profile obtained following the methodology described in Chapters 2 and 3.

#### 6.1 Problem settings

The heating effect on thin films of Cu and Ni of an electron beam from an array of CNTs is considered here. Figure 6.1 shows the electron deposition profiles on both materials for emission from a single CNT with 50 nm radius and 4  $\mu\text{m}$  of height. An applied voltage of 300 V and a gap distance of 300 nm are considered.

Even though both elements are fairly similar the differences in the penetration depth in Ni and Cu are quite noticeable, the former being almost half that of the latter. This is due to the differences in the Fermi energy and the work function which are much larger in Ni resulting in a larger energy barrier that hinders electron propagation inside the material.

Following the models and discussions presented in the previous sections, now the electron-beam based heating concept can be tackled and explore the phase change phenomena with a hybrid TTM-MD simulations approach. In a previous study, this concept was explored for a 50 nm thin film of Au (Sanchez and Mengüç 2007). Here, films are considered with 100 nm in thickness. Table 6.1 summarizes the geometric details of the models used.

Periodic boundary conditions are used along the  $x$ - and  $y$ - axes, with the  $z$ - axis representing a free surface (Plimpton 1995). The domain corresponds to a free standing

thin film extending infinitely in the  $x$ - and  $y$ - directions. In practice, thin film heating experiments could be done using a film deposited on a flat substrate, such as a silicon wafer. Our simulations correspond to a case in which the film is supported from the sides and such supports are very far away from the region of interest. The size effects are negligible based on temperature calculations using a box size with dimensions that are twice as large as the ones considered here. Because of the consideration of a heating process that is not varying in the radial direction, the solution corresponds to a one-dimensional (1D) problem. Conduction effects in the  $x$ - and  $y$ - dimensions are not accounted for because of the relatively small size of the simulation box in comparison to the total electron spread ( $\sim 2 \mu\text{m}$ ). It is assumed that the heating occurs uniformly in the entire area where the electron beam is spread, rendering the consideration of conduction in the lateral directions unnecessary for the small region in the center. Also, radiation heat transfer from the heated workpiece to the vacuum is negligible because of the short simulation time (120 ps). However, due to the high temperatures attained (see below) and the close proximity of the CNT emitter array, near field radiation heat transfer effects might be considerable (Francoeur and Mengüç 2008). These effects could pose an additional cooling mechanism for the films, yet the time-scale in which they become important is unclear. Due to the complexity of the near field radiation problem, however, those effects were neglected in this study.

A standard tri-diagonal formulation is used to solve Eq. (3.7) (Kincaid 2002). The FD scheme is discretized spatially with  $\Delta z = 0.3615 \text{ nm}$  for Cu and  $\Delta z = 0.352 \text{ nm}$  for Ni. The effect of increasing the number of CNT on the array (see Fig. 3.4) was analyzed which corresponds to plausible experimental conditions. The simulations are run in parallel computers with 32 processors. In order to account for thermal expansion of the lattice in FD scheme, the number of atoms in each cell is counted during the course of the simulations. The simulations begin with a fixed number of FD cells. However, the atoms can move in and out of the cells during the simulations because of changes in their energy due to the energy deposition by the electron beam. When the number of atoms in a particular region exceeds 10% of the average number density per cell a new FD cell is activated (Schafer et al. 2002; Ivanov and Zhigilei 2003). Also, when the number of

atoms decreases below this limit, the cell is deactivated and the TTM is solved in the active number of cells. Adiabatic boundary conditions are considered when solving the TTM, and the electron energy is not “defined” when material is not present. Numerically, this is implemented by using a ghost-node method (Wong et al. 2004). In the event that a cell between two free surfaces becomes deactivated due to possible ablation of the material, a new adiabatic boundary is created and the TTM is solved for each section of the material once more.

## 6.2 One-dimensional temperature and pressure spatial-temporal profiles

The simulation begins by a 10 ps constant temperature run in which the velocities of the atoms are rescaled to maintain a constant temperature of 300 K. Then a 20 ps constant energy run is performed in which the system is left undisturbed without applying the electron beam. These simulations show that the total energy of the system remains constant during the 20 ps of the simulations indicating that the modified equation of motion, Eq. (5.10), samples the microcanonical ensemble correctly.

The temporal and spatial evolution of the lattice temperature is shown in Fig. 6.2 for an array of 10000 CNT acting on the films. The motion of the top and bottom surfaces of the film corresponds to the thermal expansion. Note that in Fig. 6.2, and in the subsequent figures, the plots correspond to surface plots in 3D that are seen from the top with the height of the surfaces shown in the color bars.

The energy transfer from hot electrons to the lattice leads to an increase in the temperature. In the case of the Cu thin film fast electron diffusion throughout the film causes a rapid rise of the electronic temperature. An order of magnitude analysis based on Eq. (3.7) reveals that the diffusion time for Cu is  $L^2 C_e / k_e \sim 187$  fs while the electron-phonon coupling time is  $C_e / G \sim 3$  ps meaning that at the initial stages of heating the electron temperature rise is fast and uniform. By the time the electrons begin to transfer their energy to the lattice, small electron temperature gradients due to fast diffusion lead an almost uniform temperature rise of the lattice. For Ni, with a large electronic heat capacity, the electronic thermal diffusion is rather small in comparison; therefore, larger

temperature gradients are expected. An order of magnitude analysis leads to diffusion times and electron-phonon times for Ni in the same order of magnitude and approximately 9 ps. This means that before the electrons can diffuse their energy to the bottom of the film, they are already transferring their energy to the lattice resulting in pronounced temperature gradients. This is evident from Fig. 6.2b where for Ni the bottom surface remains relatively cool in comparison to the top. For Cu, as shown in Fig. 6.2a, both sides become hot. This also causes the top surface layers to heat up considerably as the hot electrons cannot easily diffuse into lower parts of the film. Also, the electron-beam penetration depth in Ni is almost half that of Cu further enhancing this effect (see Fig. 6.1).

Examination of the spatial-temporal pressure profiles of Cu and Ni (see Figs. 6.3a and 6.3b respectively) during electron heating reveals an interesting interplay between compression (inwards and keeping the film together) and tension (outwards and pulling the films apart) stress during electron heating. Note that just as in Fig. 6.2 the profiles shown in Fig. 6.3 correspond to the values of the pressure along the depth of the film and plotted for all recorded timesteps. Thus, the rhombus-shaped regions on the plots correspond to the amplitude of a pressure wave as it moves through the film and changes phase from compression to tension when it hits the top and bottom surfaces (Sanchez and Mengüç 2007). These regions appear because the pressure distribution at every timestep is plotted in Fig. 6.3 in parallel axes.

Approximately 5 ps after the electron beam is turned on, the pressure wave that is traveling through the materials starts shifting to a more tensile nature. In the Cu thin film (Fig. 6.3a) a large tensile stress build up is apparent at 40 ps that pushes the top and bottom surface regions apart contributing to thermal expansion of the film. After the film melts at approximately 49 ps (29 ps after the heating begins, see Fig. 6.2a) two regions are observed in the pressure plot: the top region expanding outwards exhibits tensile stress indicating that it continues to expand as it vaporizes; the lower region exhibits compressive stress. Even though tension is usually associated with cooling due to the dissipation of heat into mechanical energy as thermal expansion, the vaporized region

expands while its temperature continues to increase. This is because the top region is comprised of low density vapor which has high kinetic energy. The energy from this region can be dissipated into the vacuum via radiation heat transfer, although radiation losses are not considered. The lower region exhibits compressive stress with a peak at approximately 70 ps. As the heating continues, the magnitudes of these stresses begin to decrease.

In the case of Ni tensile stress mainly builds up close to the top surface, and is followed by the expansion of the surface layers (see Fig. 6.3b). It is interesting to note a compressive stress peaks near the center of the film at approximately 50 ps. This is the point where the solid-liquid melting front speed reaches its maximum after which it decreases and becomes constant (see Fig. 6.7b). The position of the solid-liquid melting front is apparent in this plot. The stresses in the film are mainly tensile with larger magnitudes in the region where the material retains the liquid state.

### 6.3. Structural Changes

Figure 6.4 shows the spatial-temporal profiles of the normalized number density of atoms for both films. These results are plotted to further study the structural change during electron heating. At the early stage of electron heating, the crystal structure is preserved in the target, which is seen as the peak number density of atoms near at each lattice layer. Due to the increase of atomic kinetic energy in electron heating, atoms vibrate more intensely in the solid region, resulting in a lowering of the number density of atoms. As the electron heating progresses, the target is melted, and the atomic distribution becomes random. Two different trends are observed for Cu and Ni. For the former, the energy increase causes that the atomic layers on the surface and below it to become vaporized as they are pushed off the material. For the latter, a region of low temperature is observed being pushed outwards. Vaporization in this case happens below the surface of the workpiece, which reduces the number density of atoms significantly at the location near the liquid surface.

In order to determine the rate of melting and evaporation, additional criteria are needed to discern the solid-liquid and liquid-vapor interfaces. The profile of the number of atoms (Hakkinen and Landman 1993), the radial distribution function (Chokappa et al. 1989), and the order parameter (Morris and Song 2002) are used for this purpose. For solid Cu, the average number density of atoms is  $8.47 \times 10^{28} \text{ m}^{-3}$ , and for Ni it is  $9.17 \times 10^{28} \text{ m}^{-3}$ . In this work, if the number density of atoms is higher than these values, the material is treated as solid. When the material is in the solid state, its normalized number density is unity. In the liquid phase the normalized number density of Cu is less than 0.89 while for Ni is less than 0.87 (Janz 1988; Nasch and Steinemann 1995). At the front of the melted region, the normalized number density of atoms decreases sharply to less than 0.33. Therefore, the material is assumed to be a vapor at a number density lower than a third of the solid-phase number density. The validity of this criterion was studied using the radial distribution function and has been found to be a good approximation (Wang and Xu 2002). In Fig. 6.4 the solid-liquid interface (dotted line) and the liquid-vapor interface (dashed line) based on this approximation were demarked.

The spatial-temporal profile of the order parameter [Eq. (4.12)] and the in-plane radial distribution function for Cu and Ni display marked differences, as shown in Figs. 6.5 and 6.6, respectively.

The Cu thin film is entirely melted just 20 ps after the electron beam is turned on. This is due to the deeper electron penetration inside the film, as well as to the faster electronic diffusion. As the material expands outwards, solidifying plumes are observed (inside the dotted lines) that result from cooling of the ejected material. They can be considered as molten layers close to the solid-liquid transition.

The order parameter is only really useful to establish the solid-liquid interface; the radial distribution function provides additional information on the liquid-to-vapor transition. With the aid of Fig. 6.4 one can establish the position of the liquid-vapor interface. The structural analysis of Ni shows that it retains the solid structure up to the end of the simulation for layers below 50 nm into the film. This behavior is directly

related to the magnitude of the electronic heat capacity, electron-phonon coupling constant and electron penetration inside the film. Much higher values of the properties and much shorter electron penetration correspond to a better retention of the crystallinity, as measured by the order parameter of the material during electron heating and also by shallower melted regions. Lower values and longer penetration correspond to more uniform heating of the material as it was seen for Cu. The radial distribution in Figs. 6.5b and 6.6b further depicts the state of the film at 100 ps of the simulation (80 ps after heating begins). At this point the Cu film is completely melted and vaporized down to 30 nm. Within the same duration, on the other hand, the Ni film retains the solid state at deeper layers.

Using the normalized number density, order parameter and radial distribution function, the instantaneous position of the solid-liquid and liquid-vapor interfaces for the Cu and Ni films was determined. Then, the velocities of these interfaces were determined by finding the derivative of the positions after the latter were fitted with a high order polynomial. As observed in Fig. 6.7 melting and evaporation start at about 25 ps (5 ps after the heating begins). The solid-liquid interface moves into the solid as the melting progresses, and the liquid-vapor interface moves outward as the melted region expands. For the Cu film (see Fig. 6.7a) two melting fronts are actually determined. The films heats up almost uniformly in depth so a melting front from the top and bottom surfaces are obtained. In Fig. 6.7a, only the top melting front is depicted. It can be seen that the solid-liquid interface asymptotes at 49 ps (29 ps after the heating began) which is the point where the two fronts meet and from then on the material is completely melted. The highest velocity of the solid-liquid interface is about 1100 m/s. The liquid-vapor interface shows an interesting behavior as it first moves outwards and then at approximately 70 ps (50 ps after heating begins) it moves inwards indicating that the film begins to vaporize.

In the case of the Ni film (see Fig. 6.7b), the solid-liquid interface reaches a maximum speed of approximately 120 m/s at approximately 40 ps (20 ps after heating begins). Afterwards it begins to decrease and finally reaches a constant speed of 50 m/s indicating that complete meltdown of the film is also possible with prolonged exposure to

the heating source. Unlike Cu however, the melting front moves only from top to bottom surface due to more pronounced temperature gradients in the Ni film. The liquid-vapor interface also moves with increasing speed outwards only to reach a constant speed of approximately 50 m/s (outwards into the vacuum).

Finally, the time required to achieve melting at different depths into the films with different number of CNTs in the array, ranging from 1000 to 1000000 was calculated and shown in Fig. 6.8. The time at which melting occurs was determined by running individual simulations for each point in plots in Fig. 6.8 with different number of CNTs. The order parameter was then calculated using Eq. (4.12) and following the criteria described in Section 6.2, the time required for the order parameter to drop below 0.04 at a given depth as indicated in the figure was determined.

It is clear that as the number of CNTs increases, the time to achieve melting at a given depth decreases since there are more electrons deposited into the materials and thus the total heating power distributed inside the films is larger. For Ni the time required to achieve melting at any depth is almost double that for Cu. The reason for this difference can be explained by the much lower electron diffusion in Ni that results in much larger electronic diffusion time and more pronounced temperature gradients. It can be seen that 10000 CNTs can cause melting of the films at depths of 40 nm at approximately the same time as with a larger number of CNTs. However as the number increases, phase change occurs faster than the time required for thermal expansion to dissipate some of the thermal energy and large pressure build ups contribute to the breakage of the films.

#### 6.4. Comments

The simulations revealed that the behavior of the two materials was considerably different, owing mainly to the faster electronic diffusion in Cu than in Ni. The Cu film melted completely when exposed to the electron beams from 10000 CNTs and exhibited two melting fronts which converge close of the middle of the film with a very large velocity. This was followed by large thermal expansion and vaporization of the top layers of the film. In the case of Ni large temperature gradients were observed.



It was found that the phase change process in thin films is an interplay between the speed of the energy diffusion into the films and a concentration of tensile stresses that contribute to expansion and breakage of the films. A material such as Cu with fast electron diffusion tends to heat up and melt more uniformly than Ni for which the energy diffusion is slower. Large tensile stresses appear in both cases contributing to thermal expansion, but due to a better retention of the crystalline phase in Ni, liquid regions of the film are pushed outwards from the solid-liquid interface.

Table 6.1  
Domain size used in the simulations

Metal	Lateral box size (nm x nm)	Atoms per layer	Number of atoms
Cu	5.784 x 5.784	1024	284160
Ni	5.632 x 5.632	1024	292352

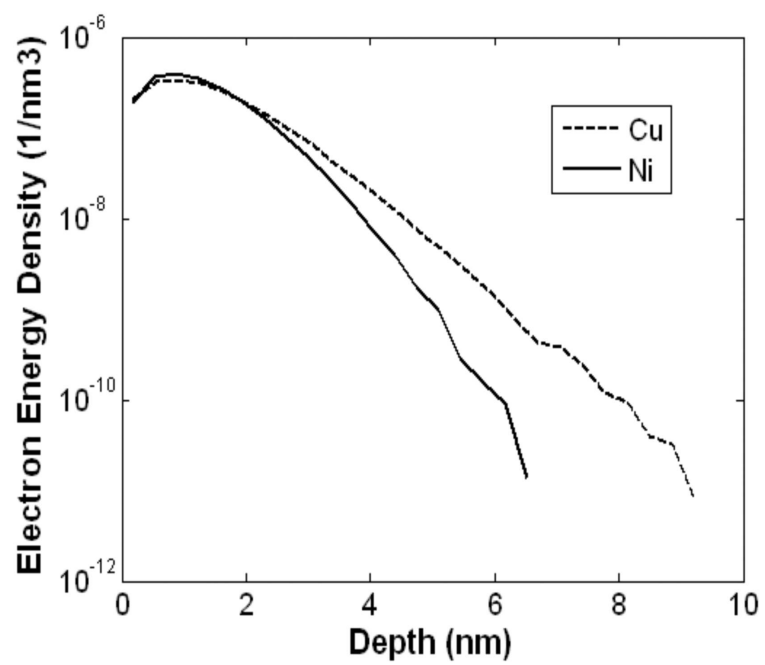


Figure 6.1 Electron energy density for Ni and Cu as a function of the depth in the film

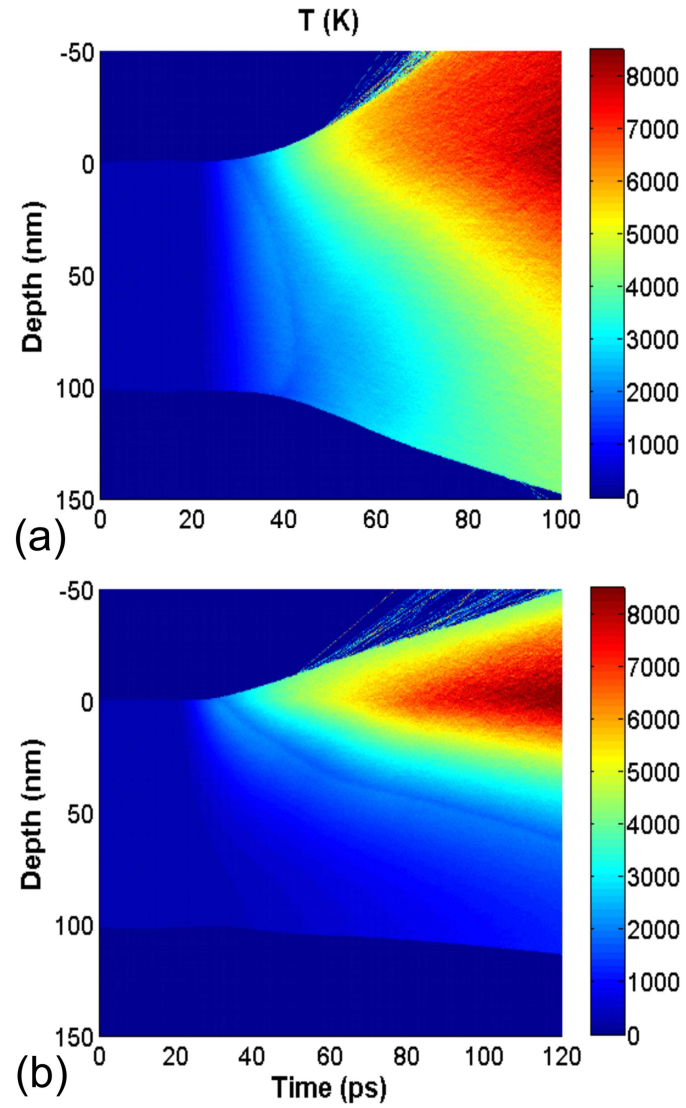


Figure 6.2 Transient lattice temperature profiles during heating of a 100 nm thin film by an array of 10000 CNTs with 300 V of applied voltage and 300 nm gap distance. a) Cu film; b) Ni film.

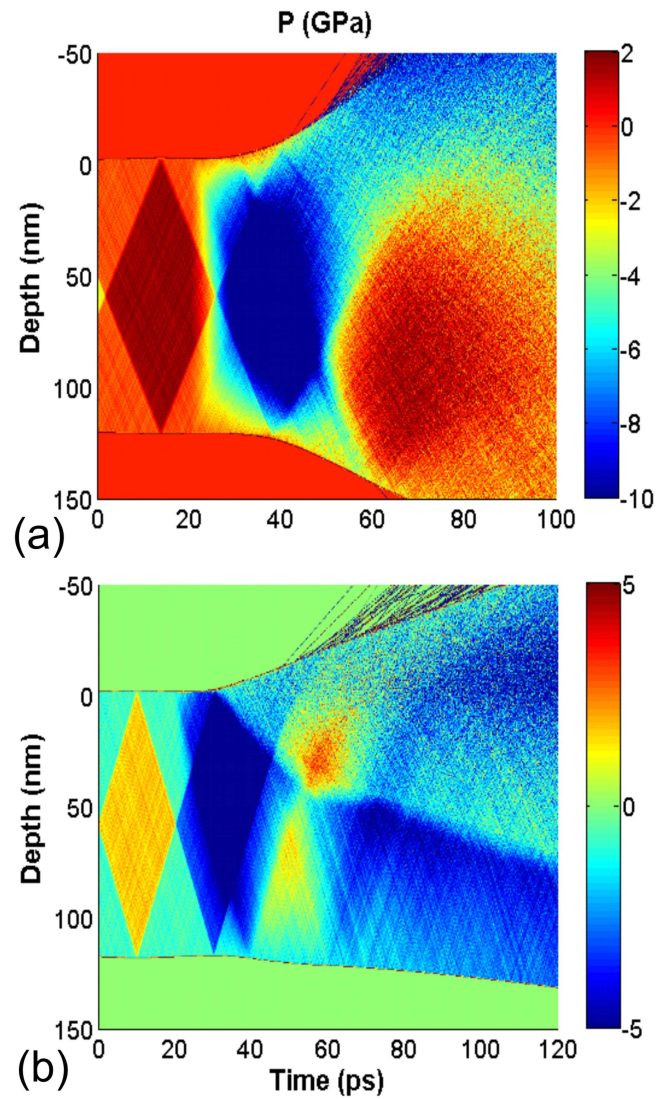


Figure 6.3 Transient pressure profiles during heating of a 100 nm thin film by an array of 10000 CNTs with 300 V of applied voltage and 300 nm gap distance. a) Cu; b) Ni. Positive values denote compression, negative values denote tension.

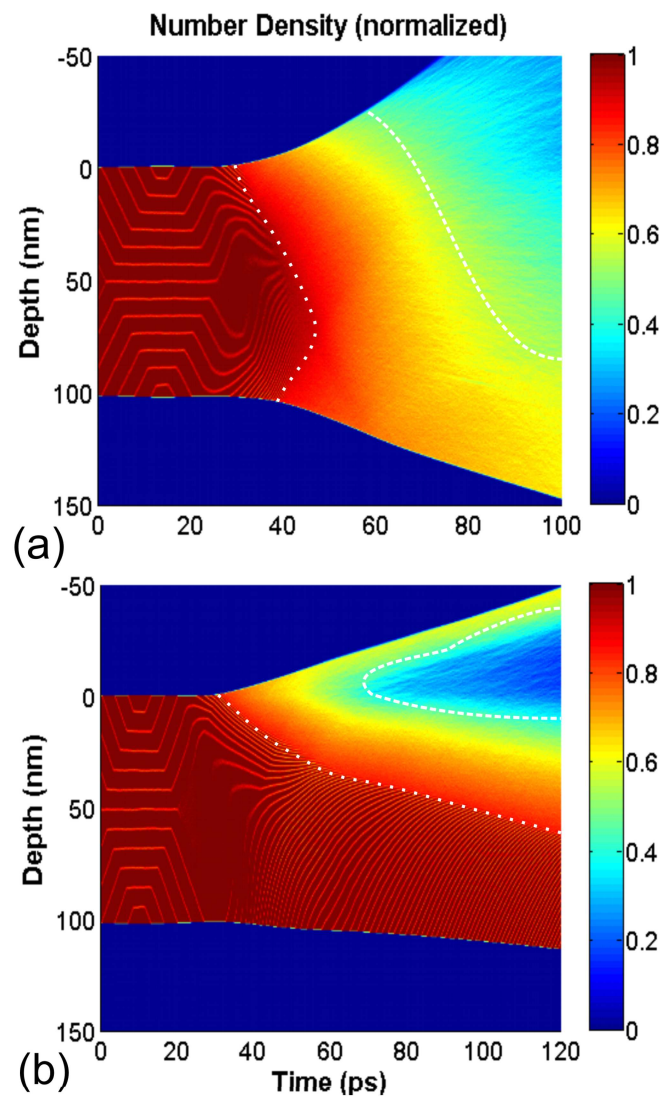


Figure 6.4 Spatial-temporal profile of the normalized number density of the films during heating by an array of 10000 CNTs with 300 V of applied voltage and 300 nm gap distance. a) Cu film; b) Ni film. The dotted line delineates the solid-liquid interface and the dashed line the liquid-vapor interface.

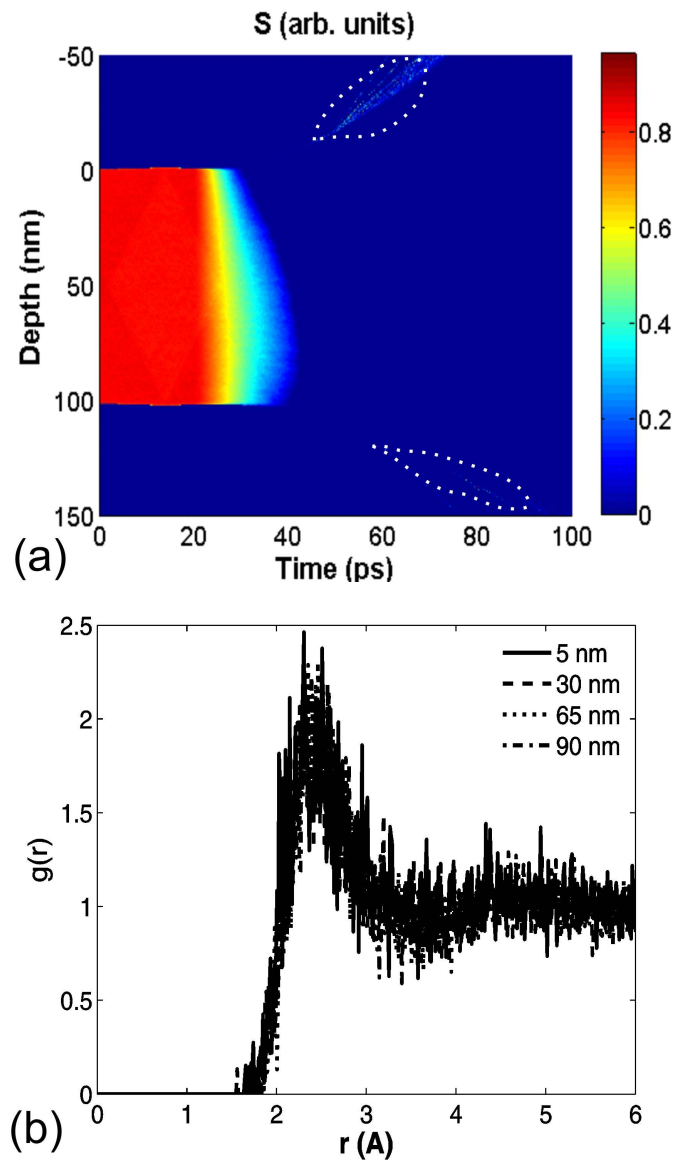


Figure 6.5 Structural analysis of the Cu film during the heating of field-emission by an array of 10000 CNTs with an applied voltage of 300 V and 300 nm gap distance. a) Order parameter and b) in-plane radial distribution function at 100 ps at various depths.

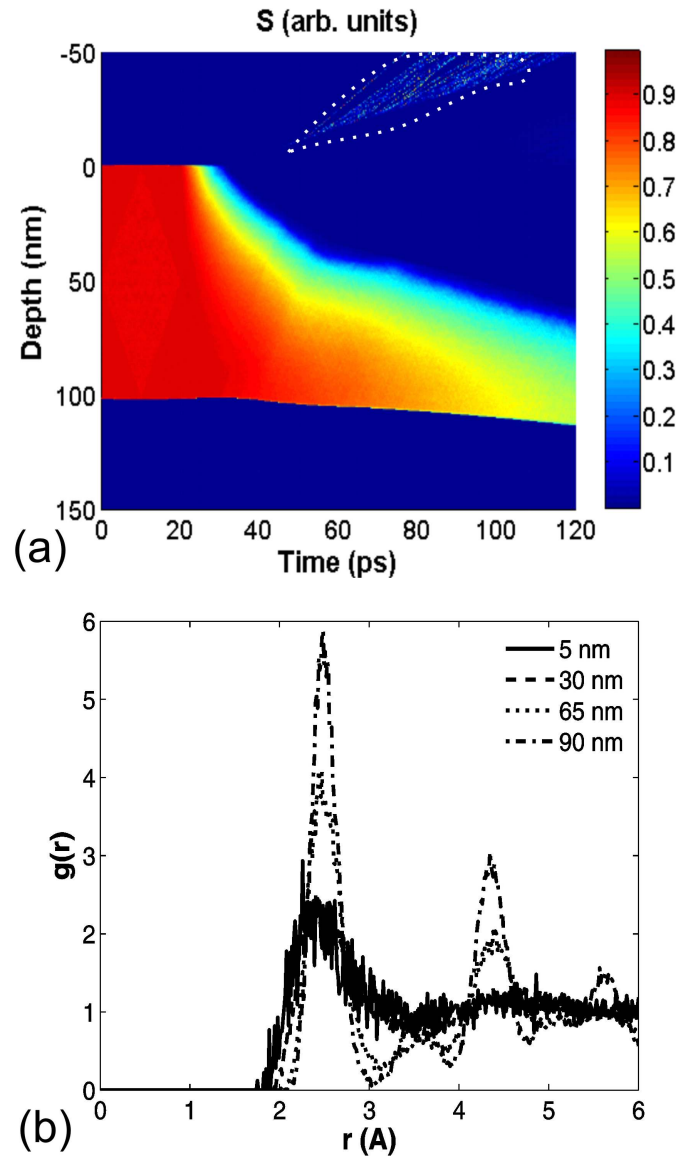


Figure 6.6 Structural analysis of the Ni film during the heating of field-emission by an array of 10000 CNTs with an applied voltage of 300 V and 300 nm gap distance. a) Order parameter and b) radial distribution function at 100 ps at various depths.



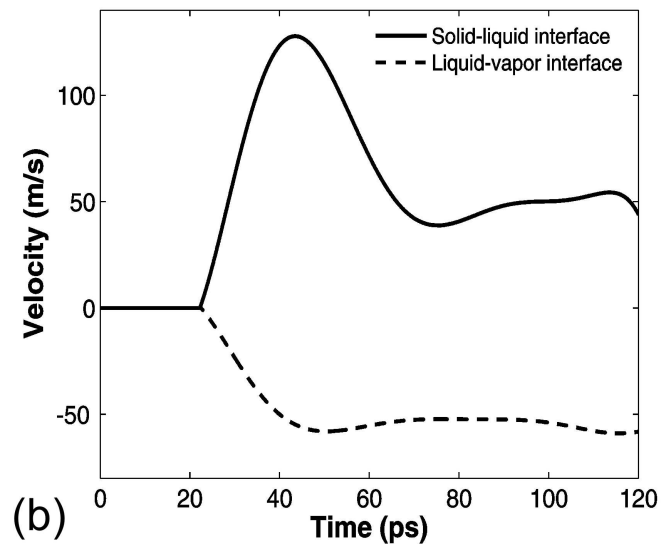
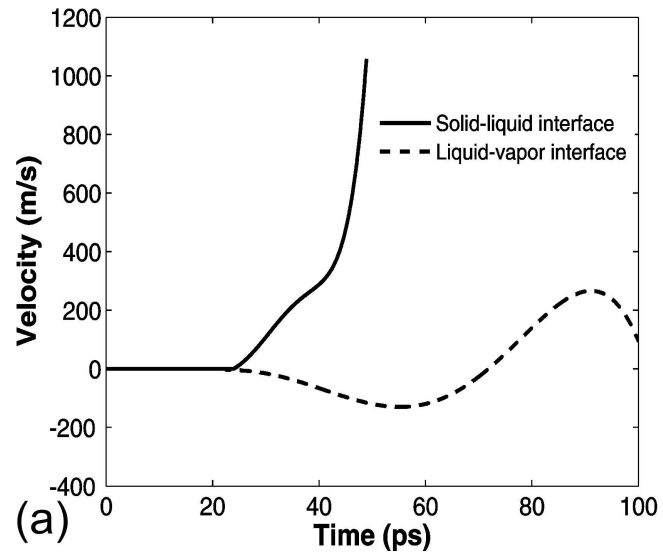


Figure 6.7 Velocities of the solid-liquid and liquid-vapor interface in a) Cu and b) Ni, after heating with 10000 CNT with 300 V and 300 nm of separation distance.

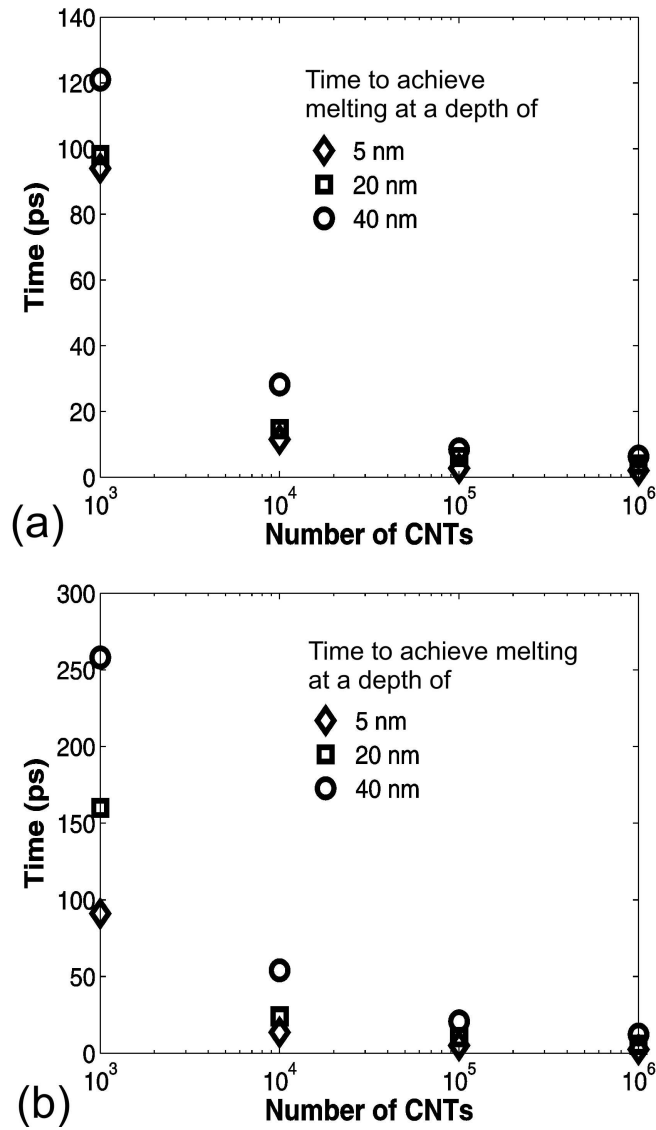


Figure 6.8 Time required to achieve melting at a given depth of a thin film as a function of the number of CNTs used for electron emission: a) Cu, b) Ni.

## CHAPTER 7

### NANOMACHINING OF METALLIC SURFACES USING A HIGHLY FOCALIZED ELECTRON BEAM

In this Chapter, the experimental conditions required, such as the accelerating voltage and heating power, to achieve nanomachining of a metallic surface are explored using a highly focused electron-beam. The focusing mechanisms are of no concern at this point, but concentrate mainly on exploring the thermal aspects of nanomachining once the electron-beam hits the surface. The hybrid numerical approach developed in Chapter 5 is used that combines the two-temperature model (TTM) and molecular dynamics (MD) to study the mechanisms of phase change and material removal in precise detail. This Chapter deals with the expansion of concepts outlined in earlier work (Sanchez and Mengüç 2007, 2008c) to consider a 3D scenario where the radial component is not neglected. Two different materials are considered (Au and Ni) in the simulations as their electronic and thermophysical properties are readily available in the literature. Finally, the hybrid numerical approach developed here is used to explore the temporal and spatial aspects of nanomachining processes.

#### 7.1 Problem settings

Nanomachining of a metallic surface using a highly focalized electron beam is now investigated (see Fig. 5.2) (Sanchez et al. 2008b). Two workpieces of Au and Ni surfaces as their properties are readily available. In Fig. 7.1 the electron energy density deposition profiles are shown as a function of the depth inside the materials for various accelerating voltages. As the accelerating voltage increases, so does maximum penetration depth of the electron beam; however, the density of the electrons along the depth decreases as they become more distributed inside the materials. The same is true along the radial direction. Note that here the term “maximum penetration depth” is used to refer to the point where the electron energy density approaches to zero (Sanchez and Mengüç 2007). It can be seen from Fig. 7.1 that even though both materials are essentially different, the resulting electron deposition profiles are almost identical.

In the simulations of nanomachining presented in Section 7.3 a heating power is associated to each accelerating voltage assuming a given value of current. For instance, a heating power of 1 W for an accelerating voltage of 0.25 keV corresponds to a current of 4 Amps. The resulting electron deposition profiles are then used as a heat source in the hybrid numerical method discussed below. The discussion of feasibility of achieving such a highly focalized and energetic electron beam is left to the next Chapter.

## 7.2 Numerical model settings

The coupling between the continuum electron equation [Eq. (3.7)] and the discrete equations of motion [Eq. (4.5), with the explicit velocity rescaling Eqs., (5.6) and (5.13)] is achieved via a hybrid approach (see Chapter 5). The simulations begin by dividing a continuum domain with volume  $L_x L_y L_z$  into grid elements of volume  $\Delta x \Delta y \Delta z$ . Grid elements of length as  $\Delta x = \Delta y = \Delta z = 3a_0$  are chosen where  $a_0 = 0.408$  nm and  $a_0 = 0.3615$  nm is the lattice constant of Au and Ni respectively. A schematic of this model is shown in Fig. 5.2. Inside each discrete element shown in Fig. 5.2 there are 109 atoms.

As the simulation of nanomachining is performed, the number of atoms in each element changes due to their atomic motion. The model in Fig. 5.2 represents a free standing thin film. Thermal expansion is a natural consequence of solving the equations of motion because at each time step the position of each individual atom can be determined. To account for thermal expansion new elements on the  $y$ - axis are activated if the number of atoms in a particular point in space, defined with the same dimensions of a discrete element, exceed 10% of the initial number of atoms in a regular element. However, in the event that the number of atoms in a region is less than this limit, the element is deactivated. Here, the implicit discretization given in Section 5.4.2 is used in order to solve Eq. (3.7).

## 7.3 Continuum calculations with the TTM

Before performing the simulations of nanomachining with the hybrid TTM-MD method discussed in the Section 5.1, one needs to have a feeling of the behavior of the materials when exposed to the electron beam. Thus, as a first approximation, and to

explore the effects of heat diffusion through Au and Ni when exposed to an electron beam with a given accelerating voltage and heating power, Eqs. (3.7) and (3.8) are solved using a finite difference scheme [Eqs. (5.14)-(5.17)]. Note that these equations are solved as they are without additional considerations of phase change and moving boundaries due to thermal expansion (Szyszko 1995; Pronko 1996).

In achieving different nanomachining scenarios, the potential combinations of accelerating voltage and heating power are virtually infinite. Here, the details of the feasibility of achieving a prescribed heating power of the electrons are not given, as they were discussed earlier in (Sanchez and Mengüç 2008b). The modeling is based in the possibility of producing a very large temperature gradient in a radius of approximately 10 nm from the center of the workpiece. Obtaining pronounced temperature gradients within the workpiece is crucial because electron-based nanomachining is purely a thermal process in which highly focalized, high energy electrons heat the material to the point where atoms in a given region are ejected, thus producing a nano-sized indentation on a surface. Additional questions can be raised at this point, such as what is the final position of the atoms that are “ejected” and what are the governing physics of the process that can lead to it being repeatable and controllable in an industrial environment. The expectation is that these questions can be addressed with the use of the hybrid TTM-MD discussed above.

Au and Ni films with dimensions of 100 x 25 x 100 nm are simulated. The solution of Eqs. (3.7) and (3.8) are shown for a variety of accelerating voltages and heating powers. For each accelerating voltage, heating powers of 0.5 W, 1 W and 10 W were considered.

For the case of Ni (left column, Figs. 7.2a and 7.2c) the results correspond to the temperature profile on the material at the time when a point located at the center of the top surface reaches the prescribed boiling point. At that time, the simulation was stopped. Because in this simple model the effects of the latent heat of fusion, vaporization or thermal expansion are not considered, the temperature gradients depicted in the Fig. 3 might not be as pronounced given that the two phase change processes take place at

constant temperature. In the work of Wong et al. (2004) the latent heat of fusion effect was considered on gold and the result was a more distributed high temperature region. Thermal expansion in turn is a process that tends to cool the material (Sanchez and Mengüç 2007, 2008c). For the case of Ni, however, it is expected that even when the phase change processes take place pronounced temperature gradients remain as this material has a very low electron diffusivity, which in turn results in a longer time for the energy of the electron beam to diffuse into the material. The results in Figs. 7.2a and 7.2c indicate that within a radius of 10 nm from the center of the top surface a nano-indentation might be achievable on Ni, especially for the case of the lowest voltage and lowest heating power. From Fig. 7.2c it can be seen that the effect of higher voltage produces a deeper distribution of a high temperature region into the film, creating a potential scenario in which a hole is “burned” through the film. Here, one is interested in the possibility of removing a certain amount of material from a surface without cutting through it.

Even though for the accelerating voltages below 1 keV the temperature profile looks similar for both materials, the behavior at 5 keV is significantly different. As the accelerating voltage increases, the electrons penetrate deeper into the material and become more diluted. For a given heating power, this means that it takes more time for given part of the material to achieve a certain temperature before the energy diffuses into deeper regions.

The results for Au (right column, Figs. 7.2b and 7.2d) show that the high temperature region extends well beyond 10 nm at the time the boiling point is reached. As for the case of Ni, the heating effect of an electron-beam with different accelerating voltages and heating powers focused to 2 nm on the surface was considered. In reality, one would expect that the temperature distribution is much more uniform during the phase change processes. The case for 5 keV (Figs. 7.2b and 7.2d bottom right) is interesting because it shows the material heating almost uniformly both the in the radial and axial directions. The results for Au contrast those of Ni in such a large degree owing to the much faster electron heat diffusion of the former (Sanchez and Mengüç 2007).

#### 7.4 Nanostructure formation

With the results of the previous section, the hybrid TTM-MD simulations are carried considering Ni as the workpiece under the influence of a highly focused electron beam with an accelerating voltage of 250 V and heating power of 0.5 W. Equation (3.7) is used to represent the electronic system, which is discretized following Eqs. (5.14)-(5.17). The simulations begin with 98000 elements:  $N_x = N_z = 70$ ,  $N_y = 20$  where  $N_\alpha$  is the number of elements in direction  $\alpha$ . This corresponds to a film of 73.92 x 21.12 x 73.92 nm. Inside each discrete element of the continuum domain, the MD domain is initially defined with 109 atoms per element, with a total 10682000 atoms. A parallel algorithm was used to integrate the equations of motion with the required re-scaling to account for the electron-phonon coupling [Eqs. (5.6) and (5.13)]. A cluster of 256 processors is used in the simulations shown below, arranged in a grid of 8 x 4 x 8 which gave the most efficient computation results (Plimpton 1995).

Since atoms can move freely throughout the domain, additional discrete cells are activated when the number of atoms in a particular region of space exceeds 10% of the average number of atoms in a regular cell (Sanchez and Mengüç 2007). Periodic boundary conditions are applied in the  $x$ - and  $z$ - directions. Thus, only along the  $y$ -direction are the additional cells activated or deactivated to compensate for thermal expansion. In general terms, the extent of the lateral dimensions should be such that, far away from the center of the electron beam, the expected temperature rise is small or negligible. This is expected for the case of Ni for the energy of the electron beam considered (see Fig. 7.2a).

The simulation begins by a 10 ps constant temperature run in which the velocities of the atoms are rescaled to maintain a constant temperature of 300 K. Then a 10 ps constant energy run is performed in which the system is left undisturbed without applying the electron beam. These simulations showed that the total energy of the system remained constant during the 10 ps of the simulations indicating that the equation of motion, Eq. (4.5), with the explicit velocity rescaling [Eqs., (5.6) and (5.13)] samples the

microcanonical ensemble correctly. At this time,  $t = 10$  ps, the electron beam is turned on.

Figure 7.3 shows snapshots of the atomic positions at various times in the simulation. The region depicted corresponds to the  $x$ - $y$  plane 0.352 nm thick centered at  $z = 0$ . This gives a visual guide of the process of nanomachining. In these plots each dot corresponds to an atom. The electron-beam was fired at  $t = 0$ . Already at 0.7 ps a region in the center of the film exhibits a lighter color in comparison with the rest of the material, because atoms have more energy to move in and out of the plane depicted in the snapshot. It is also an indication that atoms are more “diluted” in that region, indicating that the material has started to change phase.

As the electron-beam heats the surface the energy of the atoms increases, and the pressure resulting from their collective motion pushes the region outwards. At 0.95 ps, the electron-beam is turned off, and the heated spot can be characterized as a super heated vapor. As the pressure below the surface has built up, an explosion of material is observed and clusters of atoms are ejected outwards leaving a “crater” on the surface. Towards the end of the simulation, at 20 ps, the material has re-solidified leaving a well defined nano-hole that has a radius of approximately 4 nm and a depth of 2 nm.

The phase transitions mentioned in the discussion of Fig. 7.3 are characterized through the use of an order parameter and a radial distribution function (RDF) (Sanchez and Mengüç 2007, 2008c). Both of these methods use structural information based on the original atomic positions, before the electron-beam heats the surface, and compares it with their time dependent trajectories. In a very rigorous sense they do not explain the reasons behind phase transitions, but can be used to characterize them. Given that they are based on averages that require a certain number of atoms, there is the problem of identifying the number of atoms required to produce statistically sound results. The cell size considered with 109 atoms seems to be adequate as the calculations based on both the order parameter and the RDF give results that correspond to what is observed from



directly visualizing the atomic trajectories. Additional problems in the temperature calculations are discussed later.

The results of the time-dependent order parameter are shown in Fig. 7.4. Already at 0.1 ps of heating, the crystallinity of a nanometer-sized region below the surfaces begins to decrease. By the time of 1 ps after the heating started, a melted region is apparent on the surface with a radius and depth of approximately 5 nm. It was found that at this time the magnitude of the order parameter inside this “hole” is zero. Given that the order parameter is only useful to characterize solid-to-liquid phase transitions it mainly serves to characterize the onset of melting, and also to establish the position of the melting front as a function of time. The material is usually considered as a liquid when the magnitude of the order parameter drops below 0.04 (Morris and Song 2002). It is interesting to note, however, that as the material cools down, the regions close to the borders of the nano-hole begin to re-solidify, and by the end of the simulation a clearly distinguishable hole of 4 nm in radius and approximately 2 nm in depth appears with solid walls. A similar behavior was observed elsewhere (Wang and Lu 2005). Comparing Fig. 7.3 and 7.4 at  $t = 2$  ps, it is clear that there is some material ejected outwards. However, the phase of those “droplets” was not calculated using the order parameter, because each of those regions was comprised of less than 10 atoms. An interesting question arises as to how one can define phase for such a small number of atoms.

The RDF is shown in Fig. 7.5 calculated as a function of time in four locations on the workpiece. All of these locations were considered in the  $x$ - $y$  plane for the positions indicated in the figure at  $z = 0$ . Four locations were chosen: one at the very center of the workpiece, and the other three located at a radius of 10 nm away from this center spot. Unlike the order parameter, the RDF can be used effectively to characterize both solid-to-liquid and liquid-to-vapor phase transitions as it calculates the number density of atoms starting from a center atom and compares it to the number density of a vapor (Haile 1992). Thus, if the material is in the vapor phase the RDF tends to unity. It is observed that effectively, the material remains in the solid phase at points located on a radius of 10 nm away from the center. At 1 ps, the center spot exhibits a vapor-like behavior as

expected from the atomic trajectories in Fig. 7.2. There is no need to show the RDF for latter times, as the region in the center is ejected, and it was found that the other points depicted in Fig. 7.5 exhibit solid-like behavior.

With the use of the information shown in Fig. 7.4 the position of the solid-liquid interface during the process can be tracked. This is done by determining the depth at which the order parameter drops below 0.04 as a function of time. The results are shown in Fig. 7.6.

For clarity, in Fig. 7.6a a polynomial of 4<sup>th</sup> order was used to fit the data of the positions of the interface (Wang and Lu 2005). Already at 0.4 ps there is a molten region that moves into the film and reaches a maximum depth at 1 ps. Afterwards, and as the material cools down, the material re-solidifies and the interface recedes outwards. The speed of the melting front of a point located at the center of the workpiece (Fig. 7.6b) was calculated by dividing the distance traveled by the time duration of the given interval (inset of Fig. 7.6b). It is observed that the acceleration of the interface into the material is extremely fast, with a maximum speed of 10000 m/s at 1 ps. It has been established, however, that the maximum velocity of the melting front is limited by the speed of sound, so the validity of these results needs to be evaluated (Rethfeld et al. 2002a). This is the point when the material inside the hole exhibits the behavior of a superheated vapor. As the process continues, the material is ejected, leaving behind a hot zone. The interface then stops moving, and recedes outwards with a constant rate of approximately 70 m/s, much slower than the propagation inwards of the melting front. At the end of the simulation, there is a hole with solid walls and of course there is no longer a moving interface. From these simulations, it can be estimated that a total of 2305 atoms Ni were removed from the surface, which corresponds to approximately 100.53 nm<sup>3</sup> of material or  $1.34 \times 10^{-22}$  kg at a rate of  $6.7 \times 10^{-12}$  kg/s.

## 7.5 Pressure and temperature profiles

The previous discussions show that as the heating takes place material inside a 4 nm region on the surface is ejected outwards. Insight on the reasons behind this behavior can

be investigated by calculating the pressure of the system through the virial which gives the total pressure exerted on an atom due to the interactions with its neighbors (Haile 1992). Here, the average per-atom pressure was calculated on a cell of 1.056 nm in size. Tensile stress thus negative and compression is positive. The results are shown in Fig. 7.7.

Only a few snapshots of the pressure distribution are shown in Fig. 7.7 for clarity, given that the color bars change dramatically as the tensile stresses increase. The main feature of these results is that a large tensile stress builds up underneath the surface. At 1 ps, the material has already started to expand and the pressure has a magnitude of approximately 120 GPa, almost a thousand times larger than the ultimate strength of Ni (Howatson 1992). This large pressure rise happens when the material is heated faster than the time it takes for thermal expansion to relax the energy of the system. Thus, by the time the material begins to expand the pressure is large enough to produce a phase explosion and a region of superheated vapor is ejected outwards. This process is referred to as stress confinement and has been studied extensively in the past for lasers (Zhigilei and Garrison 1999, 2000). The same trends are observed here.

It can be noted that the regions that exhibit these large tensile stresses, also correspond to the regions where the material is diluted, meaning that there are fewer number of atoms in a discrete region with which to take an average. This may result in numerical errors that could affect the actual magnitude of the stress. It becomes more and more difficult, however, to use definitions such as the virial when the number of atoms is very low, as in this case. Even with these considerations, it can be expected that the trends observed here remain the same.

Once the super heated region is ejected, the magnitude of the tensile stress reduces significantly. Additionally, it is observed that when the ejection takes place, a pressure wave travels through the film from the separation region towards deeper parts of the film. The propagation of this wave is evident from the pressure profiles at 1.6 and 2 ps. This wave propagates through the film from the top surface towards the bottom. It is then

reflected back and changes phase at the boundaries from tension to compression. This phenomenon was also observed in another simulation involving heating of an Ar thin film (Wang 2005; Wang and Lu 2005).

Finally, the temperature of the system is calculated. Thus far, the regions referred to as “hot spots” have been labeled so based on the results from the order parameter and RDF, where the presence of the liquid or vapor phase was determined. In Fig. 7.8 the temperature distribution in the workpiece is shown for various times calculated using Eq. (4.10). As in the case of Fig. 7.7, only a few snapshots are shown due to the large changes in the color bars for each time.

First, it is noted that there exist large temperature gradients, along the lateral and axial dimensions. This means that in a real experiment where the thin film could be placed on top of another substrate the results presented here are still valid, since the effect of heat conduction can be neglected.

As the nanomachining process takes place, the energy from the electron beam deposited inside the material is transferred to the lattice via the electron-phonon coupling. The electron energy is converted into kinetic energy of the atoms that comprise the lattice, producing large vibrations of their trajectories. Since the heating rate is faster than the time required for diffusion to transfer energy into deeper parts of the material, the kinetic energy of just a few number of atoms in a small region increases rapidly and by a large amount. Numerically, this directly affects the virial and thus the calculated pressure (Haile 1992). It can also be seen that even with the fast temperature rise exhibited in Fig. 7.8, the process of thermalization (time required for electrons in the electron-beam to reach equilibrium with the free electrons in the metal) still occurs much faster than the actual temperature rise (Rethfeld et al. 2002b).

At the time the material begins to expand at 1 ps, the calculated temperature of the system is approximately 50000 K at the highest point which corresponds to  $k_B T = 4.31$  eV. This energy is in the order of the ionization energy of metals (Ashcroft and Mermin

1976). Additional consideration for the effect of ionization of the atoms was not done here, but it is expected that it does not affect the results considerably. This omission would create a problem only if the electron source (negatively charged) is placed close to the surface of the workpiece as the ionized atoms (positively charged) would accelerate towards the electron gun and could potentially cause some damage. As for the calculations of the pressure, the potential for error in calculating the temperature of a very small number of atoms is noted, as the temperature seemed to be higher when the number of atoms was small. The trend observed here is likely to be correct, but the magnitude of the temperature values, especially for the ejected region, might be larger due to large kinetic energies of individual atoms.

A very rapid decrease in temperature soon follows and already at 2 ps the temperature of the hottest spot is in the order of 7000 K. Equation (4.10) was used here to calculate the temperature of the ejected regions because the droplets shown in Fig. 7.3 are comprised of only a few atoms, which do not provide a meaningful statistical averaging. At 10 ps into the simulation, the affected region has cooled down considerably and is below the melting point of Ni (1726 K). Finally by the end of the simulation the system has cooled down considerably due to heat diffusion to deeper parts of the film, as other energy loss mechanisms, such as radiation, were not considered.

## 7.6 Comments

In this Chapter the process of nanomachining on metallic surfaces under the influence of a highly focalized electron-beam was studied. A hybrid numerical approach that combines the continuum two-temperature model and the discrete molecular dynamics was used to simulate the process. First, the continuum two-temperature model was applied to establish the potential combinations of voltage and heating power that could lead to a large temperature gradient in a 10 nm region. It was found that this is achievable in Ni surfaces, and in general, in materials with low electron diffusivity. The continuum predictions showed that materials with low electron diffusivity lead to fast temperature rise. Then, the hybrid numerical approach was applied to Ni. Through the molecular dynamics simulations, it was found that due to the large energy concentration on a small

region on the workpiece, tensile stresses build up. These ultimately exceed the mechanical resistance of the material and a phase explosion occurs which leads to material ejection. Through an order parameter and a radial distribution function, it was established the phase of the workpiece during the process. It was also found that before material was ejected, the heated region corresponded to super heated vapor. After the phase explosion, the material cools rapidly, in less than 20 ps.

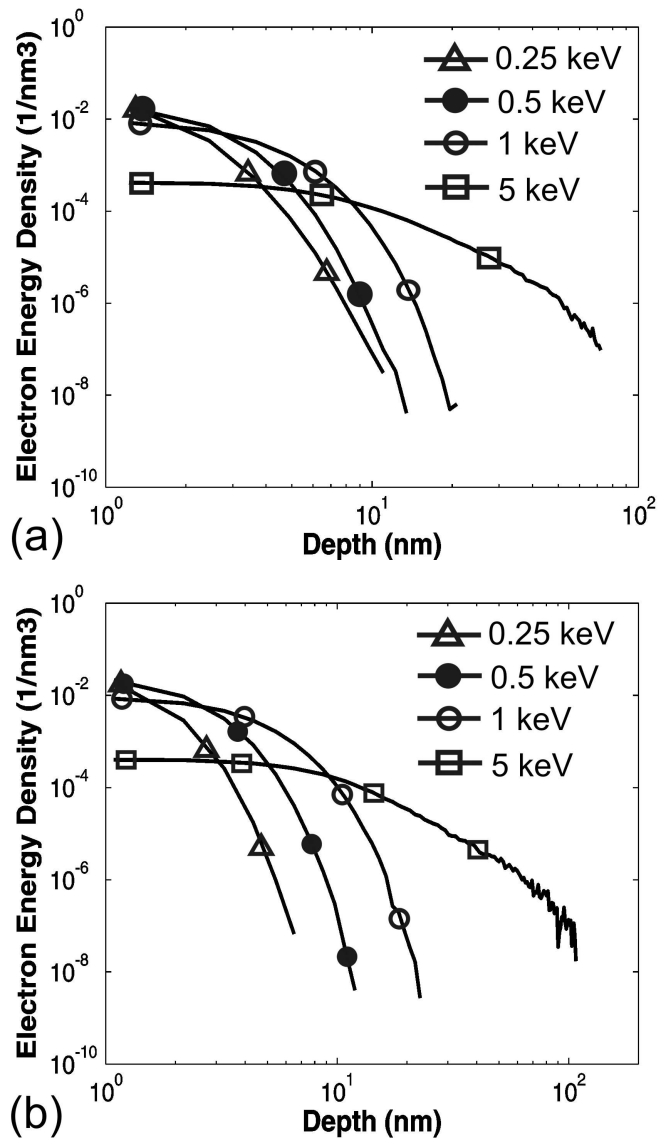


Figure 7.1 Electron energy density as a function of the applied voltage based on MCM simulations a) Au; b) Ni

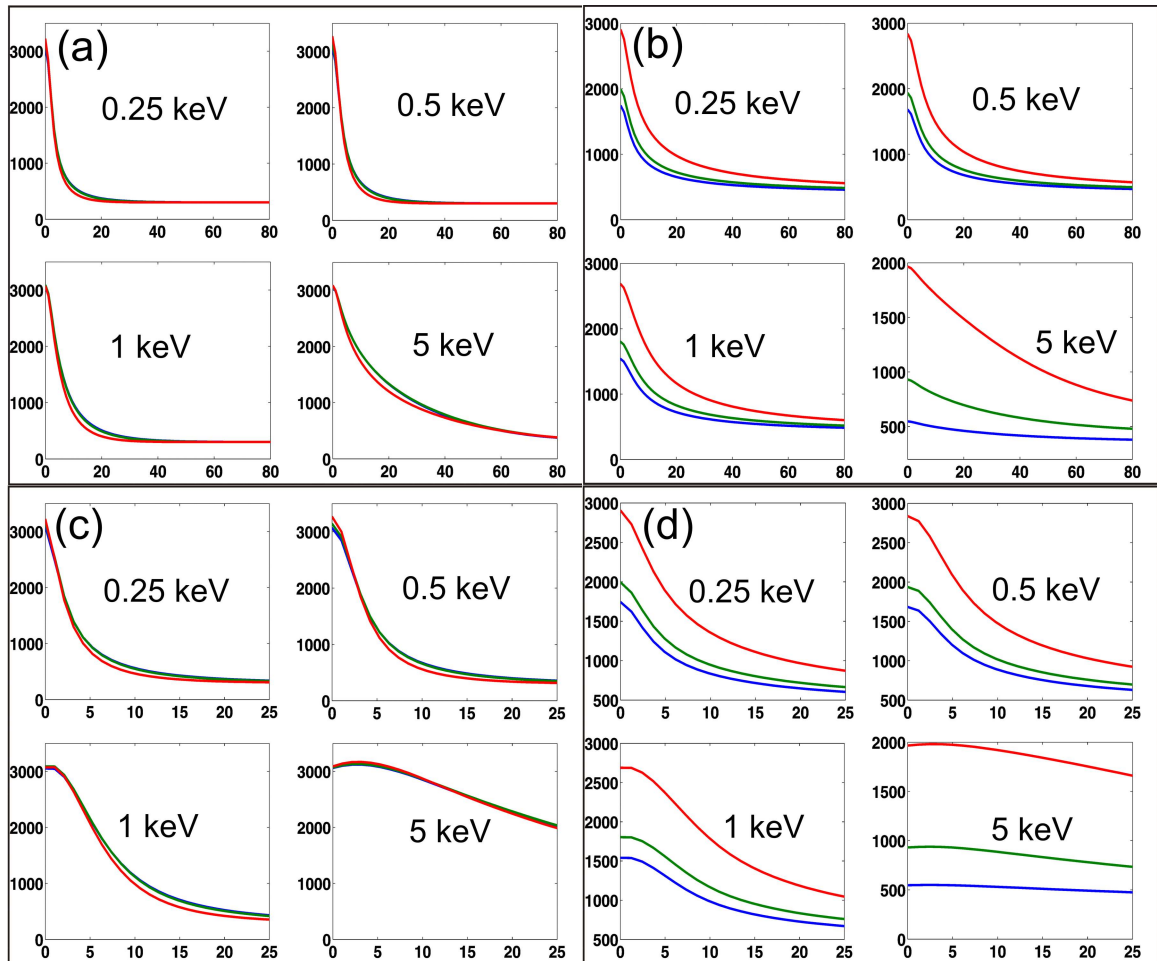


Figure 7.2 Temperature profile along the radius and axis of the films: a) and c) (left column) correspond to Ni; b) and d) (right column) correspond to Au in the radial and axial directions, respectively. For each accelerating voltage heating powers of 0.5 W (blue), 1 W (green) and 10 W (red) were considered for the electron beam. In all the plots, the  $x$ - axis is in nm and the  $y$ - axis in K.



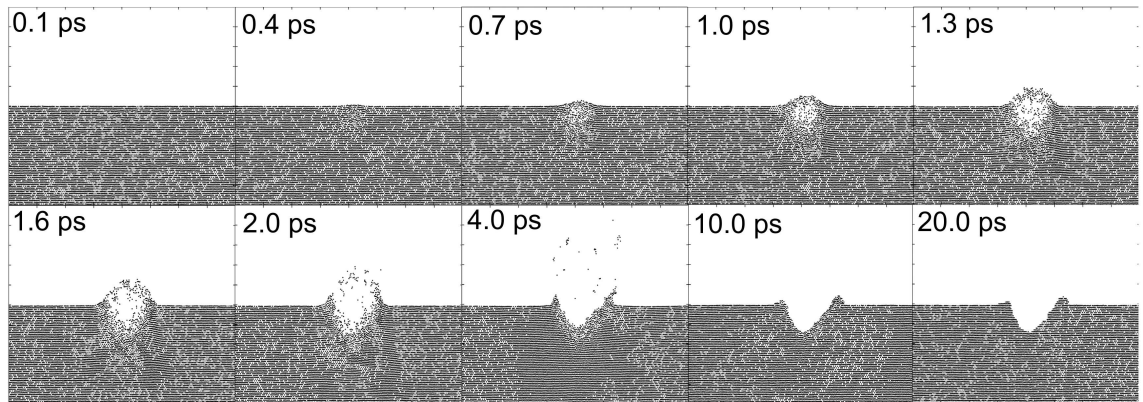


Figure 7.3 Snapshots of atomic positions of Ni workpiece in an  $x$  (horizontal:  $-20 - 20$  nm)  $-y$  (vertical:  $-10 - 10$  nm) plane  $0.352$  nm thick centered at  $z = 0$  nm. Simulations are for highly focused electron beam with an accelerating voltage of  $250$  V and heating power of  $0.5$  W.

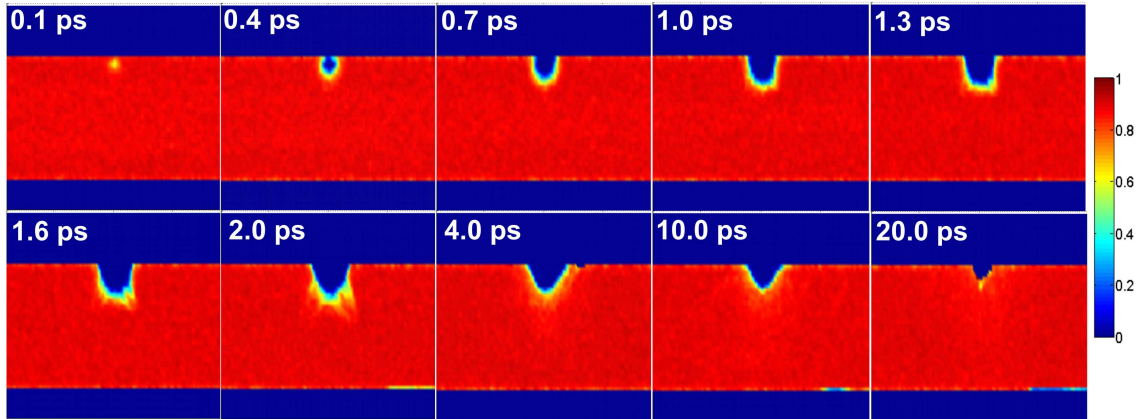


Figure 7.4 Melting sequence depicted within Ni film by the order parameter in an  $x$  (horizontal:  $-37 - 37$  nm)  $-y$  (vertical:  $-27 - 10$  nm) plane  $0.352$  nm thick centered at  $z = 0$  nm. Below  $0.04$  the material is considered a liquid. Simulations correspond to highly focused electron beam with an accelerating voltage of  $250$  V and heating power of  $0.5$  W.

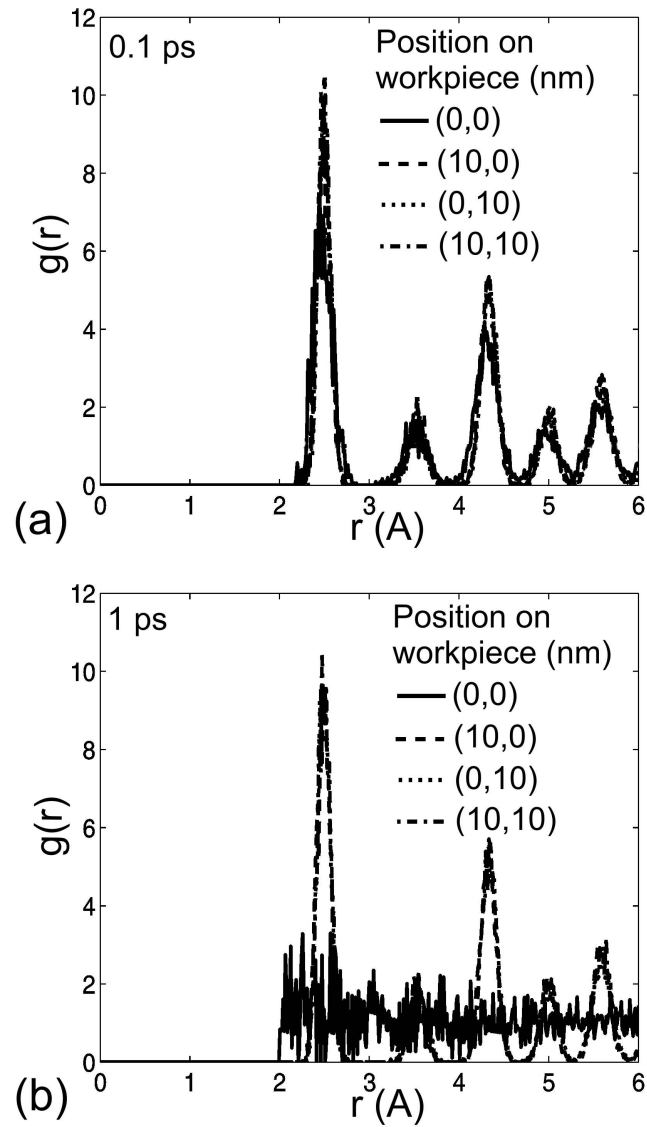


Figure 7.5 In plane radial distribution function at four locations of Ni film in the  $x$ - $y$  plane for various times during the nanomachining sequence. Conditions are the same as in Figs. 7.3 and 7.4.

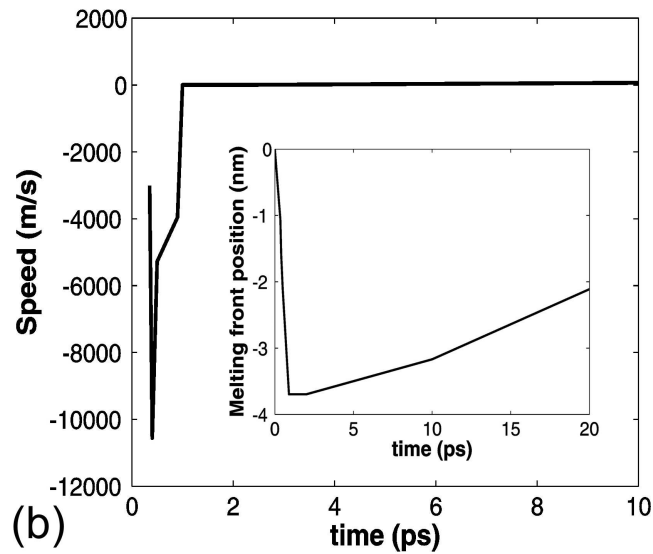
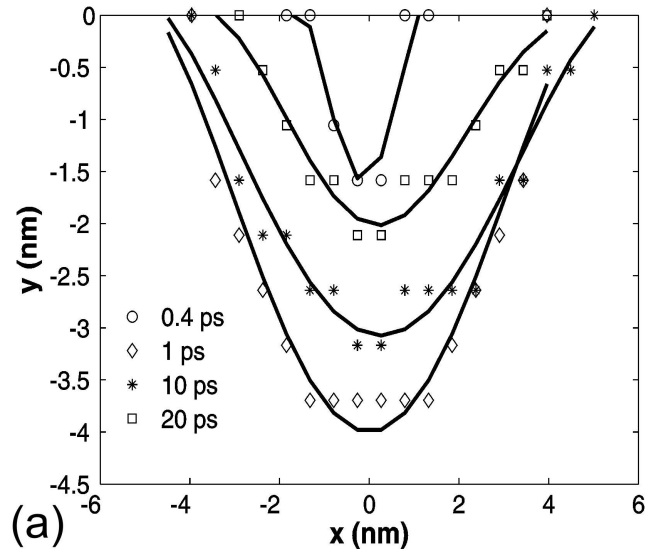


Figure 7.6 a) Position of solid-liquid interface in Ni film at various times. The marks correspond to the actual position and the lines are polynomials of 4<sup>th</sup> order that were used to fit the data. b) Speed of the melting front at the center of the workpiece. The inset shows its position as a function of time. In both cases, the results show the  $x$ - $y$  plane centered at  $z = 0$ . Conditions are the same as in Figs. 7.3 and 7.4.

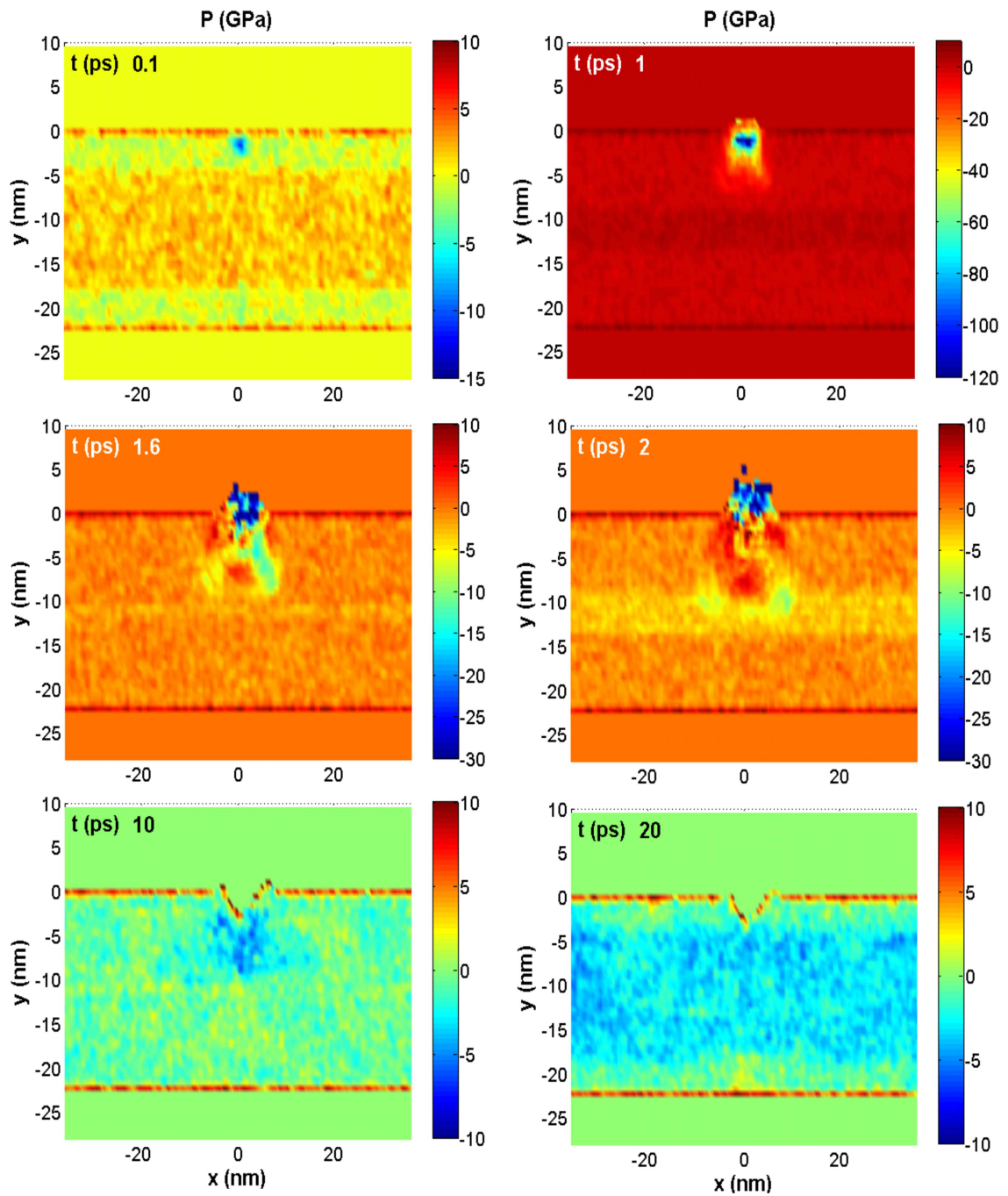


Figure 7.7 Stress profile on the Ni workpiece during the nanomachining process. Positive stresses are compressive; negative are tensile. Conditions are the same as in Figs. 7.3 and 7.4.

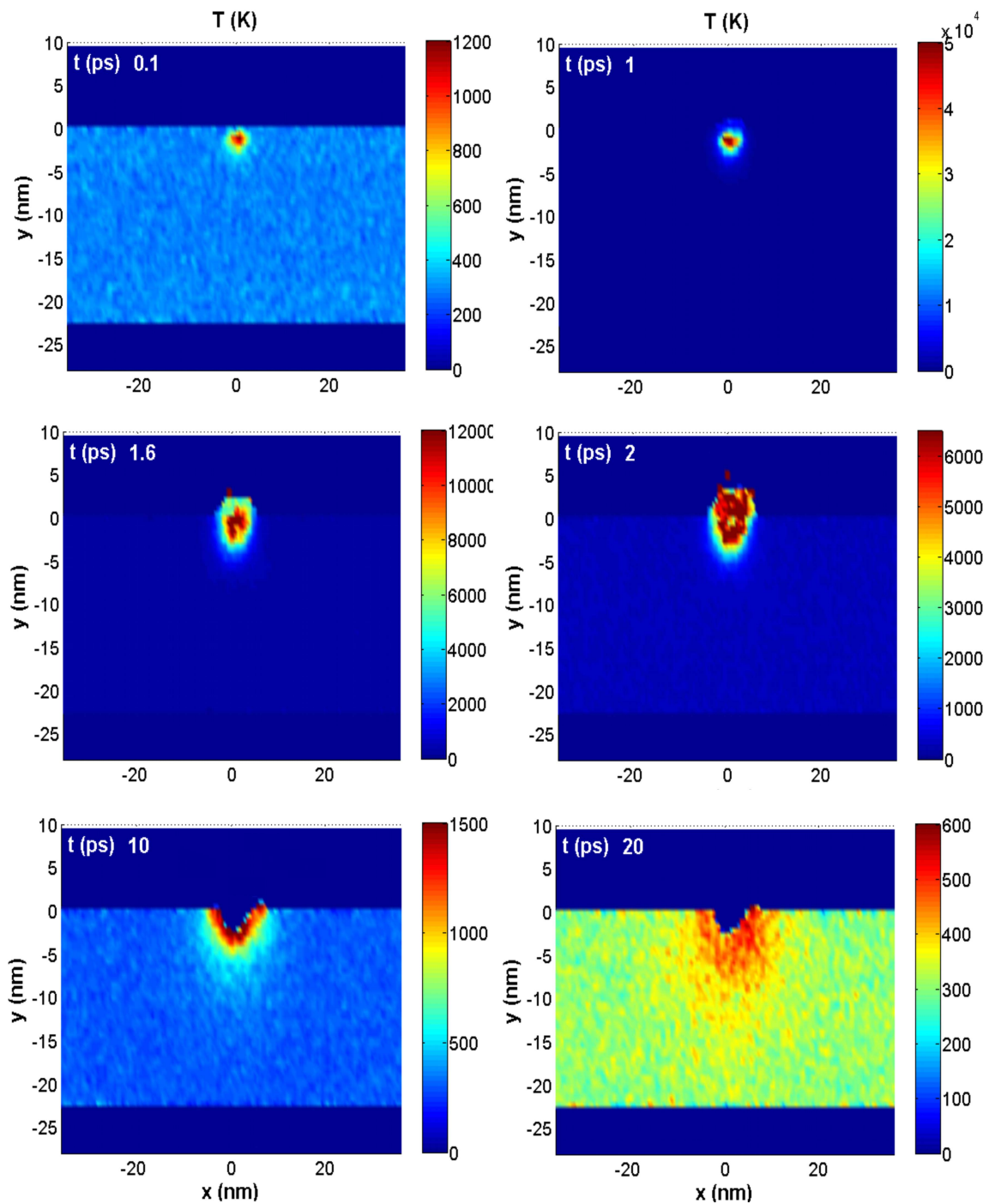


Figure 7.8 Temperature rise on the Ni workpiece during the nanomachining sequence. Conditions are the same as in Figs. 7.3 and 7.4.

## CHAPTER 8 ELECTRON FOCUSING TECHNIQUES AND FABRICATION OF ELECTRON GUNS

In the previous Chapters extensive numerical work was done to study the process of nanomachining using electrons. It was established that phase change of metals and material removal might be possible given that arrays of multiple CNTs are used, instead of a single CNT. Also, using a 3D hybrid numerical approach, the different parameters required for nanomachining based on applied voltage and material to be patterned were explored. All of these results indicate that if the electron-beam can be efficiently focused to a nanometer-sized spot on the surface, there will be sufficient amount of energy to create a nano-sized hole on a metallic surface. This Chapter begins with an overview of electron focusing mechanisms used in conventional EBL, followed by preliminary studies of novel focusing techniques that can be used for CNTs.

### 8.1 Electron beam lithography systems

An EBL column (Fig. 8.1) typically consists of an electron source, two or more lenses, a mechanism for deflecting the beam, a blanker for turning the beam on and off, a stigmator for correcting any astigmatism in the beam, apertures for helping to define the beam, alignment systems for centering the beam in the column, and finally, an electron detector for assisting with focusing and locating marks on the sample. The optical axis (Z) is parallel to the electron beam, while X and Y are parallel to the plane of the sample (Wang et al. 2003).

As mentioned in previous chapters, the EBL is not intended to make patterns in a surface by means of heating, such as the proposed concept of nanomachining. In the latter, electrons are used to directly transfer their energy to cause heating of the target. To make a defined hole, one then needs to provide a very large temperature gradient in a small region (see discussions in Chapter 7). On the other hand, EBL uses the electron beam to expose a resist (Cui 2005). A common positive electron beam resist is polymethyl methacrylate (PMMA). Electron beam exposure breaks the polymer into

fragments that can be dissolved in a mixture of MIBK:IPA developer (MIBK is Methyl Isobutyl Ketone and IPA is Isopropyl Alcohol). After the development process, the desired pattern is now on the resist. Subsequent steps are then used to transfer this pattern into another substrate. The different techniques available for pattern transfer are well reported in the literature in many books that deal with microfabrication techniques.

Due to the mechanisms involved in the focusing of the electrons in the EBL, the smaller the feature that needs to be patterned, the lower the energy of the electron beam that reaches the surface of the workpiece (brightness), essentially because less electrons manage to go through the different apertures and lenses in the focusing column. Thus, common currents measured in the emitter might be of hundreds of micro-Amperes, yet the reading on the workpiece might be of a few tenths of pico-Amperes. Below a certain level of focusing, the brightness of the electron beam is not high enough to expose the resist efficiently, and the minimum resolution of the system is obtained. Equipment available in the market today from companies such as Raith, just to name one provider, can achieve effective spot sizes of 20 nm or lower.

Even though EBL can achieve very small feature sizes, it has the disadvantage that it constitutes a serial process. In conventional applications, one would be interested in patterning complex shapes on a substrate. This can be achieved with the EBL, but it usually takes a very long time, depending on the complexity and size of the exposure. Thus, future progress in the field is oriented in devising electron beam systems that can work in parallel with multiple electron beams fired at the same time or sequentially. This topic and the requirements on focusing are discussed in the next section.

## 8.2 Electro-static lenses and emission from multiple CNTs

The next revolution in nanomanufacturing will come from fabrication methods that are cost effective, robust and precise. The state-of-the-art in micro-nanofabrication techniques is currently spearheaded by technologies such as the EBL. A parallel EBL system is a very attractive prospect because it offers the ultra-high resolution of the electrons, with the speed of today's photolithography that works in parallel mode. The



costly step of mask making followed by EUV or X-ray photolithography can then be skipped.

Electron field-emission from multiple CNTs has been contemplated as a potential candidate for such systems. As shown so far, however, a nano-sized feature can only really be resolved if there is an effective means of focusing the electrons. Electro-static lenses have been considered by several groups (Hofmann and MacDonald 1997; Binh et al. 1998; Guillorn et al. 2001, 2002; Baylor et al. 2002, 2004; Teo et al. 2003; Bae et al. 2004). Only in the past 8 years there have been 24 filings for patents of systems that offer new ways of achieving focused electron beams and 5 of those that use CNTs as the electron sources. The applications are usually related to field-emission flat panel displays and new electron beam lithography systems that are also aimed to exposing a resist such as PMMA.

An example of such a system of multiple CNTs is shown in Fig. 8.2 from the work of Teo et al. (2003). Note that the CNTs are grown inside an “extraction gate” and the focusing gate is not shown in Fig. 8.2. An extension of their work would be to wire the emitters in a way that they can be fired sequentially as proposed in a recent work (Wong et al. 2006). The practical aspects of such systems are very challenging and certainly open the possibility for future work in the field.

### 8.2.1 Preliminary modelling of electro-static lenses

Simulations were carried to investigate certain aspects of the electro-static lenses. Specifically, one is interested in determining what their effect is on the overall behaviour of the CNT. Additionally, the formulations discussed in Chapter 2 were used, to study the effect on the electron trajectories. A case in which a CNT is vertically aligned with an extraction gate followed by a focusing gate (see Fig. 8.3) was considered. In this way, one needs to apply a voltage  $V_1$  at the extraction gate to induce the process of field-emission at the CNT; then a voltage  $V_2$  is applied on the focusing gate so that electron trajectories are deflected and one achieved focusing. In the work by Teo et al. (2003), the focusing gate was placed several hundred microns away from the extraction gate

followed by a filter to effectively block parts of the electron beam and achieve focusing on a small spot. Baylor et al. (2004), on the other hand placed the focusing gate just 1  $\mu\text{m}$  away from the extraction gate and so in their work, they report that both the vertically aligned CNT, with an extraction gate and focusing gate can be fabricated at the same time. In this way, the emitter already includes the required electron optics. They also provided early experimental results of their system by exposing a PMMA target. In their earlier work, they considered an extraction gate followed by three focusing gates, but this was not backed with experimental evidence of the feasibility of their design (Baylor et al. 2002). What all of these previous works show, is that the combinations of geometry of the gates, with the voltages applied to them, as well as the geometry of the emitter are virtually infinite, and optimization of the parameters that give the best combinations based on efficient focusing can only be done by trial and error.

In an attempt to begin tackling this problem, the minimum gap distance  $s$  that affects the electro-static solution around the CNT was studied, and thus affects the field-emission current. The geometry considered was the one proposed by Baylor et al. (2004) as seen in Fig. 8.4 although other combinations found in the literature are also plausible. Thus, the parameter used in Fig. 8.3 are  $r_1 = 750 \text{ nm}$ ,  $z_1 = 200 \text{ nm}$ ,  $r_2 = 1 \mu\text{m}$ ,  $z_2 = 1 \mu\text{m}$ , the height of the CNT as 1  $\mu\text{m}$  and the radius as 15 nm. The thickness of the gates was measured to be 150 nm. In their experiments the gap distance between the top of the focus gate was set at  $z_3 = 500 \mu\text{m}$  (Baylor et al. 2004). Also, the voltage between gates was measured to be greater than 180 V with the recommendation that the voltage applied at the focus gate is above the extraction gate. Based on this recommendations,  $V_1 = 100 \text{ V}$  and  $V_2 = 280 \text{ V}$  were set in the model. Finally, the kinetic energy of the electrons that reach the workpiece is determined by the anode potential, which is set at 500 V, thus resulting in an electron beam with 500 eV. In Fig. 8.4 the effect on the total field-emission current calculated by integrating Eq. (2.12) on the surface of the CNT as a function of distance  $z_3$  (see Fig. 8.3) is shown. Additional cases were considered based on different combinations of  $r_1$  and  $r_2$  as illustrated in Table 8.1.

As seen in Fig. 8.4, reducing the distance  $z_3$  below 10  $\mu\text{m}$  seems to have a direct effect on the total emission current. Note that this emission current was calculated following the same approach as discussed in Chapter 2, basically integrating over the entire area of the CNT surface. As far as the electron emission, it was found in all the cases a smooth distribution of the electric field on the periphery of the CNT, indicating that electrons are emitted uniformly from every point in the tip, also seen in the discussions in Chapter 2. Also, different cases were considered in which the radii of the gates were varied by a factor of 10 from the original settings in (Baylor et al. 2004). The results show that the radius of the extraction gate is more critical than the focusing gate in setting the magnitude of the emission current. As indicated in Fig. 8.4, the dashed line demarks a boundary below which the emission current cannot be measured, based on current technology. However, it still can be calculated based on the knowledge of the electric field on the tip.

A calculation of the focusing efficiency of the system depicted in Fig. 8.4 was attempted, but the results indicate that even though a number of electrons reach the workpiece with a certain amount of focusing, most of the emitted electrons will end up hitting the gates and never reaching the workpiece. A similar situation found in conventional electron focusing. This is because of the large magnitude of the repulsion forces between travelling electrons due to Coulomb forces.

Another situation that needs to be investigated is the focusing effects of the system due to emission from multiple CNTs at the same time. Due to limitations in computational power, these simulations were not carried out as their implementation would require a full 3D solution of both the electrostatic problem and the electron trajectories. Nevertheless, this opens the potential for future work in this area.

### 8.3 Comments

In this Chapter, the modelling presented in Chapter 2 was extended, to analyse the feasibility of using CNTs with self focusing cathodes. These systems can be used as the electron guns that could provide sufficient energy to achieve the significant temperature

gradients required by nanomachining. The modelling and experimental tasks ahead based on this approach are enormous. Our attempts are just to show the effects that the geometries of the gates have on the field-emission current of the CNT. This analysis was done with the hope that it will guide future experiments in this area.

Table 8.1  
Geometrical combinations used for the electro-static problem in Fig. 8.3

Case	$r_1$ ( $\mu\text{m}$ )	$r_2$ ( $\mu\text{m}$ )
1	0.75	1
2	0.75	10
3	7.5	1
4	7.5	10

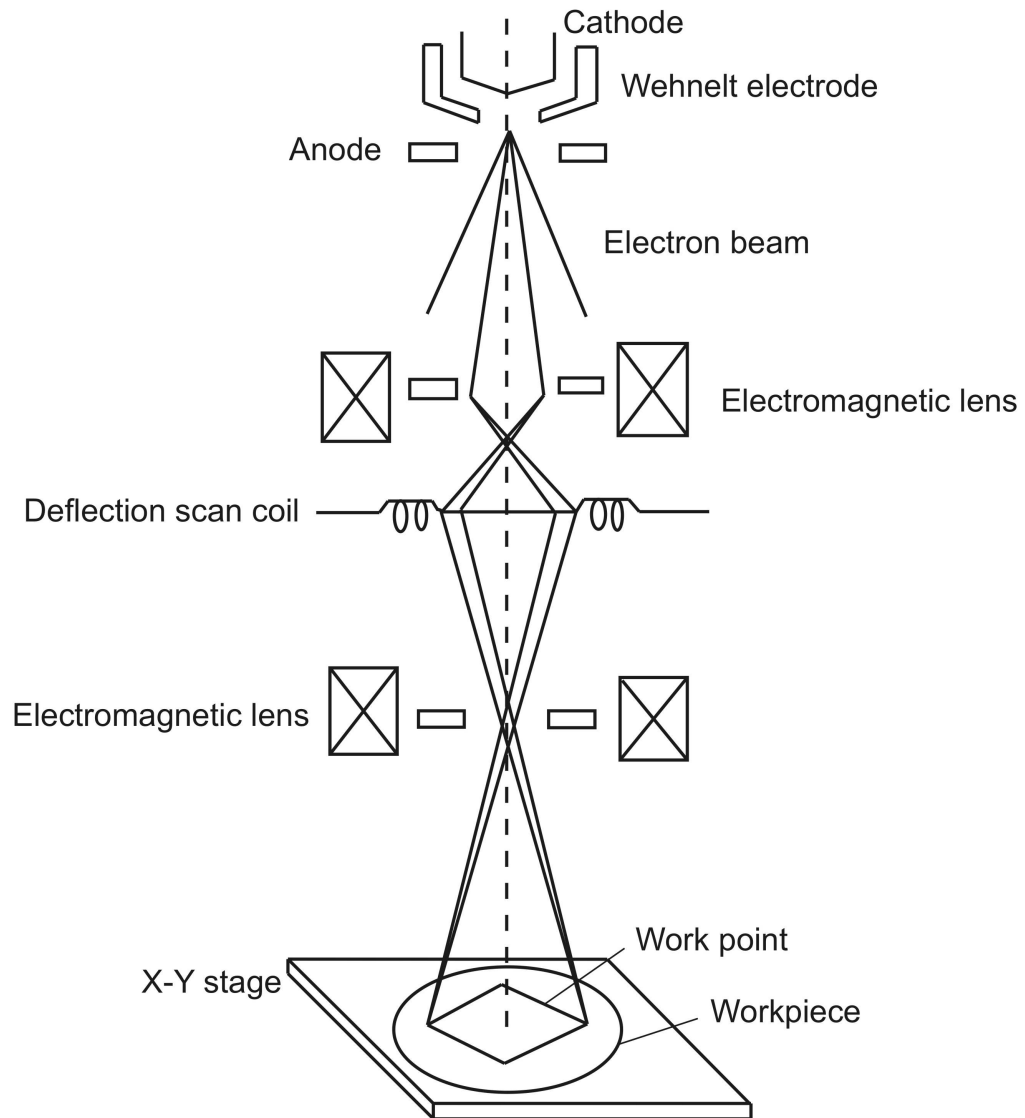


Figure 8.1 Electron beam processing equipment. Electrons are generated and accelerated by the electron gun and guided through the column by the electromagnetic lenses and the deflection scan coil. Both the scanning system and the x-y-z stage are used to define the working point on the workpiece (Wang et al. 2003).

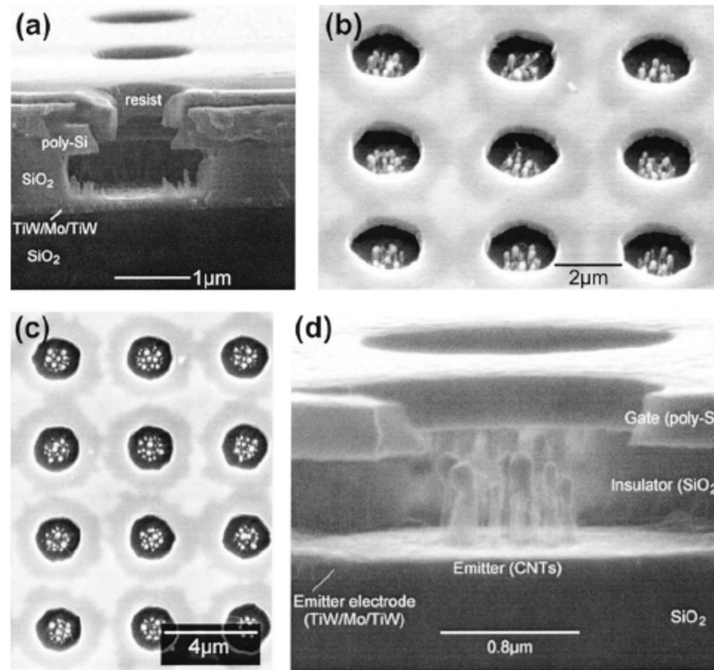


Figure 8.2 a) Cross section SEM showing the undercut of the poly-Si and SiO<sub>2</sub> beneath the resist. b) Tilted 45° view of the microcathode after nanotube growth. c) Top view clearly shows the centrally located nanotubes (bright dots) with respect to the gate hole. d) Cross section SEM of the microcathode (Teo et al. 2003).

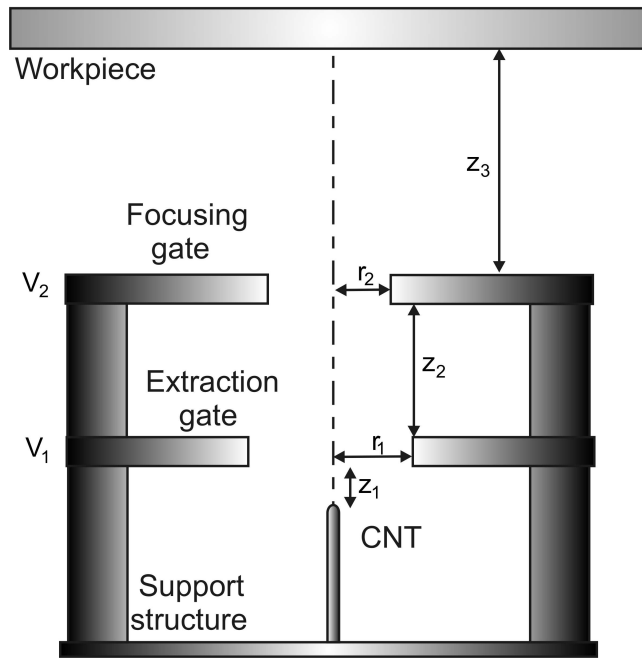


Figure 8.3 Single CNT vertically aligned with an extraction gate and a focusing gate.



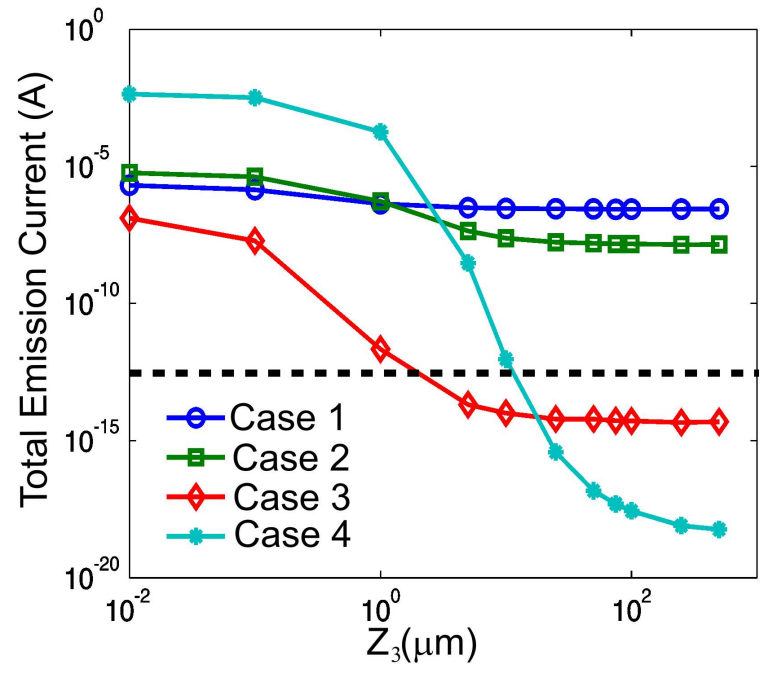


Figure 8.4 Effect on the total emission current of the different cases shown in Table 8.1. The dashed line indicates the cutoff below which the emission current cannot be measured.

## CHAPTER 9 SUMMARY

This dissertation was an attempt to tackle the different aspects of a concept that utilizes field-emission electrons from a CNT to pattern nano-features on the surface of a metal. The material was presented in a coherent way and followed a rigorous simulation strategy pinpointing the governing equations that comprise the physics that take place during nanomachining. The following sections lay out the main conclusions obtained from this work, as well as the grounds for future work.

### 9.1 Conclusions

From this study it was learned that the heat transport phenomena that take place in the CNT during field-emission puts a limit on the maximum voltage that can be applied based on the governing heating mechanisms. Thus, for constant operation of field-emission from a CNT, one needs to ensure that the current is below 1  $\mu\text{A}$ , which is set by the geometry of the CNT and the gap distance. It was also established that the geometry of the CNT is a key factor that affects the deposition profiles of the emitted electrons.

The Monte Carlo results based on the electron emission profiles from the CNT, suggest that in order to have maximum penetration of the electron beam inside workpiece, the voltage needs to be high. However, based on the limitation imposed by the heating of the CNT, larger voltages can only be applied if the gap distance is relatively large. This in turn means that the spread of the electron beam on the surface will span several tens of microns making the electron beam more dilute inside the material, and reducing the heating effect of the electrons inside the workpiece. Our findings in this area are in line with previous experiments and simulations cited in this work. There is a potential, though, based on the fact that the emission from multiple CNTs grown in arrays can be achieved, that can provide sufficient heating power to induce melting of a metallic surface

In trying to study the phase change processes at the nanoscale based on the potential of large heating powers, a hybrid numerical method was developed based on the two-temperature model and molecular dynamics. This allows one to study the heating process of the workpiece more realistically than with previous approaches based on continuum models. Using this methodology, it was found that the electronic properties of the material of the workpiece are a crucial factor in obtaining defined patterns based on heating with electrons. It was found that materials with lower electronic diffusivity will be more easily machined in defined patterns than others with larger diffusivity that tend to heat up and melt more uniformly.

The combination of these numerical methods was then extended to a potential case where a highly focused source of electrons is available for nanomachining. It was found that for low electronic diffusivity materials, there is a large concentration of energy close to the surface, which in turn results in a build up of tensile stress. These stresses lead to a phase explosion of the material, leaving behind a well defined crater.

Finally, certain alternatives to potential focusing mechanisms were contemplated to make sure that the amount of electron energy that reaches the workpiece is enough to induce phase change. It is believed that the next big step in nanomanufacturing will be in systems based on massively parallel electro-beam emitters such as CNTs with self focusing cathodes.

## 9.2 Future work

This work has the potential of being extended in several different directions which are listed below.

### 9.2.1 Accurate electron deposition profiles

The solutions provided by the MC method used throughout this work, correspond to the steady-state solution of the EBTE. A more accurate representation of the process would be to use the time-dependent electron propagation profile inside the material as the electron-beam heats the workpiece. This is not a trivial task as it requires the solution of

the electron-phonon hydrodynamic equation which contains seven partial differential equations (PDEs) that need to be solved at the same time. More importantly, the scattering cross sections used here to find the steady-state solution of the EBTE are valid for materials in the solid phase. The error in using these approximations when the material is in the liquid/vapor phase (as in the simulation results in Chapters 6 and 7) needs to be checked.

### 9.2.2 Extension of hybrid TTM-MD method to other materials

In this work, the concentration was mainly on nanomachining of Au, Cu and Ni workpieces as the properties of these materials are readily available in the literature. However, the extension of the approaches presented here to materials important in the semiconductor industry or biological materials offers a window of opportunity. This, however, requires a potential reformulation of the approach that was presented here, as the assumptions made for metals might not be accurate for other materials. Also, the timescale of the simulated processes is very small, in the order of nanoseconds at best. Current technology used in the microfabrication industry usually operates at the millisecond scale. Thus, other approaches such as meso-scale simulations or coarse grained MD simulations could be considered to extend the timescale of the simulations and predict the results of real experiments.

### 9.2.3 Experimental verification of electron beam based nanomachining

One of the major issues that still requires insight for electron-beam nanomachining to become a reality is the problem of electron focusing. The main problem that needs to be addressed is how to effectively focus a high energy/high current electron beams into a nanometer-sized target. Further research in this area needs to be done as the requirements for smaller feature sizes become greater every day. Complex electron focusing systems such as those used in EBL have been around for decades, and though functional, they still are expensive, and most importantly serial.

#### 9.2.4 Exploration of novel focusing systems for parallel electron beam nanomachining

Assuming that one can effectively focus the electrons into a nanometer scale, one is still left with the problem faced by conventional electron beam systems. Serial processing is the major bottleneck in the field and needs to be addressed. A system that is capable of working in parallel, and yet deliver the same resolution as the established technology, is thus very attractive. One venue that offers a window of opportunity in this field is provided by the use of CNT islands with extraction gates and self-focusing cathodes. The task is not a trivial one, however, and is constantly been researched by several groups by means of constantly improving micro-manufacturing techniques.

#### 9.2.5 Thermodynamic analysis of phase change at the nanoscale

In order to determine the energy required by the electron beam to remove a given number of atoms from a surface, one needs to have an idea of the energies binding them together. Even though the discussions in this dissertation tackled certain aspects of phase change, the modeling presented here shows what “would” happen to a metal target given that a certain amount of energy is provided. The real question is how much energy “is” needed to accomplish this task. In order to solve this problem, further investigation needs to understand exactly what phase change is when the domain is in the range of a few nanometers, and thus, containing a finite number of atoms.

## REFERENCES

- Abramowitz, I., and I. A. Stegun (1964). Handbook of Mathematical Functions, U.S. Department of Commerce.
- Allen, P. B. (1987). "Theory of Thermal Relaxation of Electrons in Metals." Physical Review Letters **59**(13): 1460-1463.
- Al-Rawi, A. N., A. Kara and T. S. Rahman (2000). "Anharmonic effects on Ag(111): a molecular dynamics study." Surface Science **446**(1-2): 17-30.
- Andersen, H. C. (1980). "Molecular-Dynamics Simulations at Constant Pressure and-or Temperature." Journal of Chemical Physics **72**(4): 2384-2393.
- Anisimov, S. I., and B. Rethfeld (1997). "On the theory of ultrashort laser pulse interaction with a metal " Proceedings of SPIE 3093: 192.
- Ashcroft, N. W. and N.D. Mermin (1976). Solid State Physics. Philadelphia, Saunders Company.
- Bae, S., W. J. Seo, S. Choi, S. Lee and K. H. Koh (2004). "Double-gate field emitters with planar carbon-nanoparticle cathodes: Simulation studies." Journal of Vacuum Science & Technology B **22**(3): 1303-1307.
- Baylor, L. R., D. H. Lowndes, M. L. Simpson, C. E. Thomas, M. A. Guillorn, V. I. Merkulov, J. H. Whealton, E. D. Ellis, D. K. Hensley and A. V. Melechko (2002). "Digital electrostatic electron-beam array lithography." Journal of Vacuum Science & Technology B **20**(6): 2646-2650.
- Baylor, L. R., W. L. Gardner, X. Yang, R. J. Kasica, M. A. Guillorn, B. Blalock, H. Cui, D. K. Hensley, S. Islam, D. H. Lowndes, A. V. Melechko, V. I. Merkulov, D. C. Joy, P. D. Rack, M. L. Simpson and D. K. Thomas (2004). "Initial lithography results from the digital electrostatic e-beam array lithography concept." Journal of Vacuum Science & Technology B **22**(6): 3021-3024.
- Berber, S., Y. K. Kwon and D. Tomanek (2000). "Unusually high thermal conductivity of carbon nanotubes." Physical Review Letters **84**(20): 4613-4616.
- Berendsen, H. J. C., J. P. M. Postma, W. F. Vangunsteren, A. Dinola and J. R. Haak (1984). "Molecular-Dynamics with Coupling to an External Bath." Journal of Chemical Physics **81**(8): 3684-3690.
- Bilalbegovic, G. and E. Tosatti (1993). "Incomplete Melting of the Au(100) Surface." Physical Review B **48**(15): 11240-11248.

- Binh, V. T., V. Semet, D. Guillot, P. Legagneux and D. Pribat (1998). "Microguns with 100-V electron beams." Applied Physics Letters **73**(14): 2048-2050.
- Bonard, J. M., K. A. Dean, B. F. Coll and C. Klinke (2002). "Field emission of individual carbon nanotubes in the scanning electron microscope." Physical Review Letters **89**(19): 197602
- Born, M., and Th. Von Karman (1912). "Uber Schwingungen in Raumgittern." Physik. Z. **13**: 297-309.
- Born, M. (1939). "Thermodynamics of crystals and melting." Journal of Chemical Physics **7**: 591-603.
- Bube, R. H. (1974). Electronic Properties of Crystalline Solids: An Introduction to Fundamentals. New York, Academic Press.
- Caffrey, A. P., P. E. Hopkins, J. M. Klopff and P. M. Norris (2005). "Thin film non-noble transition metal thermophysical properties." Microscale Thermophysical Engineering **9**(4): 365-377.
- Campbell, S. A. (2001). The Science and Engineering of Microelectronic Fabrication. New York, Oxford University Press.
- Carnevali, P., F. Ercolessi and E. Tosatti (1987). "Melting and Nonmelting Behavior of the Au(111) Surface." Physical Review B **36**(12): 6701-6704.
- Charbonnier, F. M., R. W. Strayer, L. W. Swanson and E. E. Martin (1964). "Nottingham Effect in Field and T-F Emission: Heating and Cooling Domains, and Inversion Temperature." Physical Review Letters **13**(13): 397-401.
- Chen, G. (2005). Nanoscale Energy Transport and Conversion: A Parallel Treatment of Electrons, Molecules, Phonons, and Photons. New York, Oxford University Press.
- Chen, Y., S. Y. Tong, J. S. Kim, L. L. Kesmodel, T. Rodach, K. P. Bohnen and K. M. Ho (1991). "Characterization of Surface Phonons on Cu(001) and Ag(001) - 1st-Principles Phonon Calculations with Experimental and Theoretical-Studies of High-Resolution Electron-Energy-Loss Spectra." Physical Review B **44**(20): 11394-11401.
- Cho, S. A. (1982). "Role of Lattice Structure on the Lindemann Fusion Theory of Metals." Journal of Physics F-Metal Physics **12**(6): 1069-1083.
- Chokappa, D. K., S. J. Cook and P. Clancy (1989). "Nonequilibrium Simulation Method for the Study of Directed Thermal-Processing." Physical Review B **39**(14): 10075-10087.

- Clementi, E., and C. Roetti (1974). "Roothaan-Hartree-Fock atomic wave functions. Basis functions and their coefficients for ground and certain excited states of neutral and ionized atoms, Z .leq.54." Atomic Data and Nuclear Data Tables **14**(3-4): 177-478.
- Cui, Z. (2005). Micro-Nanofabrication: Technologies and Applications, Springer.
- Dai, H. J., E. W. Wong and C. M. Lieber (1996). "Probing electrical transport in nanomaterials: Conductivity of individual carbon nanotubes." Science **272**(5261): 523-526.
- Das, P. S. and L. T. Wille (2002). "Atomistic and continuum studies of carbon nanotubes under pressure." Computational Materials Science **24**(1-2): 159-162.
- Davisson, C., and L.H. Germer (1920). "The thermionic work function of tungsten." Phil. Mag. **40**: 746
- Daw, M. S. and M. I. Baskes (1984). "Embedded-Atom Method - Derivation and Application to Impurities, Surfaces, and Other Defects in Metals." Physical Review B **29**(12): 6443-6453.
- Derouffignac, E., G. P. Alldredge and F. W. Dewette (1981). "Dynamics of Xenon-Covered Graphite Slabs." Physical Review B **24**(10): 6050-6059.
- Ding, Z. J. and R. Shimizu (1996). "A Monte Carlo modeling of electron interaction with solids including cascade secondary electron production." Scanning **18**(2): 92-113.
- Edgcombe, C. J., and U. Valdré (2001). "Microscopy and computational modeling to elucidate the enhancement factor for field electron emitters." Journal of Microscopy **203**(2): 188-194.
- Ferry, D. K. and S. M. Goodnick (1997). Transport in nanostructures. New York, Cambridge University Press.
- Fisher, T. S., D. G. Walker and R. A. Weller (2003). "Analysis and simulation of anode heating due to electron field emission." IEEE Transactions on Components and Packaging Technologies **26**(2): 317-323.
- Foiles, S. M., M. I. Baskes and M. S. Daw (1986). "Embedded-Atom-Method Functions for the Fcc Metals Cu, Ag, Au, Ni, Pd, Pt, and Their Alloys." Physical Review B **33**(12): 7983-7991.
- Forsythe, W. E. and A. G. Worthing (1925). "The properties of tungsten and the characteristics of tungsten lamps." Astrophysical Journal **61**(3): 146-185.
- Fowler, R. H., and L.W. Nordheim (1928). "Electron emission in intense electric fields." Proc. Roy. Soc. (London) A119: 8.



- Fowler, R. H., and E. A. Guggenheim (1952). Statistical Thermodynamics. New York, Cambridge University Press.
- Francoeur, M., and M. P. Mengüç, (2008). "Role of fluctuational electrodynamics in near-field radiative heat transfer." Journal of Quantitative Spectroscopy & Radiative Transfer **109**(2): 280-293.
- Fransen, M. J. (1999). Towards High - Brightness, Monochromatic Electron Sources. Rotterdam, Technische Universiteit Delft. ter verkrijging van de graad van doctor: 174.
- Franssila, S. (2004). Introduction to microfabrication. Hoboken, NJ, J. Wiley.
- Frenkel, D., and B. Smit, (2002). Understanding Molecular Simulation: From Algorithms to Applications, Elsevier
- Fujieda, T., K. Hidaka, M. Hayashibara, T. Kamino, Y. Ose, H. Abe, T. Shimizu and H. Tokumoto (2005). "Direct observation of field emission sites in a single multiwalled carbon nanotube by Lorenz microscopy." Japanese Journal of Applied Physics Part 1- Regular Papers Short Notes & Review Papers **44**(4A): 1661-1664.
- Fujii, M., X. Zhang, H. Q. Xie, H. Ago, K. Takahashi, T. Ikuta, H. Abe and T. Shimizu (2005). "Measuring the thermal conductivity of a single carbon nanotube." Physical Review Letters **95**(6): 065502.
- Gao, G. H., T. Cagin and W. A. Goddard (1998). "Energetics, structure, mechanical and vibrational properties of single-walled carbon nanotubes." Nanotechnology **9**(3): 184-191.
- Gao, R. P., Z. W. Pan and Z. L. Wang (2001). "Work function at the tips of multiwalled carbon nanotubes." Applied Physics Letters **78**(12): 1757-1759.
- Gomer, R. (1993). Field Emission and Field Ionization.
- Good, R. H., and E.W. Muller (1956). Handbuch der Physik. Berlin, Springer-Verlag.
- Grafstrom, S. (2002). "Photoassisted scanning tunneling microscopy." Journal of Applied Physics **91**(4): 1717-1753.
- Gratzke, U. and G. Simon (1995). "Mechanism of Nanostructure Formation with the Scanning Tunneling Microscope." Physical Review B **52**(11): 8535-8540.
- Gray, C. G., and K. E. Gubbins (1984). Theory of Molecular Fluids. Oxford, Clarendon.
- Gray, D. E. (1972). American Institute of Physics Handbook. New York, McGraw-Hill.

Guillorn, M. A., A. V. Melechko, V. I. Merkulov, E. D. Ellis, M. L. Simpson, L. R. Baylor and G. J. Bordonaro (2001). "Microfabricated field emission devices using carbon nanofibers as cathode elements." Journal of Vacuum Science & Technology B **19**(6): 2598-2601.

Guillorn, M. A., A. V. Melechko, V. I. Merkulov, D. K. Hensley, M. L. Simpson and D. H. Lowndes (2002). "Self-aligned gated field emission devices using single carbon nanofiber cathodes." Applied Physics Letters **81**(19): 3660-3662.

Guo, T., P. Nikolaev, A. G. Rinzler, D. Tomanek, D. T. Colbert and R. E. Smalley (1995). "Self-Assembly of Tubular Fullerenes." Journal of Physical Chemistry **99**(27): 10694-10697.

Haile, J. M. (1992). Molecular Dynamics Simulations: Elementary Methods. New York, Wiley-Interscience Publication.

Hakkinen, H. and U. Landman (1993). "Superheating, Melting, and Annealing of Copper Surfaces." Physical Review Letters **71**(7): 1023-1026.

Hii, K. F., R. R. Vallance, S. B. Chikkamaranahalli, M. P. Mengüç and A. M. Rao (2006). "Characterizing field emission from individual carbon nanotubes at small distances." Journal of Vacuum Science & Technology B **24**(3): 1081-1087.

Hofmann, W. and N. C. MacDonald (1997). "Micromachined single-crystal silicon electron lenses." Journal of Vacuum Science & Technology B **15**(6): 2713-2717.

Hohlfeld, J., S. S. Wellershoff, J. Gudde, U. Conrad, V. Jahnke and E. Matthias (2000). "Electron and lattice dynamics following optical excitation of metals." Chemical Physics **251**(1-3): 237-258.

Hone, J., M. Whitney, C. Piskoti and A. Zettl (1999). "Thermal conductivity of single-walled carbon nanotubes." Physical Review B **59**(4): R2514-R2516.

Hone, J., M. C. Llaguno, M. J. Biercuk, A. T. Johnson, B. Batlogg, Z. Benes and J. E. Fischer (2002). "Thermal properties of carbon nanotubes and nanotube-based materials." Applied Physics A: Materials Science & Processing **74**(3): 339-343.

Hoover, W. G. (1986). "Constant-Pressure Equations of Motion." Physical Review A **34**(3): 2499-2500.

Howatson, A. M., P.G. Lund, and J.D. Todd (1992). Engineering Tables and Data, Kluwer Academic Pub.

Huang, S. M., M. H. Hong, Y. F. Lu, B. S. Lukyanchuk, W. D. Song and T. C. Chong (2002). "Pulsed-laser assisted nanopatterning of metallic layers combined with atomic force microscopy." Journal of Applied Physics **91**(5): 3268-3274.

- Huang, N. Y., J. C. She, J. Chen, S. Z. Deng, N. S. Xu, H. Bishop, S. E. Huq, L. Wang, D. Y. Zhong, E. G. Wang and D. M. Chen (2004). "Mechanism responsible for initiating carbon nanotube vacuum breakdown." Physical Review Letters **93**(7): 075501.
- Iijima, S. (1991). "Helical Microtubules of Graphitic Carbon." Nature **354**(6348): 56-58.
- Incropera, F. P., and DeWitt, D.P. (1996). Heat Transfer Fundamentals, Prentice Hall.
- Ivanov, D. S. and L. V. Zhigilei (2003). "Combined atomistic-continuum modeling of short-pulse laser melting and disintegration of metal films." Physical Review B **68**(6): 064114.
- Jansen, G.H. (1988), "Coulomb interactions in particle beams." Journal of Vacuum Science & Technology B **6**(6): 1977-1983.
- Janz, G. J. (1988). "Thermodynamic and Transport Properties of Molten Salts: Correlation Equations for Critically Evaluated Density, Surface Tension, Electrical Conductance, and Viscosity Data." Journal of Physical and Chemical Reference Data, Supplement **17**(2): 399.
- Joseyacamán, M., M. Mikiyoshida, L. Rendon and J. G. Santiesteban (1993). "Catalytic Growth of Carbon Microtubules with Fullerene Structure." Applied Physics Letters **62**(2): 202-204.
- Joy, D. C. (2001). A database of electron-solid interactions, Oak Ridge National Laboratory.
- Kaganov, M. I., I.M. Lifshitz, and L.V. Tanatarov (1957). "Relaxation between electrons and crystalline lattices." Soviet Physics JETP **4**: 5.
- Kim, P., L. Shi, A. Majumdar and P. L. McEuen (2001). "Thermal transport measurements of individual multiwalled nanotubes." Physical Review Letters **87**(21): 215502.
- Kincaid, D., and W. Cheney (2002). Numerical Analysis: Mathematics of Scientific Computing. Belmont, Calif., Brooks/Cole-Thomson Learning.
- Kittel, C. (1995). Introduction to Solid State Physics New York, John Wiley & Sons.
- Kohn, W. and L. J. Sham (1965). "Self-Consistent Equations Including Exchange and Correlation Effects." Physical Review **140**(4A): 1133.
- Koleske, D. D. and S. J. Sibener (1992). "Phonons on Fcc (100), (110), and (111) Surfaces Using Lennard-Jones Potentials .1. Comparison between Molecular-Dynamics Simulations and Slab Technique Calculations." Surface Science **268**(1-3): 406-417.

- Kumar, R. R. (2006). Numerical Investigation and Parallel Computing for Thermal Transport Mechanism During Nanomachining. Mechanical Engineering. Lexington, University of Kentucky. Master of Science: 118.
- Li, C. and T.-W. Chou (2003). "A structural mechanics approach for the analysis of carbon nanotubes." International Journal of Solids and Structures **40**(10): 2487-2499.
- Liboff, R. L. (1998). Kinetic Theory. New York, Wiley.
- Lide, D. (1995). CRC Handbook of Chemistry and Physics, CRC Press.
- Lindemann, F. A. (1910). "The Calculation of Molecular Vibration Frequencies." Physik. Z. **11**: 609-612.
- Makinson, R. E. B. (1938). "The thermal conductivity of metals." Proceedings of the Cambridge Philosophical Society **34**: 474-497.
- Miller, S. C. and R. H. Good (1953). "A WKB-Type Approximation to the Schrodinger Equation." Physical Review **91**(1): 174-179.
- Minh, P. N., L. T. T. Tuyen, T. Ono, H. Miyashita, Y. Suzuki, H. Mimura and M. Esashi (2003). "Selective growth of carbon nanotubes on Si microfabricated tips and application for electron field emitters." Journal of Vacuum Science & Technology B **21**(4): 1705-1709.
- Morris, J. R. and X. Y. Song (2002). "The melting lines of model systems calculated from coexistence simulations." Journal of Chemical Physics **116**(21): 9352-9358.
- Muller, E. W. (1955). "Work Function of Tungsten Single Crystal Planes Measured by the Field Emission Microscope." Journal of Applied Physics **26**(6): 732-737.
- Murphy, E. L. and R. H. Good (1956). "Thermionic Emission, Field Emission, and the Transition Region." Physical Review **102**(6): 1464-1473.
- Nasch, P. M. and S. G. Steinemann (1995). "Density and thermal expansion of molten manganese, iron, nickel, copper, aluminum and tin by means of the gamma-ray attenuation technique." Physics and Chemistry of Liquids **29**(1): 43-58.
- Nose, S. (1986). "An Extension of the Canonical Ensemble Molecular-Dynamics Method." Molecular Physics **57**(1): 187-191.
- Nottingham, W. B. (1936). "Thermionic emission from tungsten and thoriated tungsten filaments." Physical Review **49**(1): 78-97.

- Olson, R. T., and J. A. Panitz (1998). "An instrument for investigating high electric field phenomena at small electrode separations." Review of Scientific Instruments **69**(5): 2067-2071.
- Palik, E. D. (1985). Handbook of optical constants of solids. Orlando.
- Park, K. H., S. Lee and K. H. Koh (2006). "Statistical modeling of field-enhancement-factor distribution of nanostructured carbon films." Journal of Vacuum Science & Technology B **24**(2): 898-902.
- Paulini, J., T. Klein and G. Simon (1993). "Thermo-Field Emission and the Nottingham Effect." Journal of Physics D-Applied Physics **26**(8): 1310-1315.
- Pendry, J. B. (1999). "Radiative exchange of heat between nanostructures." Journal of Physics: Condensed Matter **11**(35): 6621-6633.
- Plimpton, S. (1995). "Fast Parallel Algorithms for Short-Range Molecular-Dynamics." Journal of Computational Physics **117**(1): 1-19.
- Pluis, B., A. W. D. Vandergon, J. W. M. Frenken and J. F. Vanderveen (1987). "Crystal-Face Dependence of Surface Melting." Physical Review Letters **59**(23): 2678-2681.
- Pluis, B., A. W. D. Vandergon, J. F. Vanderveen and A. J. Riemersma (1990). "Surface-Induced Melting and Freezing .1. Medium-Energy Ion-Scattering Investigation of the Melting of Pb(Hkl) Crystal Faces." Surface Science **239**(3): 265-281.
- Pratt, L. R. and S. W. Haan (1981a). "Effects of Periodic Boundary-Conditions on Equilibrium Properties of Computer-Simulated Fluids .1. Theory." Journal of Chemical Physics **74**(3): 1864-1872.
- Pratt, L. R. and S. W. Haan (1981b). "Effects of Periodic Boundary-Conditions on Equilibrium Properties of Computer-Simulated Fluids .2. Application to Simple Liquids." Journal of Chemical Physics **74**(3): 1873-1876.
- Pronko, P. P., P. A. VanRompay, R. K. Singh, F. Qian, D. Du, and X. Liu (1996). Laser-induced avalanche ionization and electron-lattice heating of silicon with intense near-IR femtosecond pulses. Materials Research Society Symposium Proceedings (Advanced Laser Processing of Materials--Fundamentals and Applications).
- Purcell, S. T., P. Vincent, C. Journet and V. T. Binh (2002). "Hot Nanotubes: Stable Heating of Individual Multiwall Carbon Nanotubes to 2000 K Induced by the Field-Emission Current." Physical Review Letters **88**(10): 105502.
- Qiu, T. Q. and C. L. Tien (1992). "Short-Pulse Laser-Heating on Metals." International Journal of Heat and Mass Transfer **35**(3): 719-726.

- Qiu, T. Q. and C. L. Tien (1993). "Heat-Transfer Mechanisms During Short-Pulse Laser-Heating of Metals." Journal of Heat Transfer-Transactions of the ASME **115**(4): 835-841.
- Rajurkar, K. P., G. Levy, A. Malshe, M. M. Sundaram, J. McGeough, X. Hu, R. Resnick and A. DeSilva (2006). "Micro and nano machining by electro-physical and chemical processes." CIRP Annals-Manufacturing Technology **55**(2): 643-666.
- Reif, F. (1965). Fundamentals of Statistical and Thermal Physics. New York, McGraw Hill.
- Rethfeld, B, K. Sokolwski-Tinten, D. von der Linde, and S. I. Anisimov (2002a). "Ultrafast thermal melting of laser-excited solids by homogeneous nucleation." Physical Review B **65**(9): 092103
- Rethfeld, B., A. Kaiser, M. Vicanek and G. Simon (2002b). "Ultrafast dynamics of nonequilibrium electrons in metals under femtosecond laser irradiation." Physical Review B **65**(21): 214303.
- Sanchez, J. A., B. T. Wong, M. P. Mengüç and P. Albella (2007). "Field emission and electron deposition profiles as a function of carbon nanotube tip geometries." Journal of Applied Physics **101**(11): 114313.
- Sanchez, J. A. and M. P. Mengüç (2007). "Phase Change Phenomena during Electron-beam Heating: Molecular Dynamics Simulations." Physical Review B **76**(22): 224104.
- Sanchez, J. A. and M. P. Mengüç (2008a). "Geometry dependence on the electro-static and thermal response of a carbon nanotube during field emission." Nanotechnology **19**(7): 075702, pp. 11.
- Sanchez, J. A. and M. P. Mengüç (2008b). "Effect of Multiple Carbon Nanotube Electron Emitters on Electron Deposition Profiles." Journal of Physics D: Applied Physics (in preparation).
- Sanchez, J. A. and M. P. Mengüç (2008c). "Melting and vaporization of Cu and Ni films during electron-beam heating." Journal of Applied Physics **103**(5): 054316.
- Sanchez, J. A., M. P. Mengüç, K.-F. Hii and R. R. Vallance (2008a). "Heat transfer within carbon nanotubes during electron field-emission." Journal of Thermophysics and Heat Transfer-Transactions of the AIAA (in press).
- Sanchez, J. A. B.T. Wong, and M. P. Mengüç (2008b). "Nanomachining of metallic surfaces with an electron-beam: simulations using a 3D hybrid MD-TTM model." Journal of Heat Transfer-Transactions of the ASME (in preparation).

Schafer, C., H. M. Urbassek and L. V. Zhigilei (2002). "Metal ablation by picosecond laser pulses: A hybrid simulation." Physical Review B **66**(11): 115404.

Scouler, W. J. (1967). "Temperature-Modulated Reflectance of Gold from 2 to 10 eV." Physical Review Letters **18**(12): 445.

Shang, X. F., M. Wang, S. Qu, Y. P. Ma, M. Q. Tan, Y. B. Xu, and Z. H. Li (2007). "A model calculation of the tip field distribution for a single carbon nanotube." Journal of Applied Physics **102**(5): 054301.

She, J. C., N. S. Xu, S. Z. Deng, J. Chen, H. Bishop, S. E. Huq, L. Wang, D. Y. Zhong and E. G. Wang (2003). "Vacuum breakdown of carbon-nanotube field emitters on a silicon tip." Applied Physics Letters **83**(13): 2671-2673.

Siwick, B. J., J. R. Dwyer, R. E. Jordan and R. J. D. Miller (2004). "Femtosecond electron diffraction studies of strongly driven structural phase transitions." Chemical Physics **299**(2-3): 285-305.

Spindt, C. A. (1968). "A Thin-Film Field-Emission Cathode." Journal of Applied Physics **39**(7): 3504-3505.

Stillinger, F. H. and T. A. Weber (1985). "Computer-Simulation of Local Order in Condensed Phases of Silicon." Physical Review B **31**(8): 5262-5271.

Sun, L. and J. Y. Murthy (2006). "Domain size effects in molecular dynamics simulation of phonon transport in silicon." Applied Physics Letters **89**(17): 171919.

Swanson, L. W., L. C. Crouser and F. M. Charbonnier (1966). "Energy Exchanges Attending Field Electron Emission." Physical Review **151**(1): 327-340.

Swope, W. C., H. C. Andersen, P. H. Berens and K. R. Wilson (1982). "A Computer-Simulation Method for the Calculation of Equilibrium-Constants for the Formation of Physical Clusters of Molecules - Application to Small Water Clusters." Journal of Chemical Physics **76**(1): 637-649.

Szysko, W. (1995). "Melting and Diffusion under Nanosecond Laser-Pulse." Applied Surface Science **90**(3): 325-331.

Teo, K. B. K., M. Chhowalla, G. A. J. Amaratunga, W. I. Milne, P. Legagneux, G. Pirio, L. Gangloff, D. Pribat, V. Semet, V. T. Binh, W. H. Bruenger, J. Eichholz, H. Hanssen, D. Friedrich, S. B. Lee, D. G. Hasko and H. Ahmed (2003). "Fabrication and electrical characteristics of carbon nanotube-based microcathodes for use in a parallel electron-beam lithography system." Journal of Vacuum Science & Technology B **21**(2): 693-697.

- Touloukian, Y. S., R.K. Kirby, R.E. Taylor, and P.D. Desai (1975). Thermophysical Properties of Matter: Thermal Expansion-Metallic Elements and Alloys. New York, Plenum.
- Tsukada, M. (1983). Work Function. Tokyo, Kyouritsu.
- Vallance, R. R., A. M. Rao and M. P. Mengüç (2003). Processes for Nanomachining using Carbon Nanotubes. US Patent No. 6,660,959 (9 December).
- van der Veen, J. F. (1999). "Melting and freezing at surfaces." Surface Science **435**: 1-11.
- van Pinxteren, H. M. and J. W. M. Frenken (1992). "Incomplete Melting of Pb(001) and Vicinal Surfaces." Surface Science **275**(3): 383-394.
- van Pinxteren, H. M., B. Pluis and J. W. M. Frenken (1994). "Temperature-Dependence of Surface-Melting-Induced Faceting of Surfaces Vicinal to Pb(111)." Physical Review B **49**(19): 13798-13808.
- Vandergon, A. W. D., R. J. Smith, J. M. Gay, D. J. Oconnor and J. F. Vanderveen (1990). "Melting of Al Surfaces." Surface Science **227**(1-2): 143-149.
- Walker, D. G., W. Zhang and T. S. Fisher (2004). "Simulation of field-emitted electron trajectories and transport from carbon nanotubes." Journal of Vacuum Science & Technology B **22**(3): 1101-1107.
- Wang, C. Z., A. Fasolino and E. Tosatti (1988). "Molecular-Dynamics Theory of the Temperature-Dependent Surface Phonons of W(001)." Physical Review B **37**(4): 2116-2122.
- Wang, X. W. and X. F. Xu (2002). "Molecular dynamics simulation of heat transfer and phase change during laser material interaction." Journal of Heat Transfer-Transactions of the ASME **124**(2): 265-274.
- Wang, Z. L., Y. Liu and Z. Zhang (2003). Handbook of Nanophase and Nanostructured Materials, Springer.
- Wang, X. (2005). "Large-scale molecular dynamics simulation of surface nanostructuring with laser-assisted scanning tunneling microscope." Journal of Physics D: Applied Physics **38**: 1805-1823.
- Wang, X. W. and Y. F. Lu (2005). "Solidification and epitaxial regrowth in surface nanostructuring with laser-assisted scanning tunneling microscope." Journal of Applied Physics **98**(11): 114304.
- Wang, M., Z. H. Li, X. F. Shang, X. Q. Wang and Y. B. Xu (2005). "Field-enhancement factor for carbon nanotube array." Journal of Applied Physics **98**(1): 014315.



- Wellershoff, S. S., J. Hohlfeld, J. Gudde and E. Matthias (1999). "The role of electron-phonon coupling in femtosecond laser damage of metals." Applied Physics A: Materials Science & Processing **69**: S99-S107.
- Westover, T., T. S. Fisher and F. Pfefferkorn (2007). "Experimental characterization of anode heating by electron emission from a multi-walled carbon nanotube." International Journal of Heat and Mass Transfer **50**(3-4): 595-604.
- Williams, R. K., and W. Fulkerson (1969). Separation of the electronic and lattice heat contributions to the thermal conductivity of metals and alloys. Thermal Conductivity, From 8th Annual Conference on Thermal Conductivity, Lafayette, IN.
- Wong, B. T. and M. P. Mengüç (2004). "Monte Carlo methods in radiative transfer and electron-beam processing." Journal of Quantitative Spectroscopy & Radiative Transfer **84**(4): 437-450.
- Wong, B. T. and M. P. Mengüç (2008). Thermal Transport for Applications in Nanomachining. Berlin, Springer.
- Wong, B. T., M. P. Mengüç and R. R. Vallance (2004). "Nano-scale machining via electron beam and laser processing." Journal of Heat Transfer-Transactions of the ASME **126**(4): 566-576.
- Wong, B. T., M. P. Mengüç and R. R. Vallance (2006). "Sequential nano-patterning using electron and laser beams: A numerical methodology." Journal of Computational and Theoretical Nanoscience **3**(2): 219-230.
- Xu, X. F., C. R. Cheng and I. H. Chowdhury (2004). "Molecular Dynamics study of phase change mechanisms during femtosecond laser ablation." Journal of Heat Transfer-Transactions of the ASME **126**(5): 727-734.
- Yamashita, Y., T. Yokomine, S. Ebara and A. Shimizu (2006). "Heat transport analysis of femtosecond laser ablation with full Lagrangian modified molecular dynamics." International Journal of Thermophysics **27**(2): 627-646.
- Yang, L. Q., T. S. Rahman and M. S. Daw (1991). "Surface Vibrations of Ag(100) and Cu(100) - a Molecular-Dynamics Study." Physical Review B **44**(24): 13725-13733.
- Yang, X. S. (2005). "Modelling heat transfer of carbon nanotubes." Modelling and Simulation in Materials Science and Engineering **13**(6): 893-902.
- Yi, W., L. Lu, D. L. Zhang, Z. W. Pan and S. S. Xie (1999). "Linear specific heat of carbon nanotubes." Physical Review B **59**(14): R9015-R9018.

Zheng, X., G. H. Chen, Z. B. Li, S. Z. Deng and N. S. Xu (2004). "Quantum-mechanical investigation of field-emission mechanism of a micrometer-long single-walled carbon nanotube." Physical Review Letters **92**(10): 106803.

Zhigilei, L. V. and B. J. Garrison (1999). "Pressure waves in microscopic simulations of laser ablation." Mat. Rec. Soc. Symp. Proc. 538: 491-496.

Zhigilei, L. V. and B. J. Garrison (2000). "Microscopic mechanisms of laser ablation of organic solids in the thermal and stress confinement irradiation regimes." Journal of Applied Physics **88**(3): 1281-1298.

Ziman, J. M. (1960). Electrons and phonons. London, Oxford University Press.

Ziman, J. M. (1964). Principles of the theory of solids. Cambridge, Cambridge University Press.

## VITA

### Personal Data

- Date of Birth: April 8<sup>th</sup>, 1980
- Place of Birth: Guayaquil, Ecuador

### Education

- May 1998 – August 2003: B.Sc. in Mechanical Engineering, Escuela Superior Politécnica del Litoral (ESPOL), Guayaquil, Ecuador, Cum. GPA 4.0/4.0. Magna Cum Laude.

### Scholastic Honors and Awards

- Awarded University of Kentucky Graduate Scholarship to pursue Graduate work (2004-2008)
- Awarded Harper Industries Fellowship to pursue Doctoral Studies in Nanotechnology Research (2004-2005)
- Awarded the University of Alberta Master's Scholarship to pursue graduate studies in 2004 (declined)
- Gold medal to the Best Graduate of the Engineering Majors at ESPOL (2003): Magna Cum Laude distinction
- Silver medal to the Best Graduate of the Mechanical Engineering Department at ESPOL (2003)
- Diplomas for best student: 2001, 2002, 2003; Gold medal in 2001 (highest GPA)
- Awarded full scholarship to pursue mechanical engineering studies at ESPOL (1998 – 2003)
- Selected Best Teaching Assistant of Physics: 2002
- First place on the first Physics Contest at ESPOL (2001)

### Invited Lectures

- Sanchez, J.A., “Electron Field-Emission from Carbon Nanotubes for Nanomachining Applications,” William Maxwell Reed Seminar, March 6<sup>th</sup>, 2008, University of Kentucky, U.S.A.
- Sanchez, J.A., “The Ultimate Milling Machine: Adventures of a Mechanical Engineer in the World of Nanotechnology,” 2006, ESPOL, Guayaquil, Ecuador
- Sanchez, J.A., “How to apply to gradschool,” 2006, ESPOL, Guayaquil, Ecuador
- Sanchez, J.A., “How to apply to gradschool,” 2005, ESPOL, Guayaquil, Ecuador

### Television Interviews

- July 27<sup>th</sup>, 2006, CN3, Guayaquil, Ecuador. Topic: What is Nanotechnology? Details: Interviewed by Fernando Aguayo to talk about the definition of Nanotechnology.
- August 1<sup>st</sup>, 2006, CN3, Guayaquil, Ecuador. Topic: Nanotechnology. Details: Served as translator between host Fernando Aguayo and Prof. M. Pinar Mengüç.
- August 1<sup>st</sup>, 2006, CN3, Guayaquil, Ecuador. Topic: Nanotechnology in developing countries. Details: Interviewed by Antonio Beltran with Prof. M. Pinar Mengüç in the segment “Análisis” to talk about how Nanotechnology could be applied in developing countries like Ecuador.

### Book Chapters

- B.T. Wong and M.P. Mengüç, “Nano-scale thermal transport and its application to nanomachining,” (Springer, Berlin 2008). Sanchez, J.A. Co-Author, Chapter 9: Molecular Dynamics Simulations

### Editorials

- Sanchez, J.A. (2008), “La Nanotecnología y el Futuro de la Medicina,” Oncología, Guayaquil, Ecuador (in press)

## Journal Publications

- Sanchez, J.A., B. T. Wong, and M.P. Mengüç (2008), “Nanomachining of metallic surfaces with an electron-beam: simulations using a 3D hybrid MD-TTM model,” *Journal of Heat Transfer – Transactions of the ASME* (under review)
- Sanchez, J.A. and M.P. Mengüç (2008), “Effect of multiple carbon nanotube emitters on electron deposition profiles,” *Journal of Physics D: Applied Physics* (in preparation)
- Sanchez, J.A., K.-F. Hii, M.P. Mengüç, and R.R. Vallance (2008), “Heat transfer within carbon nanotubes during electron field-emission,” *Journal of Thermophysics and Heat Transfer – Transactions of the AIAA*, (in press)
- Sanchez, J.A. and M.P. Mengüç (2008), “Melting and vaporization of Cu and Ni films during electron-beam heating,” *Journal of Applied Physics*, **103**(5): 054316
- Sanchez, J.A. and M.P. Mengüç (2008), “Geometry dependence of the electrostatic and thermal response of a carbon nanotube during field-emission,” *Nanotechnology* **19**(7): 075702
- Sanchez, J.A. and M.P. Mengüç (2007), “Phase Change Phenomena During Electron-Beam Heating: Molecular Dynamics Simulations,” *Physical Reviews B*, **76**(22): 224104. This paper also appeared in the *Virtual Journal of Nanoscale Science & Technology*.
- Sanchez, J.A., M.P. Mengüç, B.T. Wong and P. Albella (2007), “Field emission and electron deposition profiles as a function of carbon nanotube tip geometries,” *Journal of Applied Physics* **101**(11): 114313. This paper also appeared in the *Virtual Journal of Nanoscale Science & Technology*.

## Conference Publications

- Sanchez, J.A. and M.P. Mengüç, “Molecular Dynamics Study of Phase Change Phenomena during field emission induced nano machining,” *ASME International Mechanical Engineering Congress and Exposition, Chicago, IL 2006*.
- Sanchez, J., Duque, J., “Design and Testing of an experiment of Steady State Natural Convection from the surface of Heated Inclined Cylinders,” 2004,

Proceedings of the ASME Heat Transfer and Fluids Engineering Division Summer Conference 2004 in Charlotte NC.

#### Online animations

- Sanchez, J.A. and M.P. Mengüç (2008), “Nanomachining of metallic surfaces,” [www.ThermalHub.org](http://www.ThermalHub.org) (in preparation)

#### Posters

- Sanchez, J.A. and M.P. Mengüç, “Field emission from carbon nanotubes for nanomachining applications,” Poster at NSF CMMI Engineering Research and Innovation Conference, Knoxville, TN, January 7-10, 2008. Also presented at KYNANOMAT 2008, University of Louisville, March 16-18, 2008.
- Sanchez, J.A. and M.P. Mengüç, “Molecular Dynamics Study of Phase Change Phenomena during field emission induced nano machining,” ASME International Mechanical Engineering Congress and Exposition, Chicago, IL 2006.
- Sanchez, J.A., M.P. Mengüç, K-F Hii, B.T. Wong, R.R. Vallance, “Exploration of Multiphysics phenomena during field emission from a cnt: radiation induced melting,” Poster session ASME International Mechanical Engineering Congress and Exposition, Orlando, FL 2005.

#### Work Experience

- Sep. 2005 -Apr. 2008: Research Assistant: Worked on nanoscale heat transfer.
- Jan.-May 2007: Teaching Assistant of ME 321: Engineering Thermodynamics II.
- Feb.-Jun. 2004: Project Assistant: Repsol YPF, Guayaquil, Ecuador.
- Jan. 2003-Jan. 2005: Research Assistant: ESPOL, Guayaquil, Ecuador.
- May.-Aug. 2003: Project at Repsol YPF: AKRIBIS S.A, Guayaquil, Ecuador.
- Mar.-May 2002: Internship: Holcim, Guayaquil, Ecuador.
- Mar.-May 2000: Internship: La Universal, Guayaquil, Ecuador.
- May 1999-Feb. 2003: Teaching Assistant at ESPOL, Guayaquil, Ecuador